UC-25
LBL-7632
c.1

HIGH-RESOLUTION ELECTRON MICROSCOPY STUDIES OF Au-Ni SPINODAL ALLOYS

Chien-Kuo Wu
(Ph. D. thesis)

November 1978

Prepared for the U. S. Department of Energy
under Contract W-7405-ENG-48

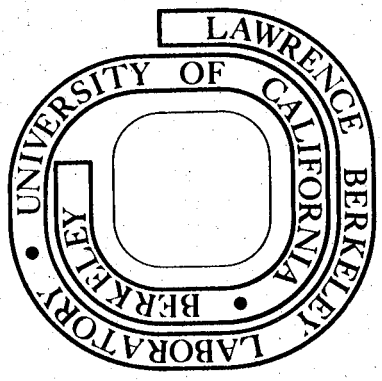

HIGH-RESOLUTION ELECTRON MICROSCOPY STUDIES OF Au-Ni SPINODAL ALLOYS

by

Chien-Kuo Wu
Lawerence Berkeley Laboratory
University of California
Berkeley, California 94720

HIGH-RESOLUTION ELECTRON MICROSCOPY STUDIES OF Au-Ni SPINODAL ALLOYS

Contents

HIGH-RESOLUTION ELECTRON MICROSCOPY STUDIES OF Au-Ni SPINODAL ALLOYS

Chien-Kuo Wu

Materials and Molecular Research Division
Lawrence Berkeley Laboratory
and
Department of Materials Science and Mineral Engineering
University of California
Berkeley, California 94720

ABSTRACT

High-resolution electron microscopy has been utilized to monitor the decomposition process in Au-Ni spinodal alloys. Individual measurements were made of lattice fringe spacings which are sensitive to composition variations at the atomic plane level. Results indicate that rather smooth and regular composition waves are obtained at an early stage of decomposition, and that later stage coarsening results in larger amplitude fluctuations. This provides direct evidence of simultaneous decomposition and coarsening which agrees with theoretical predictions.

An analysis of reaction kinetics and morphology suggests that decomposition is one-dimensional, even after very long aging times. This behavior is believed to be the result of a large matrix strain energy associated with the decomposition product and the slow decomposition kinetics due to low temperature aging (at 150°C).

1. INTRODUCTION

Spinodal decomposition is a mechanism of homogeneous phase transformation which usually produces a uniform, modulated microstructure. From the viewpoint of structural alloy design, there is a great potential for utilizing spinodal reactions to produce tough, strong alloys, since the homogeneous microstructure produced through the decomposition process is quite desirable in engineering applications. It provides uniformly distributed obstacles to minimize local stress concentrations when the material is under deformation. In addition, applications of spinodal transformations to improvement of magnetic properties have already resulted in superior alloys as those based on Fe/Cr/Co. However, the characterization of spinodal systems has so far been very limited, especially from the structure-properties viewpoint.

One difficulty in studying the spinodal reaction in solids is an exact definition of spinodal decomposition that is amenable to experimental verification. The thermodynamic criterion given by Gibbs[1] and then modified by Cahn[2-5] is an exact condition for spinodal decomposition. But it is very difficult to verify experimentally e.g., by diffraction when this thermodynamic criterion is satisfied because data is needed on compositional amplitude and wavelength. However, since the decomposition is spontaneous and fast, and is difficult to suppress by rapid quenching from above the spinodal, it is quite possible that experimental data can only be obtained after the decomposition is completed and diffusion controlled coarsening is obvious.

Hence, it is the purpose of this research to examine, by detailed metallography and diffraction, the behavior of spinodal alloys during

the early stages of decomposition and establish the kinetic relationship between fluctuation amplitude and modulation wavelength. Au-Ni alloys have been chosen particularly for their large difference in component lattice parameters which will permit higher accuracy in determining localized compositional analysis. The high resolution lattice imaging technique of transmission electron microscopy is utilized to directly monitor the process of decomposition, obtaining both wavelength and amplitude components of the composition modulation as a function of aging time by a single measurement. This information will thus serve as a strong complement to recent computer modeling of the decomposition process,[6] and lend further insight into the strengthening mechanisms of spinodal alloys.

2. THEORY OF SPINODAL DECOMPOSITION

The concept of the spinodal was formulated at the same time as nucleation theory.[1] It was first described for chemical solutions by J. Willard Gibbs in the 1880's. The thermodynamic criterion for the spinodal is that the second derivative of the free energy with respect to composition is zero ($\frac{\partial^2 F}{\partial C^2} = 0$). Inside the spinodal, where $\frac{\partial^2 F}{\partial C^2} < 0$, the unstable solid solution decomposes spontaneously into two phases, because there is no activation barrier for such reaction. Therefore, Gibbs referred to the spinodal as the limit of metastability. The new phases form by a continuous diffusional process with a gradual change in composition across the interface. The resulting microstructure consists of a uniform dispersion of small, coherent particles.

It is only very recently that extensions of spinodal phenomena to metallurgical theory and solid solution reactions have been developed fully. A diffusion theory to describe spinodal decomposition was first proppsed by Hillert.[7] Cahn[2] then modified an analytical expression for the phenomenological diffusion equation and described spinodal decomposition as a sinusoidal plane wave fluctuation of the form:

$$C(\underset{\sim}{r}) - C_o = A \cos \underset{\sim}{\beta} \cdot \underset{\sim}{r} \qquad (1)$$

where C_o is the average composition of the homogeneous phase before decomposition, A is the amplitude of the fluctuation, and β is the modulation wave number. By considering the elastic strain and surface energies between the two decomposed phases, the following free energy change per unit volume must be negative in order to satisfy the spinodal condition:

$$\frac{\Delta F}{V} = \frac{1}{4}A2\left[\left(\frac{\partial^2 F}{\partial C^2}\right) + \frac{2\eta^2 E}{1-\nu} + 2K\beta 2\right] \qquad (2)$$

Here, $\partial^2 f/\partial C^2$ is the second derivative of Helmholz free energy with respect to composition, η the linear expansion per unit composition change, E the Young's Modulus for the average composition, ν the Poisson's ratio, and K represents the surface energy due to introducing a gradient of composition. This is the concept of a coherent spinodal that Gibbs did not mention in his original paper. The effect of incipient surface tension and strain energy is to disallow the solution to decompose on too small a scale.

In the initial papers by Cahn[2] on spinodal decomposition, only the linear, or first order, terms in the diffusion equation were considered in order to give an analytical expression that could easily be treated in closed form. The solution to the derived diffusion equation can be mathematically expressed as the superposition of periodic composition waves in the solid solution with an exponential time dependence. Included in the diffusion equation are terms for the coherency strain energy and the concentration gradient energy. The microstructure predicted by Cahn's theory is a periodic distribution of small, coherent particles or regions of the two phases throughout the entire volume of the anisotropic crystal.

Some of the assumptions and mathematical procedures used by Cahn and Hilliard[8,9] to derive the diffusion equation for an inhomogeneous solid solution were questioned in articles by Hirth, Tiller and Pound[10] and Tiller, Pound and Hirth[11]. However, in a subsequent paper by Morris,[12] the validity of the diffusion equation derived by Cahn

and Hilliard was substantiated. Also, Cahn and Hilliard[13] have written a rebuttal to the criticisms raised by Hirth, et al.

Cahn[5] has considered the effects of those nonlinear terms on the phase separation in the later stages of spinodal decomposition and the beginnings of particle coarsening by using a series approximation to represent the composition dependence of the diffusion coefficient and by then solving the resulting non-linear equation by successive approximations. From this analysis, it was shown that harmonic distortions are produced that interact with the initial symmetrical composition waves in such a way as to approach the equilibrium structure. In alloys of asymmetrical compositions, the even harmonics distort the initial composition waves to give a minor phase far from the average composition and a major matrix phase consistent with the lever rule. The odd harmonics convert the fundamental sine wave into a square wave, i.e. a composition profile more characteristic of a two phase structure, by flattening the peaks of the fundamental and sharpening the gradient between the extremes in composition.

As for the beginnings of particle coarsening, Cahn's analysis[5] predicts a gradual broadening of the fundamental spectrum with longer aging time. When the non-linear terms become significant in altering the composition waves to satisfy the lever rule, the phase that will eventually become the minor phase is more developed in the regions of greater amplification. These minor phase particles remain larger and the lever rule requirement that there be less of the minor phase is carried out predominantly at the expense of the minor phase in

the less developed regions. Thus large wavelengths which are multiples, or harmonics, of the initial wavelength develop.

In a paper describing computer simulation of one-dimensional spinodal decomposition, Swanger, Gupta, and Cooper[14] have made the one-dimensional non-linear differential equation for spinodal decomposition dimensionless, converted it to a difference equation, and evaluated it numerically using periodic boundary conditions. The results obtained confirm that the initial stages of the growth of small fluctuations can be described by a linearized version of Cahn's diffusion equation. The non-linear term is necessary for the fluctuation to cross the spinodal and approach the phase boundary. The existence of a gradient energy at the diffuse interfaces between the two phases acts as a driving force favoring the longest possible fluctuation as an equilibrium solution to the diffusion equation.

However, in a recent computer modeling of the whole decomposition process, Morris[6] took all the non-linear terms of the spinodal diffusion equation into account and found that the kinetic relationship between the modulation wavelength and aging time is substantially low as compared to that of the diffusion-controlled, multi-dimensional coarsening reaction. Hence it is believed that at the beginning of spinodal decomposition, interpenetrating multi-dimensional composition waves will not be observed. Instead the microstructure should consist of many micro-domains such that only a one-dimensional modulation is developed within each domain. There are examples in the literature[15] which suggest that the local decomposition process occurs in this way. However, a detailed study of this morphology has not yet been

undertaken, nor has the concept of a one-dimensional model been highly publicized. Thus the aim of this research is to extend our fundamental understanding of spinodal decomposition in light of these microstructural models and provide the necessary detail for documenting the onset of both phase separation and particle coarsening.

3. EXPERIMENTAL REVIEW

3.1 Conventional Methods

Spinodal decomposition is characterized by small composition fluctuations over large distances, while a classical nucleation process is characterized by large composition variations over small distances. Because the new phases form by a continuous diffusional process with a gradual change in composition across the interface, they must have similar crystal structures as the original solid solution and they must be coherent. The resulting microstructure consists of a uniform dispersion of small, coherent particles. Experimental observations have shown that spinodal decomposition occurs in metallic, ceramic and glass systems. Several review articles[16-18] have described the theoretical and experimental studies pertaining to spinodal decomposition.

In elastically anisotropic materials, spinodal decomposition occurs along the elastically "soft" directions which are the cube directions for most cubic alloys.[19] The resulting periodic structure produces sidebands in diffraction patterns, and this effect has been studied extensively by investigators using x-ray diffraction. The first observation of such sidebands was reported by Bradley[20] for a Cu-Ni-Fe alloy that had been quenched and then aged inside the miscibility gap. Daniel and Lipson[21,22] made further observations on the same alloy and, using a model based on a periodic, modulated structure, they derived a formula relating the sideband spacing to the structural periodicity which has been confirmed by transmission electron microscopy.[23,24] The physical origin of these sidebands in some

Cu-Ni-Fe alloys was considered in further detail in a subsequent article by Hargreaves.[25]

The microstructures of a spinodally decomposed alloy can be characterized by these parameters:

(1) Volume fraction of the two phases;

(2) Wavelength of the modulations;

(3) Amplitude of the composition fluctuations.

Analyses of these parameters with respect to mechanical properties in spinodal Cu-Ni-Fe alloys have been performed by Butler and Thomas[23] and Livak and Thomas.[24] Their experimental results revealed that, while coherency is maintained, the increment of yield stress is directly proportional to the difference in cube lattice parameters of the two decomposing phases, and is independent of the wavelength and volume fractions in symmetric and asymmetric alloys. This is in good agreement with Dahlgren's model[26] based on internal coherency stresses to explain the yield stress of alloys containing modulated structures. The observations made on the yield strength of Au-Pt alloys[27] and Cu-Ni-Cr alloy[28] support the conclusion that in spinodal alloys containing a large volume fraction of coherent particles, the internal stresses are the primary strengthening mechanism. However, from the available data one cannot exclude other factors such as differences in shear moduli, Burgers vectors or stacking fault energies between the two phases or a chemical interaction at the interface that may contribute to the strengthening.

In Cahn's[29] analysis, the yield stress of spinodal alloys should be proportional to the product of the amplitude (A) squared and the

wavelength (λ) of the composition modulation, ($A^2\lambda$). However, Ditchek and Schwartz[30] found that this prediction was not consistently observed in Cu-Ti and Cu-Ni-Fe alloys, and so proposed a new mechanism of hardening. In their model, the shear stress due to misfit strains caused by the passage of a dislocation on its slip plane is calculated. The yield stress increment (ΔYS) was thus found to be proportional to (A/λ)S, where S is a "squaring factor", and when S was substituted by ($\lambda - \lambda_0$), where λ_0 is the fundamental wavelength of decomposition, a plot of ΔYS versus (A/λ)($\lambda - \lambda_0$) showed a linear relationship. Hence these researchers concluded that S is proportional to ($\lambda - \lambda_0$). For short aging times, the yield stress increment rises rapidly due to the rapid rise in ($\lambda - \lambda_0$)/λ. In the later stages, ($\lambda - \lambda_0$)/λ nears unity and then ΔYS is proportional to A, which is exactly Dahlgren's argument.

The most sensitve technique for following the change in amplitude of the composition waves in alloys containing iron seems to be Mossbauer spectroscopy, and the decomposition of Cu-Ni-Fe alloys[31,32] and Fe-Cu alloys[33,34] has been studied using this technique. Small angle x-ray scattering has also proved to be very useful in experimentally verifying Cahn's model for spinodal decomposition.[35] Furthermore, small angle scattering can be used to observe the change in the concentration gradient at the interface using a form of Porod's equation for the scattering intensity.[36] Less sensitive techniques for following the change in amplitude of the composition waves are measurements of electrical or magnetic properties that depend on the compositions of the decomposing regions. Transmission electron microscopy has been very useful in characterizing the microstructure of spinodal

alloys,[23,24] but is still not used as widely as can be. The most direct method of studying the spinodal structure is to use field ion microscopy where possible (e.g. Au-Pt alloys can be studied using FIM).[37]

Spinodal decomposition during continuous cooling is of technological interest since continuous cooling will afford a convenient method of developing spinodal structures in commercial heat treating practice. Huston, Cahn and Hilliard[38] have extended Cahn's theory to the case of continuous cooling by treating certain of the coefficients in the linearized diffusion equation as time dependent because of their strong temperature dependence. Badia, Kirby and Mihalisin[39] have studied the strengthening during continuous cooling of Cu-Ni-Cr alloys containing 20 to 45% Ni with up to 4% Cr. Because of the small amount of Cr in the alloys studied, it is uncertain if any of the alloy compositions were inside the spinodal region for this ternary system. However, their experimental observations showed many points of similarity with the theoretical calculations of Huston et al. for spinodal decomposition during continuous cooling.

Several alloy systems have been studied that show evidence of spinodal decomposition. Many decomposed alloys exhibit the sideband phenomenon, but such an observation is not sufficient evidence to conclude that the alloy has decomposed spinodally. Although a periodic microstructure is characteristic of a spinodal alloy that is elastically anisotropic, such microstructures can also be developed by selective growth due to elastic alignment as observed in Cu-Co[40] and Ni-Al[41,42] alloys.

Cahn[16] has outlined the procedure to follow in developing a spinodal alloy. One would begin with a system in which one has observed coherent precipitates of the same or related crystal structures or has reason to suspect that they might occur. When such precipitates do occur, one knows that it is possible in this system to cross the coherent phase boundary and thus have enough driving force to overcome elastic stresses. The spinodal is then usually attainable through a small change in composition or a greater undercooling. By suitable additional alloying elements, the coherency strain can be altered to affect the accessibility of the spinodal.

Some other alloy systems for which there is evidence to suggest decomposition by a spinodal mechanism are Au-Pt,[27,43,44] Al-Zn[35] and Au-Ni.[45,46] Morral and Cahn[47] demonstrated the possibility of both spinodal decomposition and continuous ordering occurring in some ternary alloys under certain conditions, e.g. in some Cu-Mn-Al alloys[48] both phase separation and ordering occur simultaneously and in Cu-Ti[49] and Ni-Ti[50] alloys ordering reaction is apparently preceded by spinodal decomposition. In recent study on the early stages of G.P. zone formation in naturally aged Al-4% Cu alloys,[51] diffuse satellite spots were found in electron diffraction patterns prior to the formation of the platelike G.P. zones. Thus these observations provide evidence for the occurrence of spinodal decomposition at room temperature and the continuous formation of G.P. zones is then interpreted in terms of Cahn's later stage spinodal theory.[5]

3.2 Lattice Imaging

Studies of spinodal decomposition by x-ray diffraction[18] reveal only the wavelength of the early stage modulation and the average modulation amplitude through diffracted intensities, which are averaged over a large specimen volume. Convential bright-field or dark-field images by transmission electron microscopy (TEM) cannot provide any compositional information about the two phases.[23,24,52] It is only possible to detect the localized, plane-by-plane variations in composition directly by corresponding lattice parameter modulations through the lattice imaging technique.[53,54]

Lattice imaging is a high-resolution technique in TEM by which more than one beam is allowed to pass through the objective aperture. The interference among these beams will, under appropriate circumstances, then give sets of fringes corresponding to the lattice planes in the crystal which produce the diffraction spots. This is a very useful method for obtaining information down to the atomic level in alloys (for a general review, see Allpress and Sanders[55]).

Many of the early studies utilizing lattice imaging for quantitative analysis were concerned with crystal lattice dislocations (see Ref. 56-59). However, from studies of the properties of calculated images, it was later demonstrated[60] that a change in the diffraction geometry could produce changes in the number of terminating fringes and in the fringe bending which were not related to the lattice plane geometry in any simple way. Only when the dislocation line was oriented end-on with respect to the electron beam was a single fringe termination produced.[16] Thus, it serves as an example that extreme care must

be taken in the interpretation of lattice fringe profiles with matrix structure.

In other defect studies, lattice imaging was successful in revealing microtwins of 3 atom plane thickness, intrinsic and extrinsic faults, loop defects and dislocations in epitaxial silicon.[62] In ion-bombarded Ge[63] and Cu,[64] damaged regions exhibited either no fringe contrast or severe strain contrast in the lattice image mode, respectively, suggesting a lack of crystallinity and a complex strain field in the specimens.

As for the investigation of alloys undergone certain phase transformations, lattice imaging is superior in providing detailed structure as well as compositional information in the samples. The continuous phase changes from G.P. zones to θ-precipitates in Al-Cu alloys were the first that received extensive attention.[63,65,66] In research on ordering reactions, lattice imaging has shown considerable advantages over other conventional methods,[69-73] particularly in the areas of short-range order and the detailed structure of ordered lattice defects. Similar applications to a Cu-Be alloy[67] and omega transformation in Zr-Nb alloys[68] all showed the fine structural data in localized regions.

A recent investigation of the relationship between grain boundary structure and boundary-nucleated phase transformations by lattice imaging showed three reactions associated with grain boundaries in the Al-Zn system.[74] A direct verification of plane matching model at a grain boundary interphase interface has also been obtained through this study.[75]

The utilization of lattice imaging to obtain local lattice parameter measurements and hence estimates of composition by applying Vegard's law was pioneered here at Berkeley.[54,76,77,81,90]

Other applications of this method to phase transformations in solids, including the characterizations of microstructure in magnetic Fe-Cr-Co alloys,[76] the atomic environments near twin, lath and α/martensite boundaries in steels,[77] and the crystalline and grain boundary structures in ceramics,[78] have provided finer details that only high-resolution lattice imaging technique can provide.

The most recent reports on the high resolution techniques of transmission electron microscopy indicate that not only single sets of lattice planes can be imaged, but also many-beam atomic structural images can be obtained,which is a great advance in terms of resolution.[91] Individual atoms are resolved and atomic positions in molecules of several minerals and ceramics are identified. These demonstrate the ability and potential in future research by lattice imaging. In addition, with the help of optical microdiffraction, estimates of composition for suitable solutes can be obtained through the correspondence with localized "d" spacings[81,90] (10 - 20Å areas).

During spinodal decomposition, there is no structural change, only highly localized fluctuations in composition. Using direct lattice fringe images, these can be established from the relationship between interplanar spacing and composition. Gronsky et al.[53] first used lattice imaging for studying spinodal alloys. In preliminary results of spinodally decomposed An-77 at.% Ni alloy,[54,79,80] lattice parameter differences (Δa) were clearly detected from one region to another

by measurements on microdensitometer traces across the lattice fringes. In addition, the average wavelength determined from this technique was in exact agreement with that determined from the positions of satellite reflections in the corresponding diffraction patterns. Thus, the lattice image of this material reveals the principal features expected of a spinodally decomposed alloy, and laser optical diffraction from the lattice image negatives also showed characteristic satellite reflections. This latter method allows areas as small as 10Å (1 nm) in diameter to be chosen to give diffraction data which are far superior in terms of resolution to those from selected area electron diffraction. These optical diffraction patterns can also be used to obtain fringe spacing changes,[80] and are an alternative to the microdensitometer measurements for obtaining fringe spacing information particularly for low visibility images.

The continued studies of spinodal decomposition in a commercial Cu-Ni-Cr alloy by lattice imaging[81] have revealed not only the early stage composition fluctuations, but also the later stage coarsening reactions. Individual fringe spacings can be obtained and plotted against distance to show the overall composition profiles in the system, and three types of interphase interface were found in the same specimen as a result of particle coarsening. The correlations of microstructural changes and mechanical properties are thus discussed.[28]

The significance of the work in the Cu-Ni-Cr alloy stems from the fact that although the maximum difference in lattice parameters between the two decomposed phases is less than 1%, characteristic composition profiles can be shown throughout the aging sequence.

In fact the study was intended to determine whether or not this type of fundamental research in spinodal decomposition made possible by lattice imaging can be carried out on more complex alloys. It is also due to the small difference in lattice parameter that intermediate decomposition stage can hardly be detected in this alloy. Hence, in order to directly monitor the process of decomposition, the Au-Ni system is chosen in this research to extend our fundamental understanding of the transformation mechanism.

3.3 Decomposition in Au-Ni System

The Au-Ni alloy system is one of many binary systems in which the supersaturated solid solutions may exhibit a multi-staged precipitation behavior during aging. The existence of a miscibility gap in the phase diagram (Fig. 1) with a critical point was first recognized by microscopic observations of annealed and quenched alloys containing 10-80 wt% Ni.[82] The form of the miscibility gap was further determined by Mossbauer spectroscopy in a more recent study.[83]

The early investigations by Koster and Dannohl showed a relatively simple decomposition behavior in this system.[84] The solid solution characteristic of high temperature could readily be retained upon quenching to room temperature. As these solid solutions were aged at intermediate temperatures (between 400°C and 600°C), they decomposed by a discontinuous reaction into a mixture of a Au-rich and a Ni-rich solid solution.

The X-ray low angle scattering studies of Au-Ni alloys found that the high-temperature solid solutions had pronounced short-range ordering[85] in order to reduce lattice strain energy. The short-

range-order persists even during aging at an intermediate temperature (315°C) as long as any untransformed part of the solid solution exists. Sivertsen and Wert[86] then observed that there was at least one metastable precipitate formed on low temperature annealing. It occurred about 10^4 times earlier than the discontinuous phase change studied previously.[84] The critical temperature above which this low temperature phase is unstable is about 225°C. They indicated that the phase seemed to be clusters of Au-rich or Ni-rich atoms.

The electron diffraction study on precipitation phenomena in thin films of supersaturated Au-Ni alloy[87] showed satellite reflections along cube directions which is the characteristic of modulated structures in the specimen. The satellite reflections disappeared on aging just above the critical temperature.[46] On reaging at a lower temperature, the satellites did not reappear. This was taken to indicate that the presence of a large concentration of quenched-in excess vacancies is required for the development of the modulated structure.

The subsequent investigations of Au-Ni alloys by Fisher and Embury[88] showed that the wavelength of finely spaced gold and nickel-rich layers was about 30-50 Å. It was thus suggested that the modulated structure was developed through spinodal decomposition which is in good agreement with theoretical calculations by Cahn.[2] However, the critical temperature of about 225°C is much higher than originally predicted.

Cahn[2] has considered that the spinodal should be defined only for cases where the composition fluctuations remain coherent with the matrix. Taking into account the resultant elastic energy and

surface tension effects, it was predicted that the boundary of such a coherent spinodal would be depressed well below the chemical spinodal (approximately 2000°C in the Au-Ni system). A more recent attempt to locate the boundary of the coherent spinodal was made by Golding and Moss.[89] This calculation was similar to the one performed by Cahn, but experimental values of the elastic constants and the entropy as a function of composition were used. The variation of the elastic constants with composition caused a non-uniform depression of the coherent spinodal relative to the chemical spinodal with a shift in the critical composition and temperature of the coherent spinodal to 40 at.% Ni and 0°C, in comparison with the peak of the chemical spinodal at 71 at.% Ni and 812°C. Solid solutions within the coherent spinodal would be unstable with respect to infinitesimal composition fluctuations on {100} planes, since the elastic energy is a minimum in ⟨100⟩ directions. Certain preferred wavelengths of these composition fluctuations would continue to develop, leading to the formation of a sinusoidally modulated structure in a state of metastable equilibrium.

In the case of Au-Ni alloys, where there are both a large difference in atomic size and an appreciable difference in scattering factor, a periodic composition modulation should lead to the formation of satellite reflections about all of the fundamental reflections, including the origin. In addition, an asymmetry in the satellite intensity is predicted by the Hargreaves model,[25] with the low angle satellite more intense than the high angle satellite. This is exactly what has been observed in a Au-77 at.% Ni spinodal alloy.[54]

In this investigation, Au-Ni alloys were aged at 150°C to produce the spinodal microstructure. The reason for choosing this particular temperature is that it gives maximum decomposition kinetics.[46] Measurements were then made at different aging periods to establish the relationships between the composition fluctuations and the modulation wavelengths in the early decomposition stages.

4. EXPERIMENTAL PROCEDURES

4.1. The Samples

The alloys were kindly provided by Cominco Electronic Materials in thin strips (24" x 1" x 5 mils). The three alloy compositions studied were:

Alloy 1. Au - 95 wt% (85 at.%)
Ni - 5 wt% (15 at.%)

Alloy 2. Au - 75 wt% (47 at.%)
Ni - 25 wt.% (53 at.%)

Alloy 3. Au - 50 wt% (23 at.%)
Ni - 50 wt% (77 at.%)

4.2. Heat Treatment

The samples were cut into small pieces (2" x 1" x 5 mils) and sealed in evacuated quartz-tubes for homogenization. After solution treated at 850° for 72 hours, the specimens were quenched into ice-brine. Subsequent heat-treatments were performed at 150°C from 1 hour to 4000 hours.

4.3 TEM Specimen Preparation

Thin foils for transmission electron microscopy were prepared by jet-polishing with the following solution and conditions:

Solution: 34 gm Potassium Cyanide;
7.5 gm Potassium Ferrocyanide;
7.5 gm Potassium Sodium Tartrate;
10 cm^3 Phosphoric Acid;
2 cm^3 Ammonia;
500 cm^3 Water.

Conditions: Temperature - room temperature ($\sim 25^{o}C$)

Voltage - 40V (D.C.)

Specimens were then ready for electron microscopy observations.

4.4 Lattice Imaging

For the lattice imaging technique, a Philips EM 301 transmission electron microscope equipped with high resolution stage was utilized. Specimen grains with [001] or [011] parallel to the microscope optical axis were found and the crystal was then tilted such that a two-beam condition with a strongly diffracted (200) spot was obtained in order to image (200) lattice fringes. These reveal the characteristics of spinodal decomposition along this direction.

4.5 Calibration of the Magnification

Usually lattice imaging pictures were taken in the electron microscope operating at high magnification (over 5×10^5 times). The calibration of the exact magnification of the microscope is very important for any quantitative measurement on the lattice fringe spacings. Since the true magnification is only within 10% limits of that normally shown on the microscope meter, the exact magnification was determined by the following rocedures.

Firstly, the average lattice constant of the alloy at each aging condition was determined by standard x-ray diffraction methods. The average corresponding (200) lattice fringe spacings was established on enlarged micrographs and the magnification found for this particular picture.

4.6 Measurement of Lattice Constants

Three different methods were used to measure the variations of lattice parameters between the two phases from lattice imaging negatives:

(i) Optical diffraction: The lattice imaging negatives were placed in the path of a He-Ne laser beam in a standard optical bench. The fringes present in the negatives give rise to diffraction spots in the back focal plane of the optical objective lens. Then by measuring the distance r between the transmitted and difrracted spots, using the formula:

$$L = rd$$

where L is a constant, and by comparison with that of standard gold (200) fringes, then d, the corresponding lattice spacing giving rise to the diffracted spots, can be determined.

(ii) Microdensitometer trace analysis: The individual lattice constants can be found by directly measuring the distance from peak to peak on a microdensitometer plot of the image and dividing by the appropriate magnification.

Here in this research, average values were obtained over 10 fringe spacings at a time, and standard deviations were calculated to give the accuracy limits. The final shape of the curve will then show the variations of the lattice parameters.

(iii) Direct measurement from enlarged micrograph: It is straightforward just to measure the lattice spacings on an enlarged micrograph, divide by the magnification and the lattice constants can be obtained immediately.

4.7 Accuracy of Measurements

The three different methods used to measure the fringe spacings have been described above. The accuracy of each method will be estimated as follows:

(i) Optical diffraction provides the most reliable results among the three methods. It converts fringe image information of lattice planes in the specimen into diffraction spots. By placing a certain size of aperture in the beam path, diffraction information can be obtained even from a very small area in the material.

The only limitation of this technique is governed by the aperture size, since the aperture will itself diffract. Fig. 2 shows optical diffraction patterns from the same area in the negative using three different aperture sizes. In (a), the aperture size is comparable to ~35 Å in the real crystal. The aperture itself gives diffraction patterns as Fraunhofer rings, which will sometimes interfere wih the diffraction spots and broaden them. The intensity is low due to the small size of aperture. It is also more uncertain to lcoate the exact center of the diffraction spots as they are broadened. Hence the errors in measurement are increased.

By sacrificing the resolution, a large aperture size gives sharper diffraction spots (Fig. 2 b,c) which results in more accurate measurements. Generally, using a rule marked down to 0.5 mm, the estimated accuracy is ~0.5%. This is quite reproducible, the errors originating from uncertainty in measuring the distance between the diffraction spots.

(ii) Microdensitometer trace analysis will provide more accurate data as long as there are easily recognizable fringes in the negative.

Fig. 3 shows (200) lattice fringes of a pure gold specimen and their corresponding microdensitometer traces. Since the fringes are clear in the micrograph, the microdensitometer trace is also very sharp and the fringe positions can be easily identified as those peaks in the plot.

The exact position of each peak sometimes becomes unidentifiable due to lack of contrast in the negative near the fringe. For example, in the present spinodal alloy, dark and bright diffraction contrast occurs due to the decomposition and this masks the exact position of the fringes. This effect is illustrated in Fig. 4 which shows (200) lattice fringes of a Cu-Ni-Cr alloy aged at 600°C for 1 hour and their corresponding microdensitometer traces. The fringe positions become smeared and broadened. This limits the accuracy of measurements.

Hence, in order to minimize these kinds of experimental errors, it is advisable to take an average value over 10 or 20 fringe spacings and thus smooth the curves. The accuracy limit is then estimated to be ~1%.

(iii) Since the lattice fringes broaden at high magnification, it is difficult to locate the exact positions of fringes on the prints. Thus an error always exists for direct measurements from enlarged micrographs. Usually, the accuracy can be improved if measurements averaged over a number of fringe spacings are made (see Fig. 5). Yet, a reasonable estimation of ~2% error is possible in this method by measuring 10 fringe spacings at a time.

5. RESULTS

5.1. Au-15 at.% Ni Alloy

(i) As quenched material: Figure 6 shows the electron diffraction pattern and electron image of the as-quenched Au-15% at.% Ni specimen. The foil orientation is [001]. There is no sign of any decomposition or transformation in the matrix, persumably due to a rapid quenching rate. The diffuse rings in the diffraction pattern probably originate from surface contamination which can also be seen in the image (Fig. 6(b)).

(ii) Aged samples: When the specimens are aged at 150°C, diffuse streaks along ⟨100⟩ cube directions are first observed in the electron diffraction pattern (Fig. 7). Clusters of solute atoms of only 1-2 lattice layers thick, on {100} planes are formed in the matrix. These appear to have dark contrast in a bright-field electron image (Fig. 8), similar to G. P. Zone formation in Al-Cu alloys.[92,93] The small size of the zones gives rise to the long reciprocal lattice streaks in diffraction patterns due to shape factor.[94]

The lattice imaging micrograph of this specimen really shows the detailed lattice structures of the zones (Fig. 9). In this alloy, Ni is the solute atom of smaller atomic size. As clustering occurs the cumulative elastic strain energy at the Au-Ni interfaces results in a change of (200) fringe spacing. Also, since the component species are still coherent, the lattice fringes remain continuous from one region to the other.

There are two sets of zones in contrast in Fig. 9. Those marked "P" are perpendicular to the electron beam (i.e., lie in the foil),

and those marked "E" are parallel to the electron beam (the so-called "edge-on" zones). The thickness of the zones is about 2 ~ 4Å with diameter 20 ~ 40Å. The zones are nucleated homogeneously throughout the entire specimen area.

One interesting feature that was revealed by lattice imaging is that the alloy seems to have evidence of short-range order in very localized regions. This is indicated in Fig. 10. The arrowed areas have super-lattice structures in which the fringe spacings are double that of the fundamental spacings. These can only be observed over very short distances (here less than 10Å). The reason for this phenomenon may be explained as follows. Since the Au-Ni alloys exhibited short-range-order for the homogeneous high-temperature solid solution,[85] the structure can be preserved as the specimens were quenched from high temperature. Thus evidence of short-range-order is found as long as any untransformed part of the solid solution exists. Apparently, it does not disappear homogeneously during subsequent aging.

After longer aging time, the zones coarsened. Figure 11 is a bright-field micrograph of the sample aged 20 hr at 150°C. The strain contrast is larger than that in Fig. 8. It seems that the small zones tend to join together and become larger ones. This effect can also be illustrated in the lattice imaging mode.

Figure 12 shows the (200) lattice fringes of the same specimen in Fig. 11. The dimensions of most zones are about 10-20Å thick and greater than 100Å in diameter. Also, it is interesting to note that some zones are bigger as a result of combining several small ones while some zones are close to each other which may be in the

process of joining together. Hence, these observations suggest a typical nucleation and growth type transformation. Since the purpose of this research is to investigate the early stages of spinodal decomposition, this alloy is not suitable for the present study. However, from the above illustrations, the advantages of utilizing the high-resolution lattice imaging technique in the studies of phase transformations in alloys are clearly revealed, e.g., one can ascertain whether a particular alloy is inside or outside the coherent spinodal or not.

5.2. Au-53 at.% Ni Alloy

(i) As-quenched specimens: Spinodal decomposition is a spontaneous phase transformation which begins as the limit of metastability is reached. It results in a modulated microstructure and produces satellite reflections around Bragg diffracted peaks. This is exactly what has been observed in the as-quenched Au 53 at.% Ni alloy (e.g., see Fig. 13).

Notably it appears that the composition modulation is one-dimensional, as indicated in the electron diffraction pattern shown in Fig. 14. Here, the crystal orientation is [011] and satellite reflections along [0$\bar{1}$1] can be seen surrounding every Bragg diffraction spot. From a standard (011) stereographic-projection (Fig. 15), it is seen that the [0$\bar{1}\bar{1}$] direction lies in the same zone as two of the cube directions ([010] and [001]). It is also noticed that there are no satellite reflections along the [100] direction in Fig. 14. Hence, based upon diffraction evidence alone, there appears to be no modulation in structure along at least one cube direction for this particular specimen area.

A close examination of the image furthermore reveals that in fact the modulation affects only a single set of cube planes.

An experiment was performed whereby the specimen was oriented to an exact [001] zone, and the image contrast along various diffraction contours was examined in detail (Fig. 16). It is interesting to note that wavy modulations can be seen within the (200) band (Fig. 16(c)) which are not as clear in the (020) band (Fig. 16(b)). The specimen was then tilted such that the (200) and (020) reflections are operating in the same specimen area (Figs. 17(a) and (b), respectively). Periodic modulation perpendicular to $\vec{g}$ = [200] in Fig. 17(a) indicates that a composition wave is developed along [100] in this area and, as $\vec{g}$ = [020] is operating, no such kind of modulation can be seen in Fig. 17(b). These observations suggest that spinodal decomposition will not produce interpenetrating modulations along all three cube directions but, possibly, only one-dimensional composition fluctuations will exist in the localized specimen region.

Lattice imaging of the as-quenched specimens provides even more detailed microstructural information about the sample. Figure 18(a) is a bright-field image of the as-quenched Au-53 at.% Ni alloy in which pronounced modulations are observed, indicating that the alloy has already decomposed. Note also that the corresponding electron diffraction pattern (Fig. 18(b)) is similar to that in Fig. 14. Figure 19(a) shows the (11$\bar{1}$) fringes of the circled area in Fig. 18(a). The modulation contrast makes an angle of ~145° to the (11$\bar{1}$) fringes, which is precisely the angle between [11$\bar{1}$] and [0$\bar{1}$1]. The optical diffraction pattern (Fig. 19(b)) of this micrograph

also shows satellite reflections along the [0$\bar{1}$1] direction, normal to the large scale modulation.

When the (200) planes of the specimen are imaged, three different kinds of contrast are observed: (1) fine (200) fringes on a periodic background structure (Fig. 20); (2) the same (200) fringes on a non-periodic background (Fig. 21); and (3) highly localized regions of (100) fringe periodicity (arrowed areas in Fig. 22), again on a non-periodic background. This latter phenomenon is somewhat unexpected and deserves further investigation.

Thus, these observations indicate that spinodal decomposition has already started in the as-quenched specimens. These modulations show typical periodic contrast in the images (Figs. 16 and 20) along one of the cube directions. The non-periodic background in Figs. 21 and 22 may result from imaging the non-decomposed cube lattice planes. This also serves as an evidence for the one-dimensional modulation model in the early stage of spinodal decomposition.

(ii) Aged specimens: Figure 23(a) is an electron micrograph of an alloy aged one hour at 150^{o}C. The crystal orientation is [001] and satellite spots can be seen along [100] in the corresponding electron diffraction pattern (Fig. 23(b)). Note that these arise from the strong one-dimensional modulations observed within the image (Fig. 23(a)).

The higher modulation contrast in Fig. 23(a) (c.f., Fig. 13) is obviously due to an increase in composition amplitude, which induces a large elastic strain energy within the matrix.

Figure 24 is a (200) lattice image of the same sample aged 1 hr at 150°C. The large scale dark and bright contrast is because of the composition fluctuations which are typical of a modulated microstructure imaged under two-beam conditions. The fringe spacings vary from one region to the other, but the wavelength is well-defined (see Sections 5.2 (iii) and (iv)). It may be a combined result of decomposition and coarsening.

In order to provide direct evidence of one-dimensional modulation in the material, two different sets of {200} lattice planes have been imaged within the same specimen area. Figure 25(a) shows the (200) lattice fringes for sample aged 1 hr at 150°C. There seems to be a certain periodicity of modulation along [100] and the optical diffraction pattern of this image shows satellite reflection around the main spots. When the specimen is tilted to image the (020) lattice fringes (Fig. 25(b)), it shows no periodic modulations along [010] direction and no satellite reflections are seen in the optical diffraction pattern. Therefore, this indicates that spinodal decomposition takes place in this particular specimen area only along [100] direction.

For still longer aging times, this one-dimensional modulation remains with no sign of multi-dimensionality. The electron diffraction patterns all show uni-directional satellite reflections like those in Fig. 14 and Fig. 23(b). The coarsening rate is very slow and the modulation wavelength increases at a comparatively low value. Figure 26 is a bright-field electron image of a Au-53 at.% Ni alloy aged 4000 hr at 150°C. Note that the measured wavelength is only about 55Å. The large elastic strain energies between the two phases in this system

and the slow decomposition kinetics of low temperature aging (at 150°C) may be the reasons for the slow coarsening rate.

(iii) Measurements of modulation wavelength. The modulation wavelength can be obtained either by direct measurements from enlarged micrographs or from satellite spacings in the electron diffraction pattern using the Daniel-Lipson equation:[21,22]

$$\lambda = \frac{h \tan\theta}{(h^2 + k^2 + l^2)\, d\theta}\, a_o$$

Here, θ = Bragg angle for the (hkl) reflection in a crystal of lattice parameter a_o, $d\theta$ = angular spacing between a satellite spot and its main reflection.

In this research, measurements were made throughout the entire aging sequence and values obtained by the above two methods were found to be in close agreement. For example, the measured wavelength on the enlarged micrograph in Fig. 23 is 29 ± 4Å and the calculated wavelength from the diffraction pattern is 31 ± 2Å.

Figure 27 is the log-log plot of wavelength vs aging time at 150°C. The slope of this curve is quite low when compared with previous studies on spinodal systems (e.g., Cu-Ni-Fe,[23,24] Cu-Ni-Cr[28]), all of which show that the relationship $\lambda \propto t^{1/3}$, which corresponds with the diffusion controlled three-dimensional coarsening reaction, is universally observed. However, the estimated value of the slope in Fig. 27 is only about 1/10. The implications of this finding are discussed in more detail in Section 6.4.

(iv) Detection of composition amplitude: As stated previously, spinodal decomposition is characterized by small composition fluctuation

over a large distance. The process is continuous and the resulting microstructure consists of solute-rich and solute-poor regions. Thus, the most interesting aspect of the decomposition process is the composition amplitude and modulation wavelength variation as a function of aging time.

Since the lattice constant depends on composition, then by directly imaging the lattice planes in the crystal, the localized lattice parameter of the specimen can be obtained. Hence, the lattice imaging method is useful for estimating composition profiles in the alloy. Modulation wavelength in the material can also be detected at resolutions down to the atomic-plane level by plotting fringe spacing variations vs distance.

Figure 28 is a (200) lattice imaging micrograph for an alloy aged 1 hr at 150°C. The fringes are continuous from dark regions to bright regions, indicating that the two phases are coherent and the interface is diffuse as expected at the early stage of decomposition. The electron and optical diffraction patterns (Fig. 29(a),(b)) all show satellite reflection along [100] direction, indicating that a modulated structure is developed in the specimen. Measurements of fringe spacings by microdensitometer give the composition profile as shown in Fig. 30. The ragged shape of the profile may be due to the error in defining the exact peak positions in the direct microdensitometer traces as described before. This kind of inaccuracy can be reduced if averaged over a number of fringe spacings. Figure 31 is an example by averaging, over 10 fringe spacings at a time, the data in Fig. 30. The error bars represent the standard deviations

arising from the averaging procedure. Here, a rather smooth fluctuation and regular modulation wavelength is obtained. The estimated lattice parameters of the two phases are ~3.9Å and ~3.7Å which correspond to Au-rich and Ni-rich regions, respectively. The modulation wavelength is about 29Å which is in good agreement with that found in direct measurements from enlarged micrograph or calculated from satellite spacings (see Section 5.2 (ii)).

The overall composition profiles are similar when comparing Fig. 31 with Fig. 30. The averaging procedures smooth the curve and cut off the high-peak values in Fig. 30. However, by doing so, some resolution is sacrificed, especially since there is a large strain field in this alloy. Those high peak (or low peak) values may be truly representative of the specimen due to strain effect on fringe spacings.[95] But the only interesting information at this stage is the nature of any composition gradients in the specimen. Figure 31 is thus capable of preserving the major compositional features in the specimen.

As mentioned in Section 4.7 (i), the laser optical diffraction technique serves as a more reliable method in the determination of fringe spacings on lattice imaging micrographs. The information recorded on lattice images can be selectivity monitored through a small field-limiting aperture. In this way, an objective assessment can be made of the variation in fringe image position. An additional advantage of the method is its sensitivity to low visibility fringe images as in the case of the above spinodal product. Figure 32 is a series of optical diffraction patterns taken of Fig. 28 at ~20Å advancing steps with an aperture ~30Å in size. The positions of the diffraction

spots vary as the fringe spacings vary on the lattice imaging negative. The maximum difference of fringe spacings measured from the patterns is ~6.5% which is also close to that estimated on microdensitometer trace analysis (Fig. 31). Therefore, these results really show the capability of high-resolution lattice imaging technique in the detection of localized composition amplitude at an atomic plane level.

For longer aging times, the decomposition will proceed, resulting in larger composition amplitude and longer modulation wavelength. Figure 33 is a (200) lattice imaging micrograph for alloys aged 100 hr at 150°C. The strain contrast here is larger than that in Fig. 28. This suggests that the associated strain field due to composition amplitude in this micrograph is larger than that in Fig. 28 and the interface is sharper as well.

Figure 34 is the measured (200) fringe spacings by direct microdensitometer analysis. The ragged shape of the curve is similar to that in Fig. 30, only the maximum difference in fringe spacings is much larger. Again, by averaging over 10 fringe spacings of Fig. 34, the composition profile is smoothed as shown in Fig. 35. It seems that the modulation wavelength is not so regular as that in Fig. 31, which may be interpreted as a result of coarsening. Some of the particles are in the process of "joining together" and the wavelength is thus longer.

The high values and low values of fringe spacings in Fig. 35 have exceeded the possible limiting pure Au (4.07Å) and pure Ni (3.52Å) lattice parameters. Since the fringe spacings will be dominated by the large strain field accompanying the decomposition, the measurements

in Fig. 35 may show the extra expansion and contraction of the fringe spacings at the interface. These may explain the origin of the high and low peak values. The estimated lattice parameters of the two phases are ~4.0Å (Au-rich phase) and ~3.55Å (Ni-rich phase) at this later stage which correspond to 12% difference. These values are approaching the limiting tie-line compositions of the two phases (see the Au-Ni phase diagram in Fig. 1).

The optical diffraction patterns also show this effect. Figure 36 depicts the result for an aperture equivalent to ~40Å diameter at the specimen plane. By moving the aperture in 20Å increments, an obvious variation in diffraction spot spacing is produced. The measured maximum difference of lattice parameters between the two phases from Fig. 36 is also ~12%.

Thus, from this kind of information, not only the modulation wavelength is recorded, but the amplitude of composition modulation is captured as well. The early stage behavior of spinodal decomposition can be obtained through the comparison of Fig. 31 with Fig. 35. The composition amplitude as well as modulation wavelength is found to increase. This is what should be expected from the transformation kinetics of spinodal decomposition.

5.3. Au-77 at.% Ni Alloy

Previous studies on the Au-77 at.% Ni alloy[54] showed that the specimen produced modulated structures which result from spinodal decomposition. The high resolution analysis obtained by the correspondence of fringe spacing variations with composition fluctuations indicate that a large difference (~12%) in lattice parameters between the two

phases exist in the material. However, a more systematic study of this alloy is carried out in this research and many similarities of decomposition behavior between the Au-77 at.% Ni alloy and the Au-53 at.% Ni alloy are found which will be described as follows.

Firstly, the decomposition process is also along one of the cube directions and only one-dimensional composition waves are developed in localized specimen areas. This is supported by uni-directional satellite reflections in the diffraction pattern (as in Fig. 14) and the tilting experiment (as in Fig. 17).

Secondly, the coarsening rate is slow and the plot of modulation wavelength vs aging time shows the same relationship as in Fig. 27. This is due to one-dimensional coarsening reaction as a result of one-dimensional decomposition.

Thirdly, the composition amplitudes between the two phases detected by lattice imaging exhibit similar magnitude to that of the Au-53 at.% Ni alloy. The maximum difference in fringe spacings is ~12% as well. This is in good agreement with the tie-line compositions of the two phases and with the previous study as mentioned above.[54]

6. DISCUSSION

6.1. Decomposition in Au-15 at.% Ni Alloy

Previous studies on the Au-Ni system concentrated either on the determination of chemical components (e.g., diffusion coefficients, thermodynamic activities, entropies, etc) at high temperatures, or in the decomposition behavior of high nickel content alloys (greater than 20 at.%). Very little information has been obtained about the transformation process of low-nickel content alloys.

In this research, it is found that zones about 1~2 atomic layers thick are formed in a Au-15 at.% Ni alloy when aged at 150°C (see Fig. 9), which is typical of diffusion-controlled nucleation and growth phase transformations as in the case of Al alloys containing a few per cent Cu.[96-99] This behavior results from the fact that the present alloy is too dilute in nickel to lie within the coherent spinodal, although it does lie inside the chemical spinodal of the phase diagram (see Fig. 1).

The difference between a classical nucleation reaction and spinodal decomposition is that there is no activation barrier for the new phase to form in spinodal decomposition, while there is such a barrier for nucleation. Hence, spinodal decomposition is spontaneous and is characterized by small composition fluctuations over large distances where the nucleation process is characterized by large composition variations over small distances. An example demonstrating this difference in decomposition mechanism is obvious from a comparison of Fig. 6 and Fig. 13. The as-quenched Au-15 at.% Ni alloy (Fig. 6) shows no sign of decomposition in the matrix (prior to nucleation), but the as-quenched

Au-53 at.% Ni alloy (Fig. 13) has already decomposed into two phases (by a spinodal mechanism).

Another interesting feature revealed by the high-resolution lattice images is that a (100) superlattice fringe periodicity is found in very localized regions (see Fig. 10). This phenomenon has never been reported before and certainly deserves further investigation. It is also particularly important that this type of analysis be carried out very carefully, since there are more than two beams included to form the image (i.e., the transmitted beam, the fundamental spot and a superlattice spot) and the fringe profile is thus focus dependent.[69-73] However, the advantage of high resolution lattice imaging technique in the detection of localized structural information on this atomic plane scale is clearly demonstrated.

6.2. The One-Dimensional Modulation Model of Spinodal Decomposition

The as-quenched and aged specimens of Au-53 at.% Ni and Au-77 at.% Ni alloys all show evidence of spinodal decomposition (see 5.2 and 5.3). Modulated structures that consist of fine, wavy particles of the second phase are observed in the samples.

The most important result found in this research is that the modulation is not multi-dimensional along all three cube directions in localized regions. It seems that only one-dimensional modulation waves are developed in small domains which then make up the whole crystal grain (see Figs. 14, 16 and 17). Thus, a one-dimensional modulation model is proposed to describe the early stages of spinodal decomposition in this system and is shown in Fig. 37. Here, the polycrystalline material is divided into several representative grains. Within each grain, composition waves along one of the cube directions are

produced in regions of smaller subdivision, and these composition waves do not interpenetrate.

After proposing this model, it is proper to ask whether this one-dimensional modulation should be observed in all the spinodal systems, and a survey of the literature on this point has been conducted.

Firstly, in a previously studied Cu-Ni-Cr spinodal alloy,[28] it has been found that a possible one-dimensional composition wave is seen at the early stage of decomposition. Figure 38 shows the alloy aged 10 min at 700°C. In (a), the (020) contour band is brought into contrast and a periodic modulation is observed in the image. When the same specimen area is tilted such that $\vec{g}$ = [200] is operating, there is no such kind of modulation in (b). This is similar to the tilting experiment of the Au-53 at.% Ni alloy shown in Fig. 17, indicating that a composition wave is developed only along [100] in this particular specimen region.

It is also found in asymmetrical Cu-Ni-Fe spinodal alloys[100] that the modulation wavelength increases slowly at the early stage of decomposition. A summary of the changes that occur in yield stress, Curie temperature and wavelength for such an alloy aged at 625°C is shown in Fig. 39. Note that prior to 10 hr aging time, the shape of the log-log plot of wavelength vs aging time is similar to that obtained in the Au-53 at.% Ni alloy (see Fig. 27) which is a result of a one-dimensional coarsening reaction. Thus, it is possible that the Cu-Ni-Fe alloys have undergone a one-dimensional decomposition as well.

In their studies of decomposition in Cu-Ti alloys, Laughlin and Cahn[101] have used evidence obtained from a sequence of electron micrographs to prove that the system decomposes spinodally. However, at short aging times (less than 10 min), the modulation wavelength remains almost constant which may again be due to one-dimensional composition waves in the specimen giving rise to a slow coarsening rate.

Hence, it is believed that this one-dimensional modulation period should be observed for most spinodal systems. The reason that this phenomenon has been neglected in the past is either due to the resolution limit of the experimental techniques (e.g., x-ray methods, where bulk specimens are studied in volumes large enough to include many one-dimensional composition waves along all the three cube directions), or due to the rapid decomposition rate which prevents this reaction from being observed. In the latter case, the one-dimensional decomposition reaction quickly evolves into a multi-dimensional coarsening reaction. This point will be further discussed in Section 6.4.

6.3. Comments on Composition Analysis

One of the most important objectives of studying spinodal decomposition is to obtain the shape and amplitude of the composition profile in the specimen aged at various times. Using lattice fringe images, these can be established from the relationship between inter-planar spacing and composition. It is clear from the above results that both composition amplitude and modulation wavelength can be obtained by a single measurement of fringe spacings which is then plotted as a function of distances (see Section 5.2).

In the previously studied Cu-Ni-Cr spinodal alloy,[81] the correlation between fringe spacing and the known lattice constants of particular phases at the later stage of decomposition has been demonstrated. It is due to the small lattice parameter difference ($\Delta a \sim 1\%$) that resolution has to be sacrificed by averaging over a number of fringe spacings in order to attain the necessary precision. The effect of such a procedure is to "smooth" the profile, whether it be ragged or whether it be sharply discontinuous. Unfortunately, it can be easily shown that a "square-wave" modulation would become continuously varying in amplitude after such an "averaging procedure."[81]

In the present case, although the lattice parameter difference is comparatively large ($\Delta a \sim 14\%$), this "averaging procedure" is still necessary in estimating composition amplitude. It is because of the slow decomposition kinetics at low aging temperature (150°C) that fine-scale modulation wavelength is developed in the alloys ($\lambda \sim 30$-50 Å), which makes it difficult to distinguish one phase from the other, and the large coherency strains associated with the large lattice parameter difference in the system could further complicate the interpretation of fringe profiles at interfaces. The rough shape of direct microdensitometer measurements in Figs. 30 and 34 results from this effect. Those high peak and low peak values may originate from the large coherency strains or from inaccurate measurements of exact fringe positions as discussed in Section 4.7. Thus, it is advisable to take average values over a number of fringe spacings to minimize the possible errors. In doing so, the overall profile is preserved (Figs. 31 and

35) while the extremes are smoothed and a more regular composition wave is produced.

In comparing Figs. 31 and 35, it would be tempting to take the data in Fig. 31 to indicate an approximately sinusoidal waveform at the early stages of decomposition, schematically represented in Fig. 40(a). This stage of development is also characterized by a smaller composition amplitude ($\Delta a \sim 6.5\%$ for this particular case) with continuous variations in composition across a diffuse interface. By contrast, Fig. 35 would represent an approximately square wave, characteristic of later stages of the reaction, as in Fig. 40(b). At later stages of development the composition amplitude increases ($\Delta a \sim 12\%$) along with the modulation wavelength, and the interface appears to sharpen. Hence, these results provide the desirable composition information expected from spinodal decomposition at atomic-plane level which no other technique can of itself provide.

In summary, the results indicate that in a given region decomposition occurs along a particular ⟨100⟩ direction only, but in adjacent regions modulations occur in non-parallel ⟨100⟩ as sketched in Fig. 37. In this way the alloy is divided up into "domains." It may be that this morphology developes to minimise the macroscopic strains

$$(\Delta\varepsilon_x + \Delta\varepsilon_y + \Delta\varepsilon_z = 0) \quad .$$

6.4. The Decomposition Sequence

Spinodal decomposition is a spontaneous phase transformation[1] which involves no activation barrier for formation of a new phase. Small separations in composition all lower the free energy, and therefore

proceed spontaneously until the equilibrium tie-line compositions are reached.

For most spinodal alloys, this spontaneous trend away from homogenization is very rapid and, usually within minutes, the whole process is completed. Previous X-ray[18] and electron[23,24] diffraction studies document only the later stage post-decomposition behavior when a diffusion controlled coarsening reaction is obvious. As a result of this study, however, it is clear that the entire decomposition process can be fully described.

From the model proposed in Section 6.2, it is believed that independent composition waves along only one of the cube directions are developed within small domains (Fig. 37) in the specimen as spinodal conditions are satisfied (see Eqs. (1) and (2)). This one-dimensional distribution of homogeneous second phase particles is also energetically favorable when the elastic energy associated with the difference in specific volumes of the precipitating phases is considered.[102] Consequently, the microstructure consists of fine, wavy solute-rich regions, which lie along only one cube direction (see Figs. 17 and 38).

In the original paper on spinodal decomposition,[1] only chemical conditions were considered. Cahn[2] was the first one to introduce the concept of a "coherent spinodal" by taking the surface tension and elastic energy between the two phases into account. The effect of surface tension is to prevent decomposition of the solution on too fine a scale, while elastic energy stabilizes the solution and alters the criterion for the limit of metastability. By considering the rate of growth of the composition fluctuations resulting from

the infinitesimal variations, account must be taken of higher order terms, particularly in the free energy expansion, so that these fluctuations will cease growing when equilibrium is reached. The recent theoretical calculations of Morris[6] indicate that one-dimensional composition waves are favorable at an early stage of decomposition. This result agrees well with the present experimental observations and the proposed one-dimensional model in Fig. 37.

The one-dimensional composition waves are then found to coarsen according to the law $\lambda \propto t^{1/10}$ in order to reduce surface energies between the two phases (see Fig. 27). This relationship between wavelength and aging time is also found in Morris' calculation[6] and is a result of the one-dimensional coarsening reaction. It is because of this slow coarsening rate that this phenomenon has been overlooked in many systems (see Section 6.2).

As aging continues, coarsening among adjacent one-dimensionally modulated domains will take place[6] when the following two conditions are satisfied: (1) the decomposition kinetics are large; (ii) the elastic strain energy between the two phases is relatively low. Although the resultant interpenetrating, multi-dimensional waves are elastically unfavorable,[102] the volume energy contributions are large enough that elastic energy contributions are negligible. Thus, the second phase will then appear as cuboids as shown in Fig. 41(b) which is typical of a multi-dimensional particle morphology. From this point on, the coarsening rate speeds up according to the law $\lambda \propto t^{1/3}$, characteristic of a three-dimensional diffusion controlled coarsening reaction[23,24] (e.g., see Fig. 39. The slope of log-log plot of

wavelength vs aging time increases after 10 hr aging time and follows the law $\lambda \propto t^{1/3}$.)

However, this transition from one-dimension to multi-dimensional modulations seems to be wavelength dependent and a critical value of $\lambda_c \sim 100\text{-}200\text{Å}$ is suggested by literature reviews of several spinodal systems (e.g., Cu-Ni-Fe, Cu-Ni-Cr, Cu-Ti). When the wavelength remains below λ_c, the modulation is believed to be one-dimensional (Fig. 41(a)), and for a value above λ_c, it is multi-dimensional (Fig. 41(b)). Of course, this value is only a rough estimate and further detailed analyses, both in experiments and theoretical calculations, are necessary in the future.

With further aging, the particles become larger until they reach the point where they lose coherency.[103] Therefore, the entire decomposition sequence can be schematically illustrated in the following way:

homogeneous solid solution → one-dimensional composition modulations in small domains → multi-dimensional modulated structures → loss of coherency → incoherent, stable second phase in the matrix.

As for the present Au-Ni alloys, only one-dimensional composition modulations are observed in the specimen. It is due to the slow decomposition kinetics (aging at 150°C) and large elastic strain energy in the system that both factors prohibit the alloys from formation of multi-dimensional particles.

7. SUMMARY AND CONCLUSIONS

A series of Au-Ni alloys have been studied to understand the entire spinodal decomposition sequence. From this research, the following conclusions have been drawn.

(1) The low nickel content alloy (Au-15 at.% Ni) shows zone segregation in the matrix aged at 150°C. This results from the fact that the present alloy is too dilute in nickel to lie within the coherent spinodal.

(2) The as-quenched and aged specimens of the medium (Au-53 at.% Ni) and high (Au-77 at.% Ni) nickel content alloys all show evidence of spinodal decomposition when aged at 150°C. Satellite reflections in the diffraction pattern and modulated structures are observed in the samples typical of spinodal decomposition.

(3) The most significant result of this research is the detection of small microstructural domains in which composition modulations develop along a single crystallographic direction. This is supported by uni-directional satellite reflections in the diffraction pattern and images which result from tilting experiments wherein periodic modulations are observed along only one cube direction.

(4) A one-dimensional modulation "domain" model is proposed to describe the early stages of spinodal decomposition when composition waves do not interpenetrate. A survey of the literature also shows that most spinodal systems have probably undergone a similar one-dimensional decomposition reaction (e.g., Cu-Ni-Cr, Cu-Ni-Fe, Cu-Ti).

(5) The relationship between modulation wavelength and aging time for Au-53 at.% Ni and Au-77 at.% Ni alloys obeys the law

$\lambda \propto t^{1/10}$. This is explained by the dimensionality of the composition profile, since this is a much slower coarsening rate than that observed for multi-dimensional Ostwald ripening.

(6) The high-resolution lattice imaging technique has been utilized to estimate the composition amplitude as well as modulation wavelength in the specimen. It is found that a smooth and regular waveform with diffuse interfaces is produced for the Au-53 at.% Ni alloy aged 1 hour at 150°C when the measured fringe spacing is plotted against distances. The estimated composition amplitude in terms of lattice parameter difference (Δa) is about 6.5%, which corresponds to an intermediate decomposition stage. When the same alloy is aged 100 hours at 150°C, an approximate square wave characteristic of later decomposition stage is observed, with lattice parameter difference up to 12%. This value in fact corresponds to the equilibrium tie-line compositions of the two phases. Thus, it provides the desired information expected from spinodal decomposition at an atomic-plane level.

(7) The whole spinodal decomposition process can be described as follows:

homogeneous solid solution → one-dimensional modulations in small domains → multi-dimensional second phase particles in the matrix → loss of coherency of the particles → incoherent, stable equilibrium phase.

(8) The slow decomposition kinetics due to low-temperature aging and the large strain field in this system prevent the present spinodal alloys from forming a multi-dimensional array of particles in the matrix.

ACKNOWLEDGEMENTS

The author wishes to express his gratitude to Professor Gareth Thomas for his continuous encouragement and support while conducting this research. Deep appreciation is extended to Dr. Ronald Gronsky for his asistance in experiment and critical review of the manuscript. Helpful discussions with Professors J. W. Morris and A. G. Khachaturyan are also gratefully acknowledged.

Reseach facilities and technical staff were provided by the U. S. Department of Energy through the Materials and Molecular Research division of the Lawrence Berkeley Laboratory. Financial support was obtained by a grant from the National Science Foundation.

Love from the author's family members, such as his parents (Mr. and Mrs. Fong-Shiang Wu) and his brother (Dr. Wei-Kuo Wu) are highly appreciated. He is especially indebted to his wife Sophia and his son Howard for their love and tenderness throughout the years in Berkeley.

REFERENCES

1. The Scientific Papers of J. Willard Gibbs, p. 105, Dover (1961).
2. J. W. Cahn, Acta Met. 9, 795 (1961).
3. J. W. Cahn, Acta Met. 10, 907 (1961).
4. J. W. Cahn, J. Chem. Phys. 42, 93 (1965).
5. J. W. Cahn, Acta Met. 14, 1685 (1966).
6. J. W. Morris, Jr., Department of Materials Science and Mineral Engineering, University of California, Berkeley, private communication, February 1978.
7. M. Hillert, Acta Met. 9, 525 (1961).
8. J. W. Cahn and J. E. Hilliard, J. Chem. Phys. 28, 258 (1958).
9. J. W. Cahn and J. E. Hilliard, J. Chem. Phys. 31, 688 (1959).
10. J. P. Hirth, W. A. Tiller and G. M. Pound, Phil. Mag. v. 22, 117 (1970).
11. W. A. Tiller, G. M. Pound and J. P. Hirth, Acta Met. 18, 225 (1970).
12. J. W. Morris, Jr., Phil. Mag. 23, 1041 (1971).
13. J. W. Cahn and J. E. Hilliard, Acta Met. 19, 151 (1971).
14. L. A. Swanger, P. K. Gupta, and A. R. Copper, Jr., Acta Met. 18, 9 (1970).
15. See for example, Figs. 3 and 4 of Ref. 100. Also, This model has been discussed in recent technical meetings. See Program of AIME Fall Meeting, 1978.
16. J. W. Cahn, Trans. AIME 242, 166 (1968).
17. J. E. Hilliard, Phase Transformation (American Society for Metals, 1970), p. 497.

18. D. deFontain, Ultrafine-Train Metals (Syracuse University Press, 1970), p. 93.

19. J. W. Cahn, Acta Met. 10, 179 (1962).

20. A. J. Bradley, Proc. Phys. Soc. 52, 80 (1940).

21. V. Daniel and H. Lipson, Proc. Roy. Soc. London 181A, 368 (1943).

22. V. Daniel and H. Lipson, Proc. Roy. Soc. London 182A, 378 (1944).

23. E. P. Butler and G. Thomas, Acta Met. 18, 347 (1970).

24. R. J. Livak and G. Thomas, Acta Met. 19, 497 (1971).

25. M. E. Hargreaves, Acta Cryst. 4, 301 (1951).

26. S. D. Dahlgren, Met. Trans. A 8A, 347 (1977).

27. R. W. Carpenter, Acta Met. 15, 1297, 1567 (1967).

28. C. K. Wu and G. Thomas, Met. Trans. A 8A, 1911 (1977).

29. J. W. Cahn, Acta Met. 11, 1275 (1963).

30. B. Ditchek and L. H. Schwartz, Proc. of the 4th Intern. Conf. on the Strength of Metals and Alloys, Vol. 3, p. 1319 (1976).

31. A. Nagarajan and P. A. Flinn, Applied Phys. Letters 11, 120 (1967).

32. L. H. Bennett and L. J. Swartzendruber, Acta Met. 18, 485 (1970).

33. D. Chandra and L. H. Schwartz, Met. Trans. 2, 511 (1971).

34. T. DeNys and P. M. Gielen, Met. Trans. 2, 1423 (1971).

35. K. B. Rundman and J. E. Hilliard, Acta Met. 15, 1025 (1967).

36. M. Murakami, O. Kawano, Y. Murakami and M. Morinaga, Acta Met. 17, 1517 (1969).

37. W. Polanschutz and E. Krautz, Surface Science 46, 602 (1974).

38. E. L. Huston, J. W. Cahn and J. E. Hilliard, Acta Met. 14, 1053 (1966).

39. F. A. Badia, G. N. Kirby and J. R. Mihalisin, Trans. ASM 60, 395 (1967).

40. V. A. Phillips, Trans. AIME 230, 967 (1964).

41. A. J. Ardell, R. B. Nicholson and J. D. Eshelby, Acta Met. 14, 1295 (1966).

42. V. A. Phillips, Acta Met. 14, 1533 (1966).

43. T. J. Tiedema, J. Bouman and w. G. Burgers, Acta Met. 5, 310 (1957).

44. L. J. van der Toorn, Acta Met. 8, 715 (1960).

45. R. Gibala, Trans. AIME 230, 255 (1964).

46. J. E. Woodilla, Jr. and B. L. Averbach, Acta Met. 16, 255 (1968).

47. J. E. Morral and J. W. Cahn, Acta Met. 19, 1037 (1971).

48. M. Bouchard and G. Thomas, 29th Ann. Proc. of Electron Microscopy Society of America, G. W. Bailey, ed. (Claitor's Publishing Division, Baton Rough, La., 1971), p. 126.

49. A. Datta and W. A. Soffa, Acta Met. 24, 987 (1976).

50. D. E. Laughlin, Acta Met. 11, 53 (1976).

51. R.J. Rioja and D. E. Laughlin, Met. Trans. A 8A, 1257 (1977).

52. M. Bouchard and G. Thomas, Acta Met. 23, 1485 (1975).

53. R. Gronsky, M.Okada, R. Sinclair and G. Thomas, 33rd Ann. Proc. of Electron Microscopy Society of America, G. W. Bailey, ed. (Claitor's Publishing Division, Baton Rough, LA, 1975), p. 22.

54. R. Sinclair, R. Gronsky and G. Thomas, Acta Met. 24, p. 789 (1976).

55. J. G. Allpress and J. V. Sanders, J. Applied Cryst. 6, 165 (1973).

56. T. Komoda, J. Appl. Phys. Japan 5, 452 (1966).

57. J. R. Parsons and C. W. Hoelke, J. Appl. Phys. 40, 866 (1969).

58. V. a. Phillips and J. A. Hugo, Acta Met. 18, 123 (1970).

59. J. R. Parsons and C. W. Hoelke, Phil. Mag. 22, 1071 (1970).

60. D. J.H. Cockayne, J. R. Parsons and C. W. Hoelke, Phil. Mag. 24, 139 (1971).

61. V. A. Phillips and R. Wagner, J. Appl. Phys. 44, 4252 (1973).

62. V. A. Phillips, Acta Met. 20, 1143 (1972).

63. J. R. Parsons, M. Rainville and C. W. Hoelke, Phil. Mag. 21, 1105 1970).

64. L. M. Howe and M. Rainville, Rad. Eff. 16, 203 (1972).

65. V. A. Phillips, Acta Met. 21, 219 (1973).

66. V. A. Phillips, Acta Met. 23, 751 (1975).

67. V. A. Phillips and L. E. Tanner, Acta Met. 21, 441 (1973).

68. A. L. J. Chang, S. L. Sass and W. Krakow, Acta Met. 24, 29 (1976).

69. K. Schneider, R. Sinclair and G. Thomas, Proc. of the Eighth Intern. Congress on Electron Microscopy, Vol. 1, Canberra, 1974, p. 520.

70. R. Sinclair, K. Schneider and G. Thomas, Acta Met. 23, 873 (1975).

71. R. Sinclair and G. Thomas, J. Applied Cryst. 8, 208 (1975).

72. J. Dutkiewicz and G. Thomas, Met. Trans. 6A, 1919 (1975).

73. R. Sinclair and J. Dutkiewicz, Acta Met. 25, 235 (1977).

74. R. Gronsky, Ph. D. Thesis, University of California, Berkeley, LBL-5784 (1976).

75. R. Gronsky and G. Thomas, Scripta Met. 11, 791 (1977).

76. M. Okada, Ph. D. Thesis, University of California, Berkeley, LBL-7668 (1978).

77. J. Y. Koo and G. Thomas, 35th Ann. Proc. Electron Microscopy Society of America, G. W. Bailey, ed.(Claitor's Publishing Division, Baton Rough, La, 1977), p. 118.

78. D. R. Clarke and G. Thomas, 35th Ann. Proc. Electron Microscopy Society of America, G. W. Bailey, ed. (Claitor's Publishing Division, Baton Rouge, La., 1977), p. 114.

79. R. Gronsky, R. Sinclair and G. Thomas, 34th Ann. Proc. Electron Microscopy Society of America, G. W. Bailey, ed. (Claitor's Publishing Division, Baton Rouge, La, 1976), p. 494.

80. G. Thomas, R. Sinclair and R. Gronsky, Proc. of the Sixth European Congress on Electron Microscopy, p. 114 (1976).

81. C. K. Wu, R. Sinclair and G. Thomas, Met. Trans. A 9A, 381 (1978).

82. W. Fraenkel and A. Stern, Z. anorg, Chem. 166, 161 (1927).

83. E. M. Howard, C. E. Violet and R. J. Borg. Trans. of the Metallurgical Society of AIME 242, 1503 (1968).

84. W. Koster and W. Dannohl, Z. Metallk. 38, 248 (1936).

85. P. Flinn, B. L. Averbach and M. Cohen, Acta Met. 1, 673 (1951).

86. J. Sivertsen and C. Wert, Acta Met. 7, 275 (1959).

87. Y. Fukano, J. of the Physical Society of Japan 16, 2295 (1961).

88. R. M. Fisher and J. D. Embury, Proc. of the 3rd European Regional Conference on Electron Microscopy, Czechoslovak Academy of Sciences, Prague, Czechoslovakia, 1964, p. 149.

89. B. Golding and S. C. Moss, Acta Met. 15, 1239 (1967).

90. R. Sinclair and G. Thomas, Met. Trans. A 9A, 373 (1978).

91. See Proc. of the Ninth Intern. Congress on Electron Microscopy, Toronto, Canada, 1978, J. M. Sturgess, ed. Vol. I, pp. 242, 244, 250, 256, 258, 260, 262, 264, 268.

92. A. Guinier, Ann. Phys. 12, 161 (1939).

93. A. Guinier, Solid State Phys. 9, 293 (1959).

94. P. B. Hirsch, A. Howie, R. B. Nicholson, D. W. Parhley and M. J. Whelan, Electron Microscopy of Thin Crystals (London, Butterworths, 1965), p. 98.

95. P. Rez, Proc. of the Ninth Intern. Congress on Electron Microscopy, Toronto, Canada, J. M. Sturgess, ed., 1978, Vol. I, p. 280.

96. J. M. Silcock, T. J. Heal and H. K. Hardy, J. Inst. Met. 82, 239 (1954).

97. R. B. Nicholson and J. Nutting, Phil. Mag. 3, 531 (1958).

98. R. B. Nicholson, G. Thomas and J. Nutting, J. Inst. Met. 87, 429 (1958-59).

99. A. Kelly and R. B. Nicholson, Prog. Mat. Sci. 10(3), 193 (1963).

100. R. J. Livak, M. S. Thesis, Univ. of California, Berkeley, UCRL-19189 (1970).

101. D. E. Langhlin and J. W. Cahn, Acta Met. 23, 329 (1975).

102. A. G. Khachaturyan, Phys. Stat. Sol. 35, 119 (1969).

103. R. J. Livak and G. Thomas, Acta Met. 22, 589 (1974).

FIGURE CAPTIONS

Fig. 1. The Au-Ni phase diagram. T_c is the chemical spinodal, while T' and T are experimental and theoretical estimate of the coherent spinidal, respectively.

Fig. 2. Optical diffraction patterns taken from the same area with different equivalent aperture sizes: (a) ~30Å, (b) ~50Å (c) ~120Å.

Fig. 3. Lattice image and microdensitometer traces of Au (200) fringes, showing clear distinct peaks.

Fig. 4. Lattice image and microdensitometer traces of Cu-Ni-Cr (200) fringes after aging at 600°C for 1 hr. The peaks have much lower visibility than those in Fig. 3.

Fig. 5. A lattice image of gold (200) fringes. The average lattice spacing is determined more precisely if a larger number of fringes are used in the measurement.

Fig. 6. The as-quenched Au-15 at.% Ni alloy, showing no sign of decomposition in the matrix. (a) (001) electron diffraction pattern. (b) The corresponding bright-field image. The diffuse rings in diffraction pattern originate from surface contamination of the specimen.

Fig. 7. (001) electron diffraction pattern for Au-15 at.% Ni alloy aged 1 hr at 150°C. Diffuse streaks along cube directions suggest that zones about a few atomic layers thick are formed in the sample.

Fig. 8. Bright-field image of the same alloy as in Fig. 7. Note that small zones are visible in the matrix.

Fig. 9. (200) lattice fringes of the same alloy as in Fig. 7. Zones about 1-2 atomic layers thick are clearly resolved. There are two types of zones in contrast: those marked "E" are parallel with the electron beam, the so-called "edge-on" zones; those marked "P" are in the foil. The lattices are continuous and coherent.

Fig. 10. A short-range (100) periodicity is observed in localized arrowed area. This may be due to the preservation of short-range order at high temperatures.

Fig. 11. Bright-field image of the Au-15 at.% Ni alloy aged 20 hr at 150°C. The zones coarsen and strain energies are larger between the two phases.

Fig. 12. (200) lattice fringes of the same alloy as in Fig. 11. The zones are about 10-20 Å thick, indicating the effect of coarsening. Note that the lattices are still coherent.

Fig. 13. The as-quenched Au-53 at.% Ni alloy. (a) BF image shows that decomposition has already started. Note that modulation perpendicular to g = [200] can be seen. (b) Electron diffraction pattern of (a). Satellite reflections along [100] are visible.

Fig. 14. (011) electron diffraction pattern of as-quenched Au-53 at.% Ni alloy. Note that satellite reflections are around every main spots along $[0\bar{1}1]$. There is no satellite spots along [100] in this area.

Fig. 15. (011) standard stereographic projection shows that the other two cube directions [010] and [001] lie in the same direction of $[0\bar{1}1]$.

Fig. 16. (a) The [001] zone axis of the as-quenched Au-53 at.% Ni alloy. (b) there is no modulation along (020) band. (c) There is some modulation along (200) band.

Fig. 17. the as-quenched Au-53 at.% Ni alloy. (a) With g = [200], strong modulation contrast can be seen. (b) With g = [020] operating in the same specimen area as in (a), the modulation contrast is not seen, indicating that only one-dimensional modulation along [100] is developed in this particular specimen area.

Fig. 18. The as-quenched Au-53 at.% Ni alloy. (a) BF image with g = $[11\bar{1}]$ shows modulation in the specimen. (b) The corresponding electron diffraction pattern. Satellite reflections along $[0\bar{1}1]$ can be seen.

Fig. 19. (a) The $(11\bar{1})$ lattice fringes of the circled area in Fig. 18(a). The large scale dark contrast is due to the composition waves along a certain cube direction. (b) Optical diffraction pattern of (a). Satellite reflections perpendicular to the modulation in (a) can be seen.

Fig. 20. The (200) lattice image of as-quenched Au-53 at.% Ni alloy. The large scale dark contrast is typical of spinodal decomposition at early stage.

Fig. 21. The (200) lattice image of another specimen area of as-quenched Au-53 at.% Ni alloy. There is no such kind of modulation as in Fig. 20.

Fig. 22. The (200) lattice image of as-quenched Au-53 at.% Ni alloy. A short range (100) fringe periodicity is observed in localized specimen area (arrowed). This is similar to that shown in Fig. 10.

Fig. 23. (a) BF image of Au-53 at.% Ni alloy aged 1 hr at 150°C. The modulation contrast is much stronger than that of the as-quenched specimen. (b) The corresponding (001) electron diffraction pattern shows satellite reflections around main spots along [100].

Fig. 24. The (200) lattice fringe image of Au-53 at.% Ni alloy aged 1 hr at 150°C. This is typical of spinodal decomposition.

Fig. 25. Two different sets of fringes are imaged in the same specimen area to show only one-dimensional composition waves are developed in this particular region. (a) Modulations in the image and satellite reflections along [100] in the optical diffraction pattern can be seen when (200) fringes are imaged, While in (b), no such kind of effect can be seen when (020) fringes are imaged. Thus, there is only modulation along [100] in this specimen area.

Fig. 26. BF image of Au-53 at.% Ni alloy aged 4000 hr at 150°C. The avelength is ~55Å and the modulation seems to remain one-dimensional.

Fig. 27. The log-log plot of wavelength vs aging time. The slope is quite low and the relationship between wavelength and aging time obeys the law $\lambda \propto t^{1/10}$ which is a result of one-dimensional coarsening.

Fig. 28. The (200) lattice image of Au-53 at.% Ni alloy aged 1 hr at 150°C.

Fig. 29. A comparison of electron and optical diffraction patterns taken from Fig. 28. Satellite reflections can be seen along [100].

Fig. 30. Direct microdensitometer trace analysis of Fig. 28. The ragged shape may originate from inaccuracy of fringe spacing measurements.

Fig. 31. A smoothed curve of Fig. 30 by taking average value over 10 fringe spacings at a time. The overall profile is preserved and this represents an early stage decomposition behavior. It is characterized by small composition amplitude ($\Delta a \sim 6.5\%$) and diffuse interface.

Fig. 32. Results of an optical microdiffraction analysis of Fig. 28. By moving an aperture equivalent to ~30Å at the specimen plane in ~20Å increments normal to the fringe. A periodic variation in spacing is produced. The central pattern is taken with large aperture such that satellites can be seen.

Fig. 33. (a) The (200) lattice image of Au-53 at.% Ni alloy aged 100 hr at 150°C. (b) The corresponding electron diffraction pattern shows satellite reflections along [100].

Fig. 34. Direct microdensitometer trace analysis of fringe spacing in Fig. 33. The ragged shape is similar to that in Fig. 30, but there is a noticable increase in amplitude due to decomposition.

Fig. 35. The smoothed curve of Fig. 34 by taking average value over 10 fringe spacings at a time. The composition amplitude increases ($\Delta a \sim 12\%$) and reaches the equilibrium tie-line compositions. This represents a later stage of decomposition which is characterized by sharp interface and large composition amplitude.

Fig. 36. Results of an optical microdiffraction analysis of Fig. 23. the aperture size is the same as that in Fig. 32. Note that the measured difference in fringe spacings is also ~12%.

Fig. 37. Schematic representation of the one-dimensional modulation model. The crystal is divided into several representative gains. Within each gain, small domains of one-dimensional waves are developed which do not interpenetrate.

Fig. 38. (a) Strong modulation perpendicular to g = [020] is observed of a Cu-Ni-Cr spinodal alloy, but it is not observed with g = [200] in the same specimen area. This suggests that a possible one-dimensional modulation is developed in this alloy system as well.

Fig. 39. Summary of the changes that occur in a yield stress, curie temperature and wavelength for an asymmetric Cu-Ni-Fe spinodal alloy. Note that prior to 10 hr aging the shape of the wavelength vs time curve is similar to that in Fig. 27 which is a result of one-dimensional coarsening.

Fig. 40. Schematic representation of the characteristics of spinodal decomposition plotted as concentration against distance (1) early stage, (2) later stage.

Fig. 41. The typical spinodal microstructure, (a) early stage, and (b) later stage. It is also suggested that the wavy appearance of the second phase in (a) is due to one-dimensional modulation, while the cuboid-like particles in (b) is obviously due to multi-dimensional coarsening reaction.

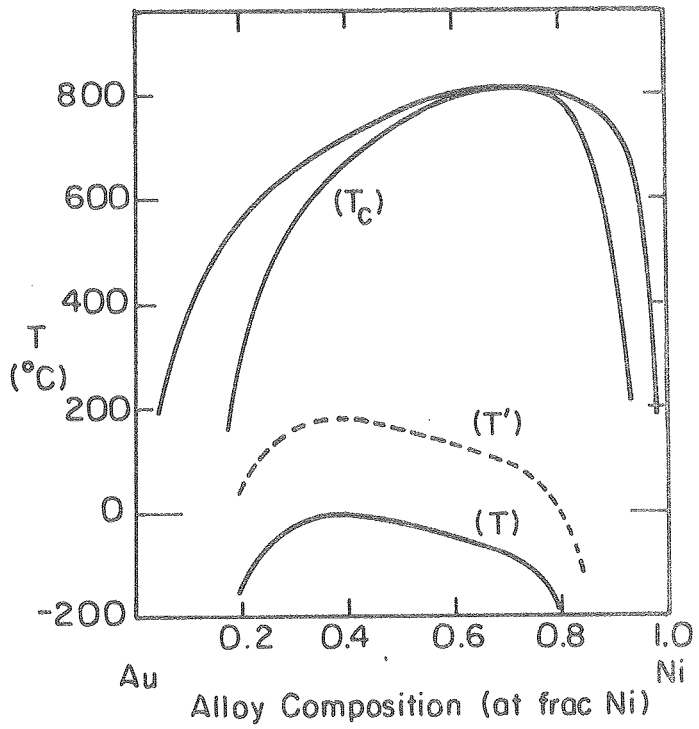

XBL 788-5693

Fig. 1

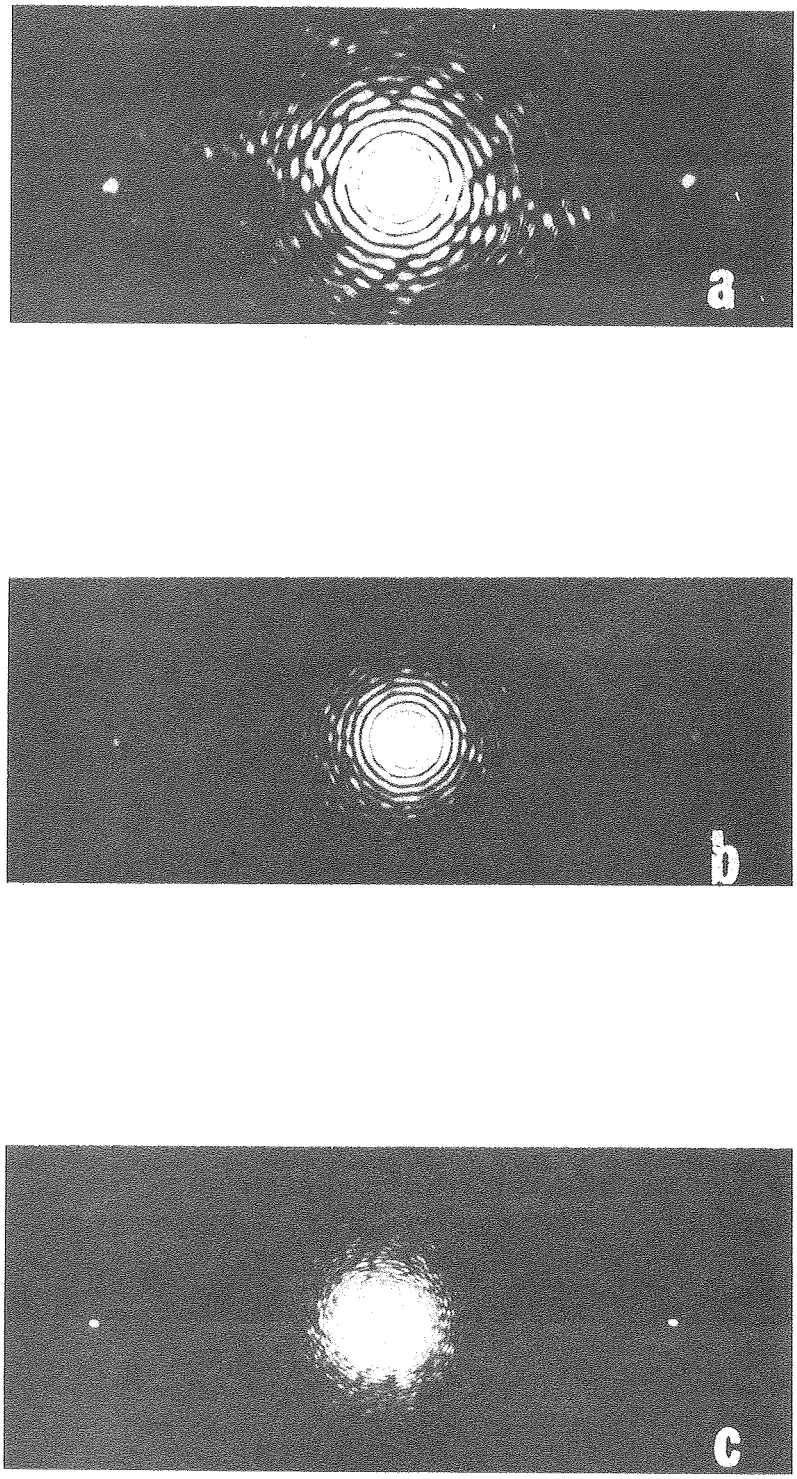

XBB 760-10144

Fig. 2

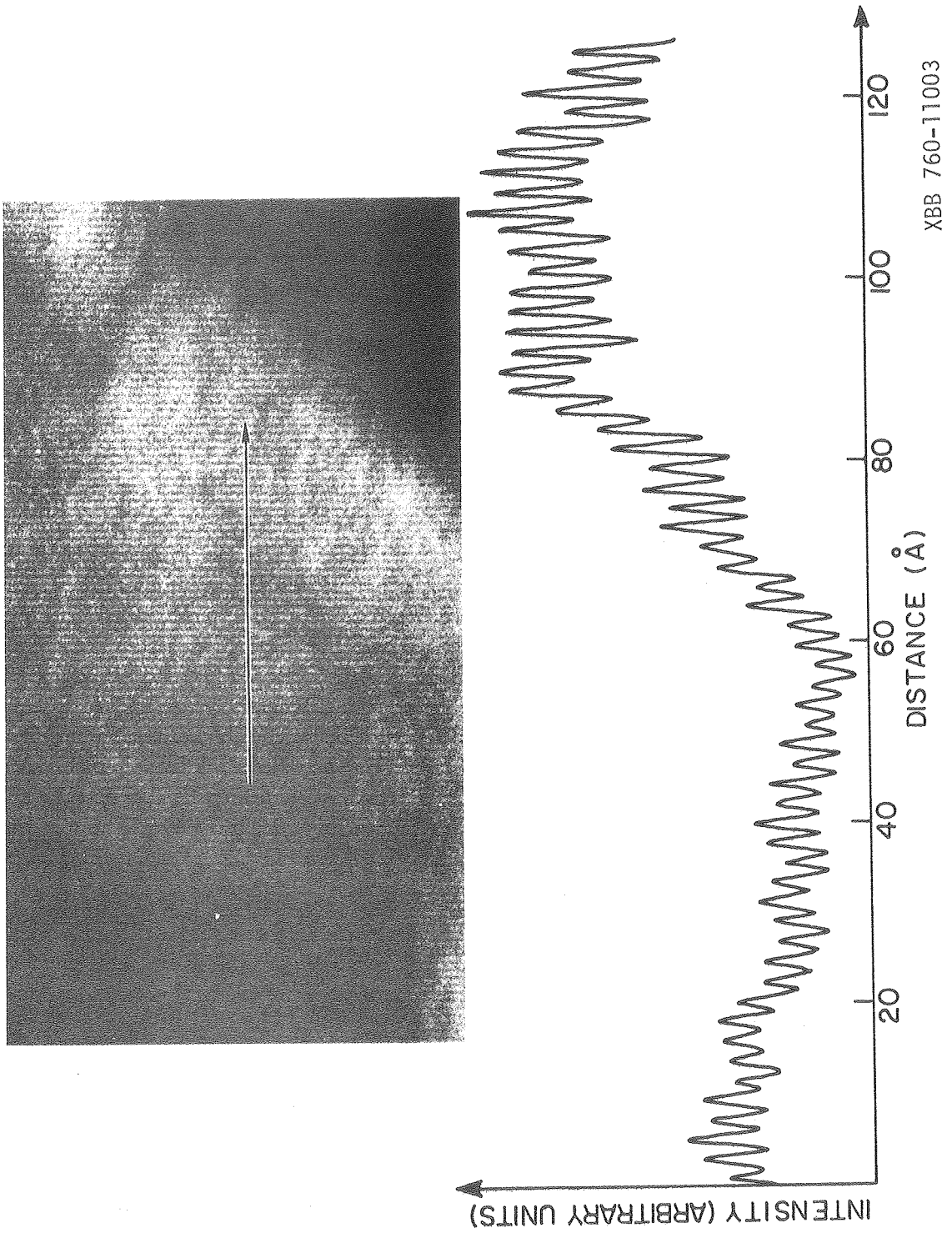
INTENSITY (ARBITRARY UNITS)
20
40
60
80
100
120
DISTANCE (Å)
XBB 760-11003

Fig. 3

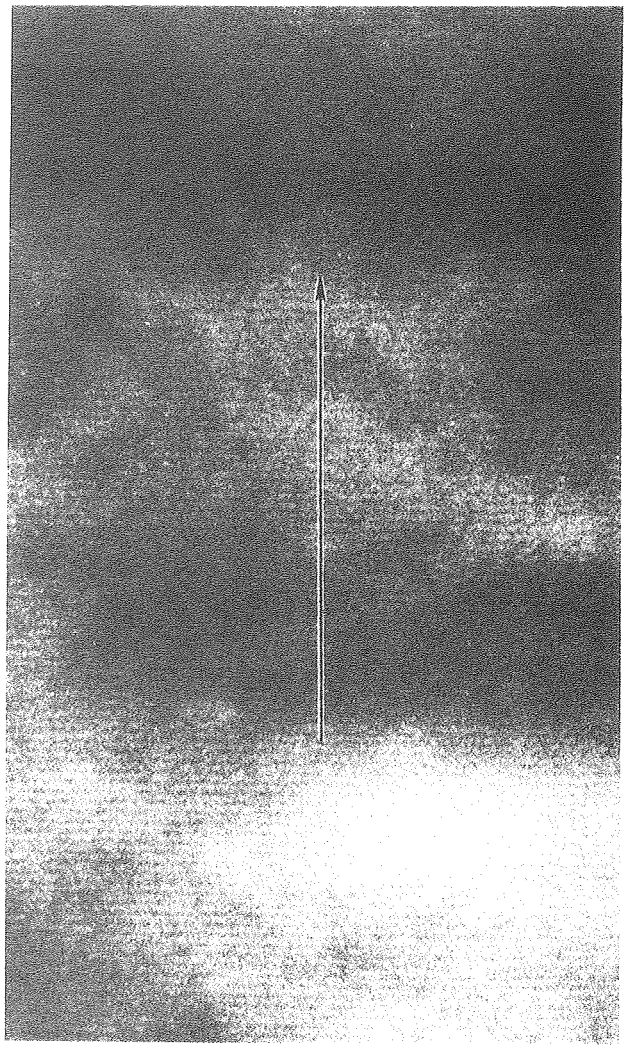

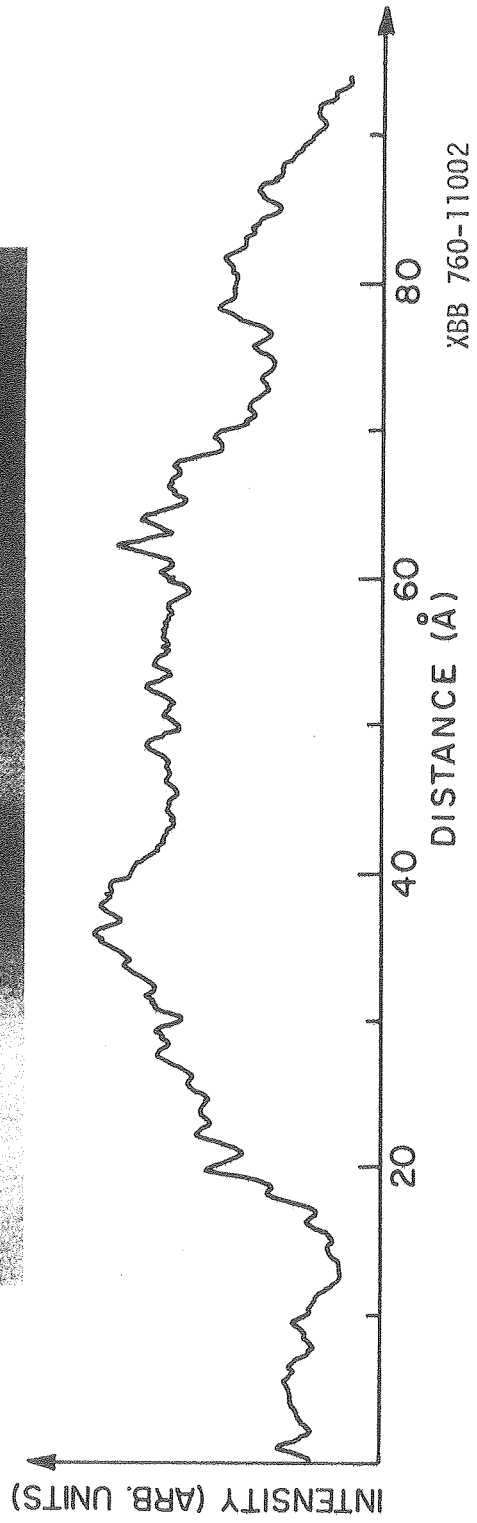

Fig. 4

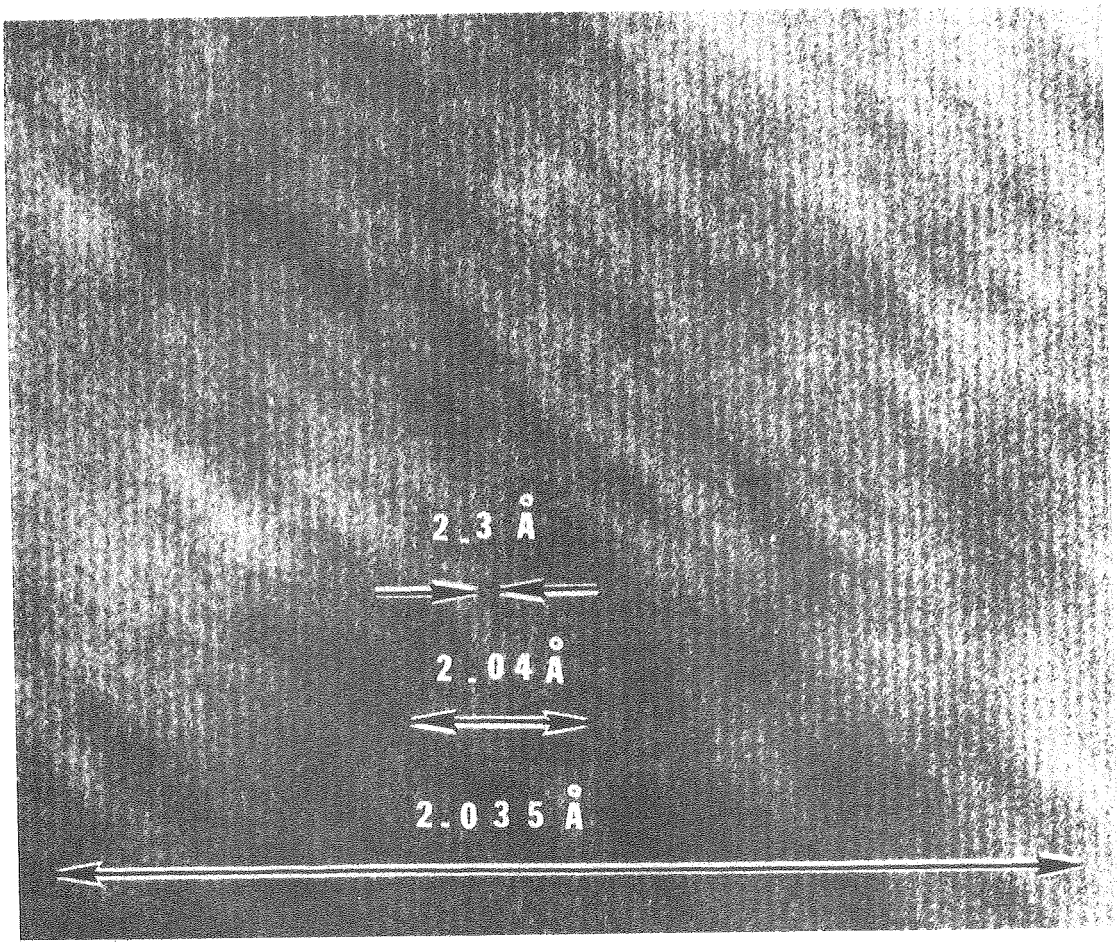

XBB 780-12876

Fig. 5

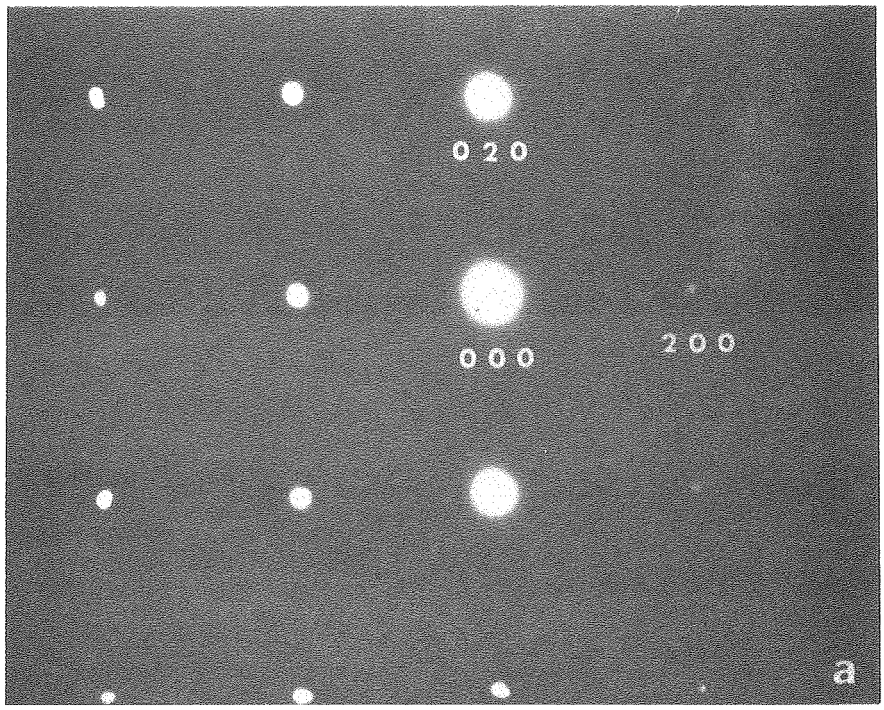

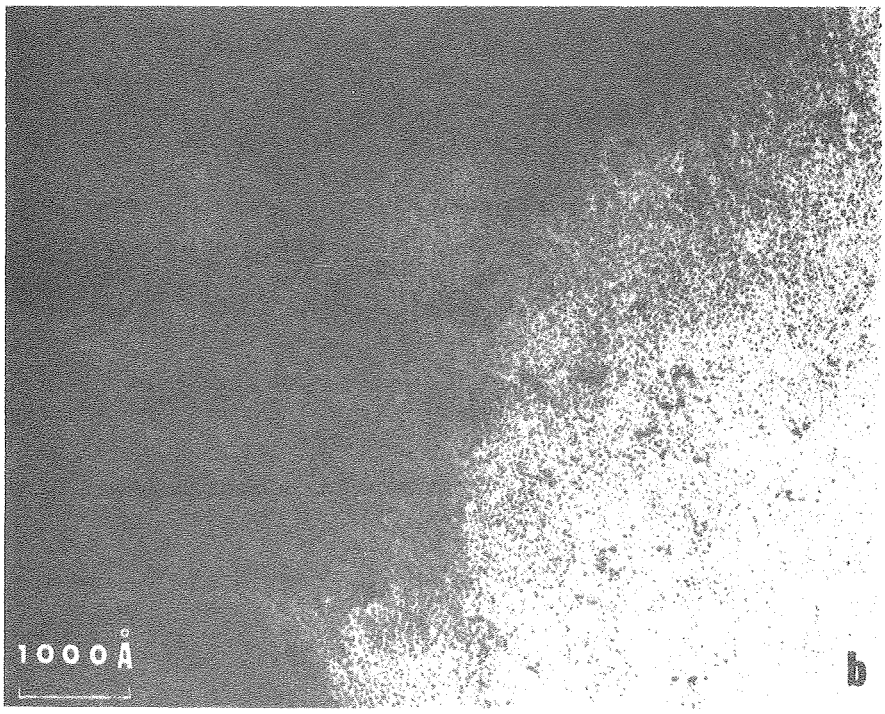

XBB 780-12885

Fig. 6

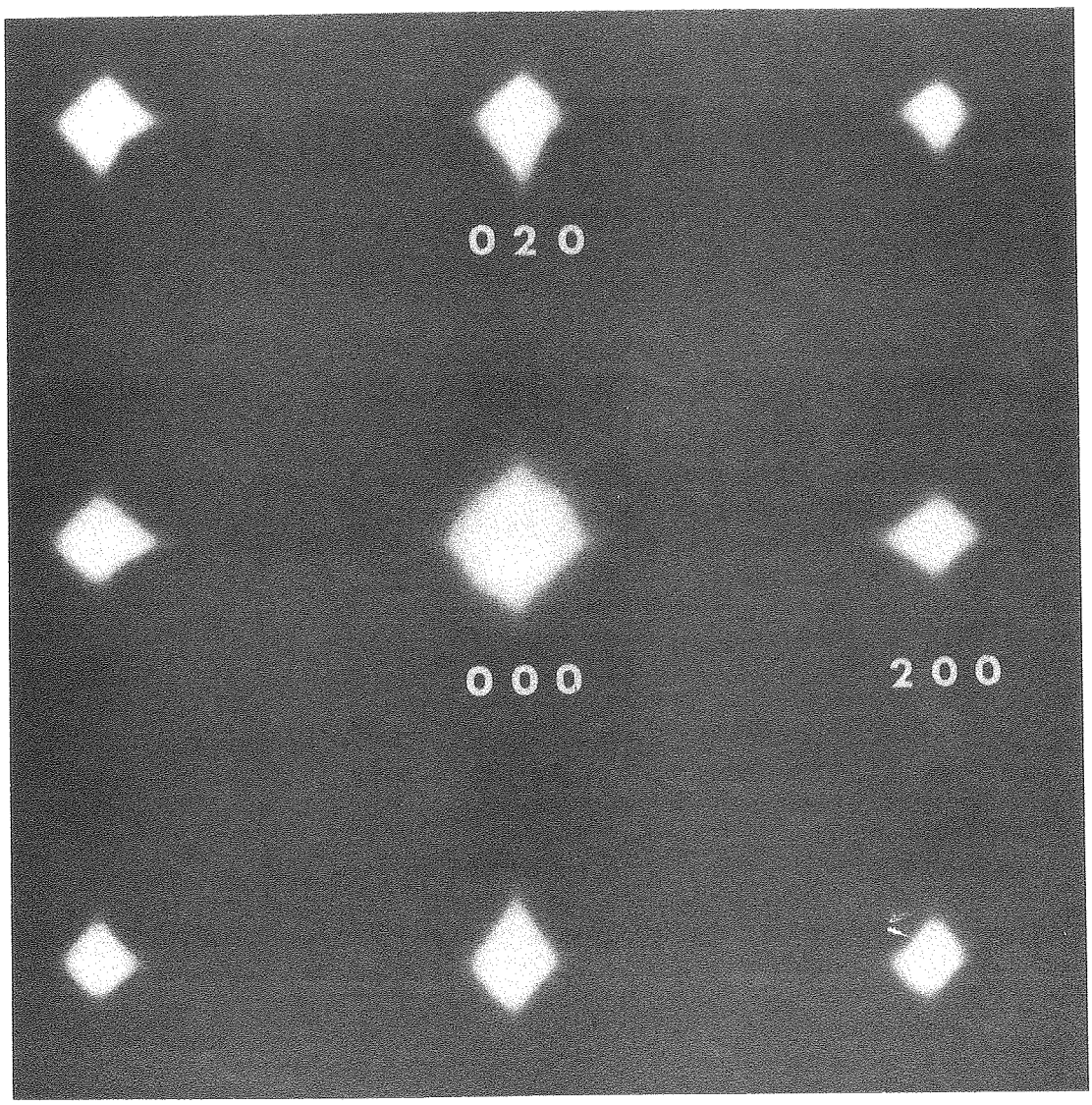

XBB 780-12895

Fig. 7

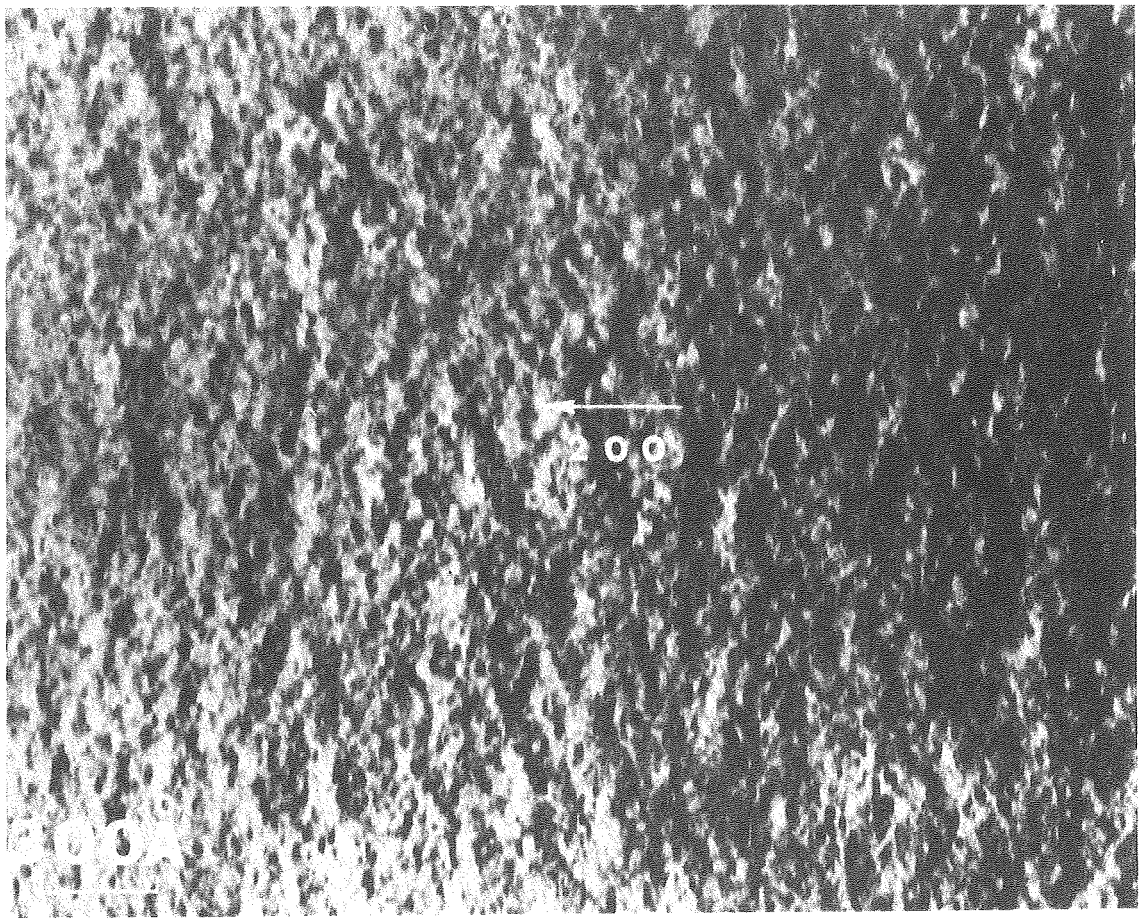

XBB 780-12878

Fig. 8

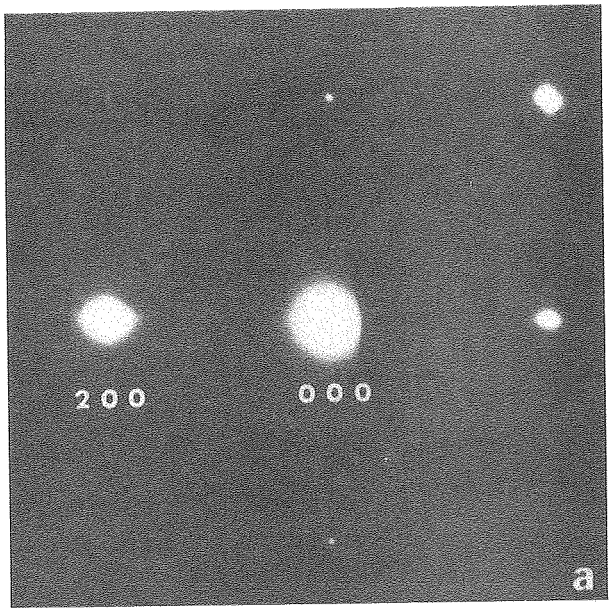

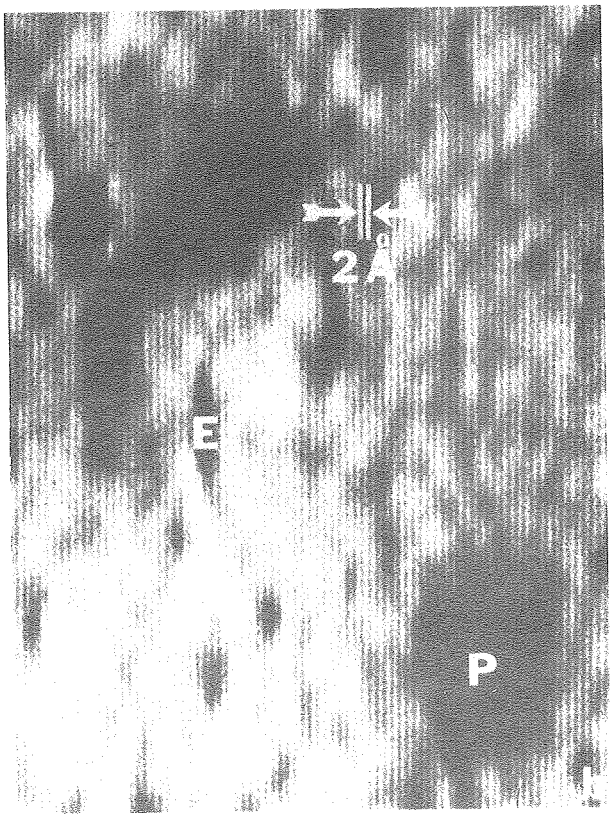

XBB 780-12872

Fig. 9

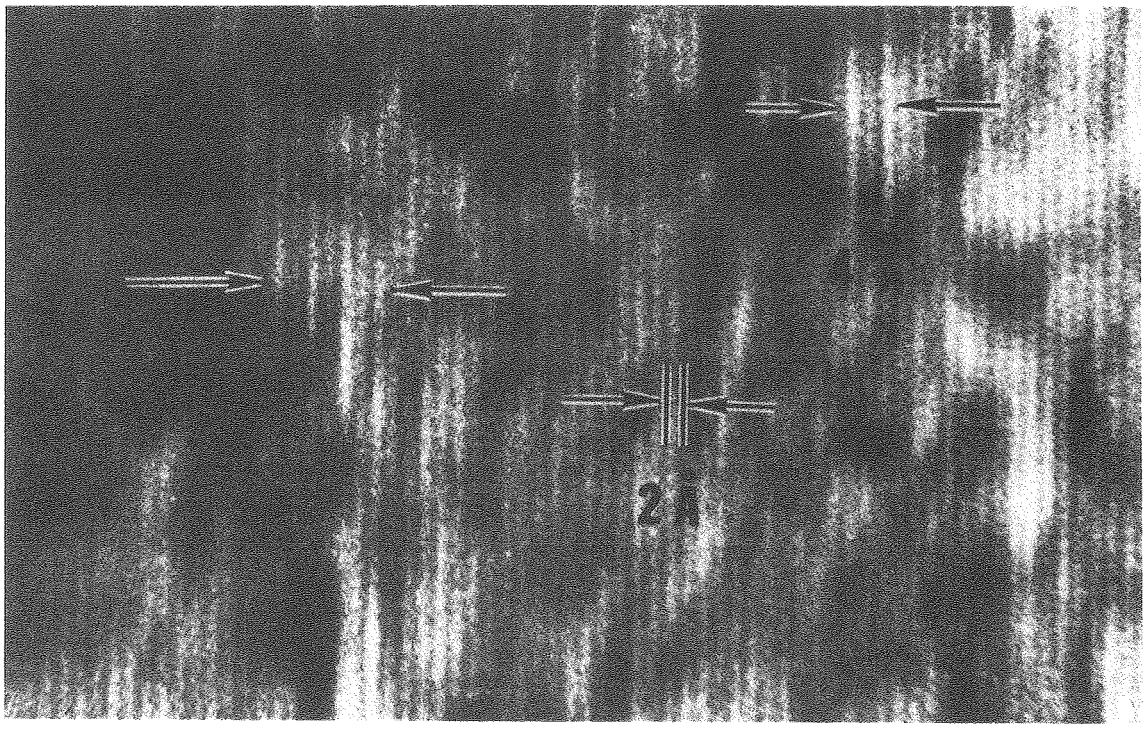

XBB 780-12880

Fig. 10

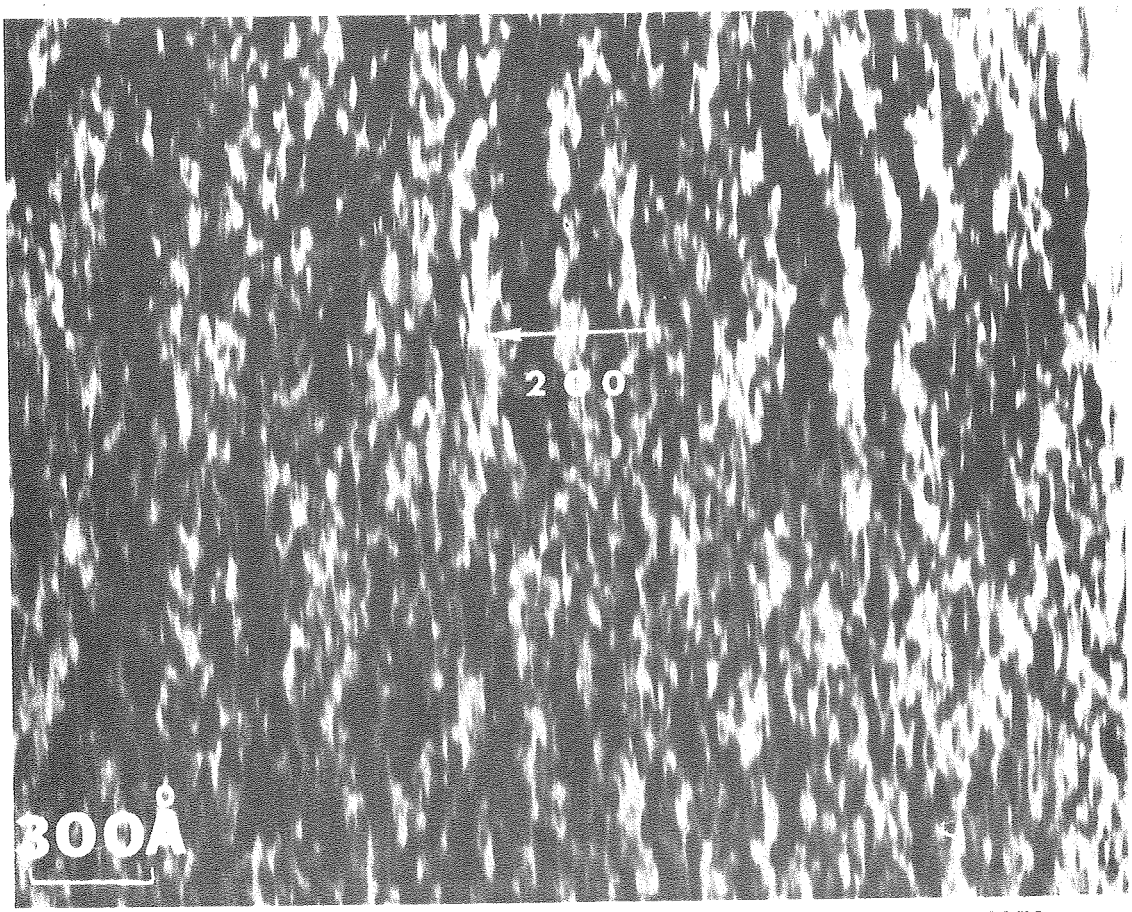

XBB 780-12879

Fig. 11

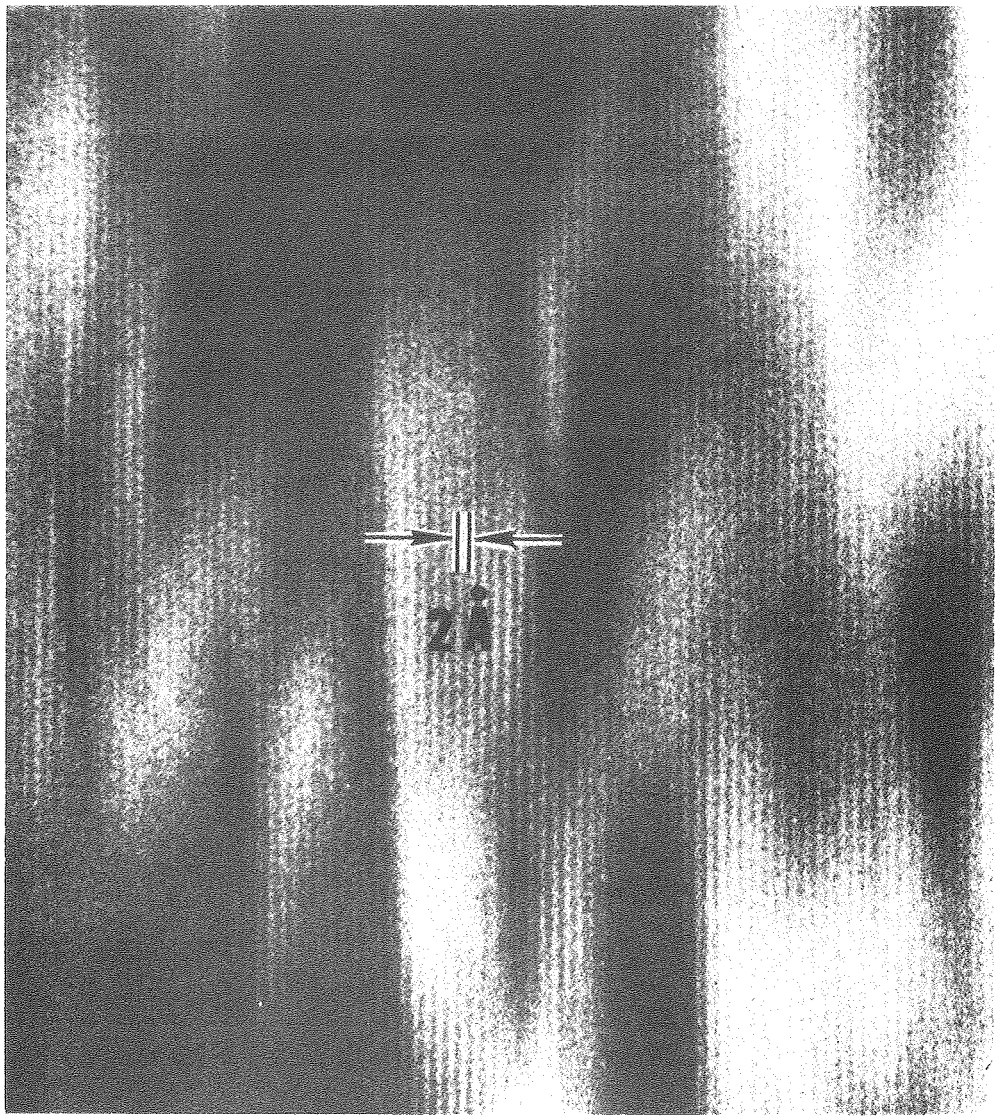

XBB 780-12881

Fig. 12

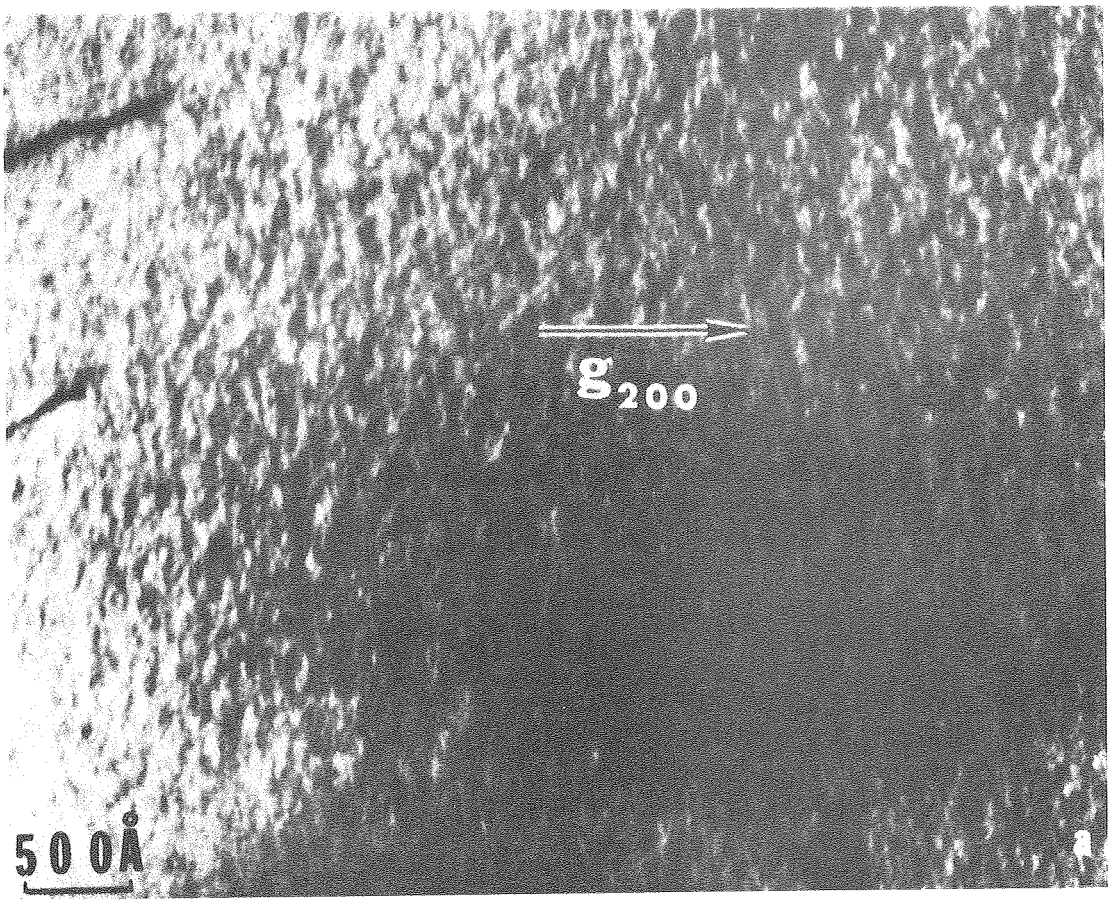

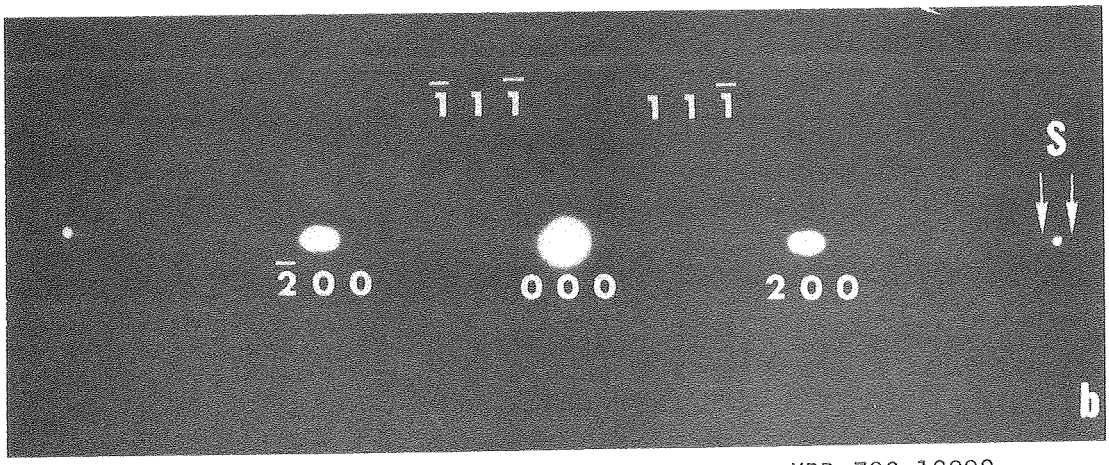

XBB 780-12882

Fig. 13

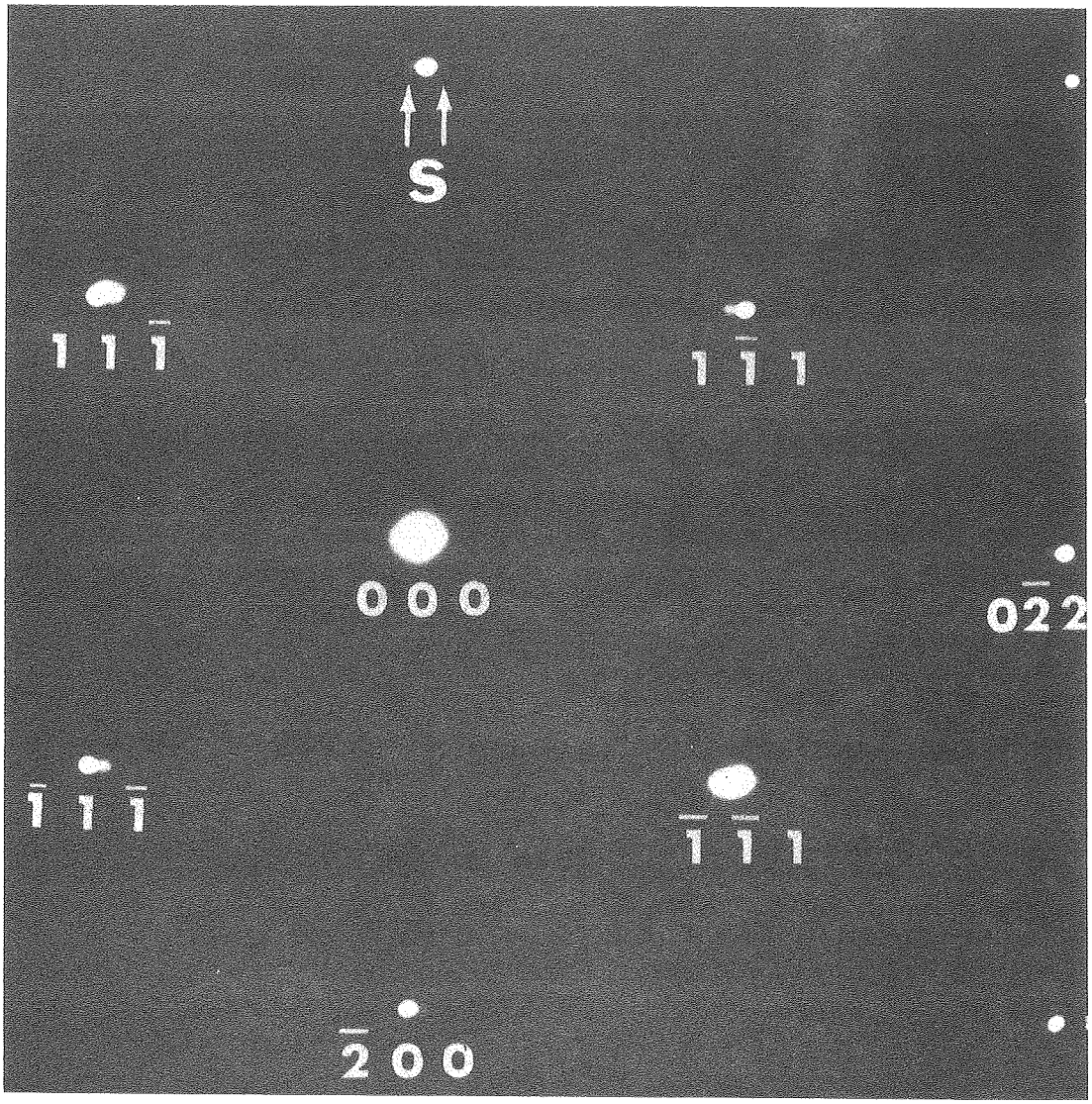

XBB 780-12877

Fig. 14

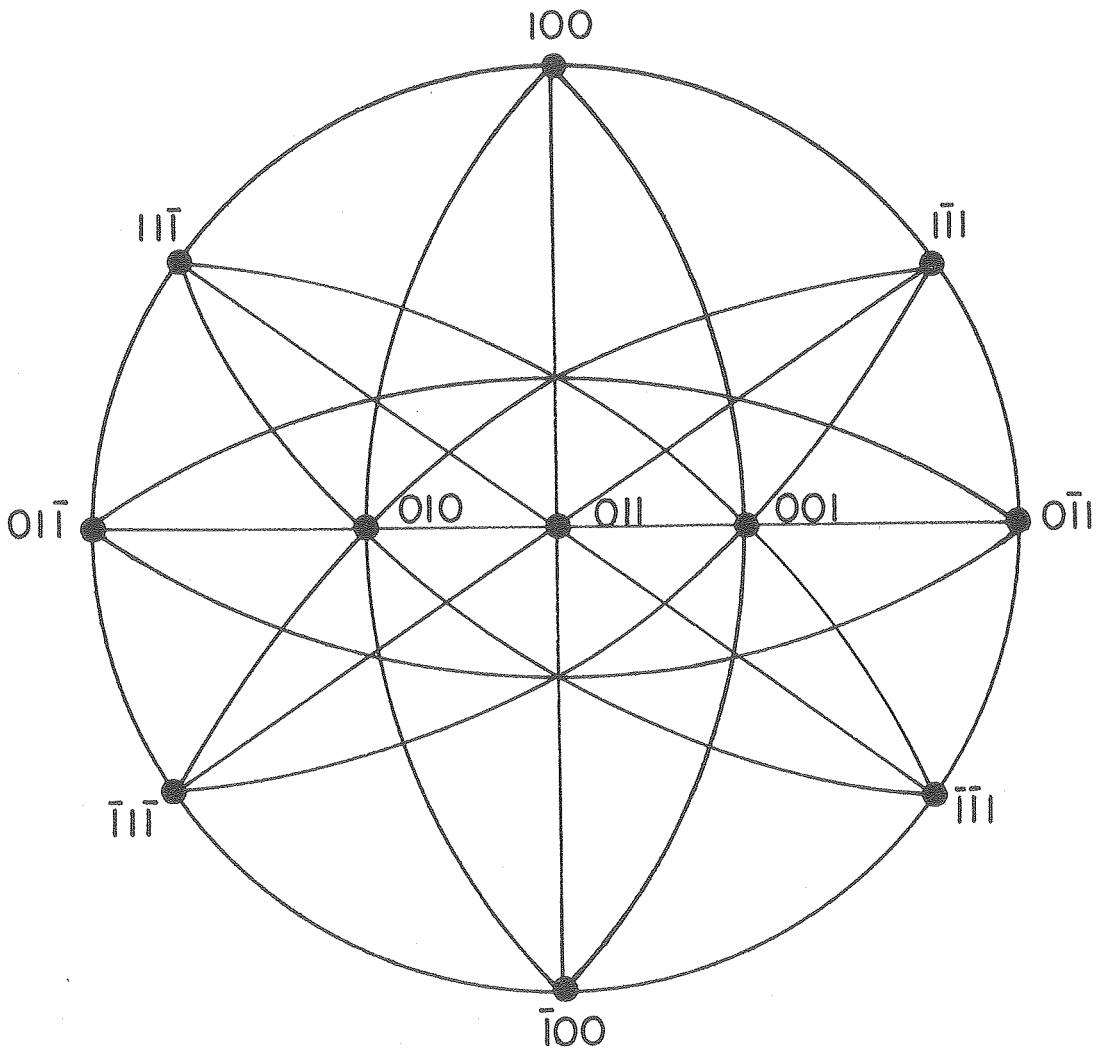

XBL789-5789

Fig. 15

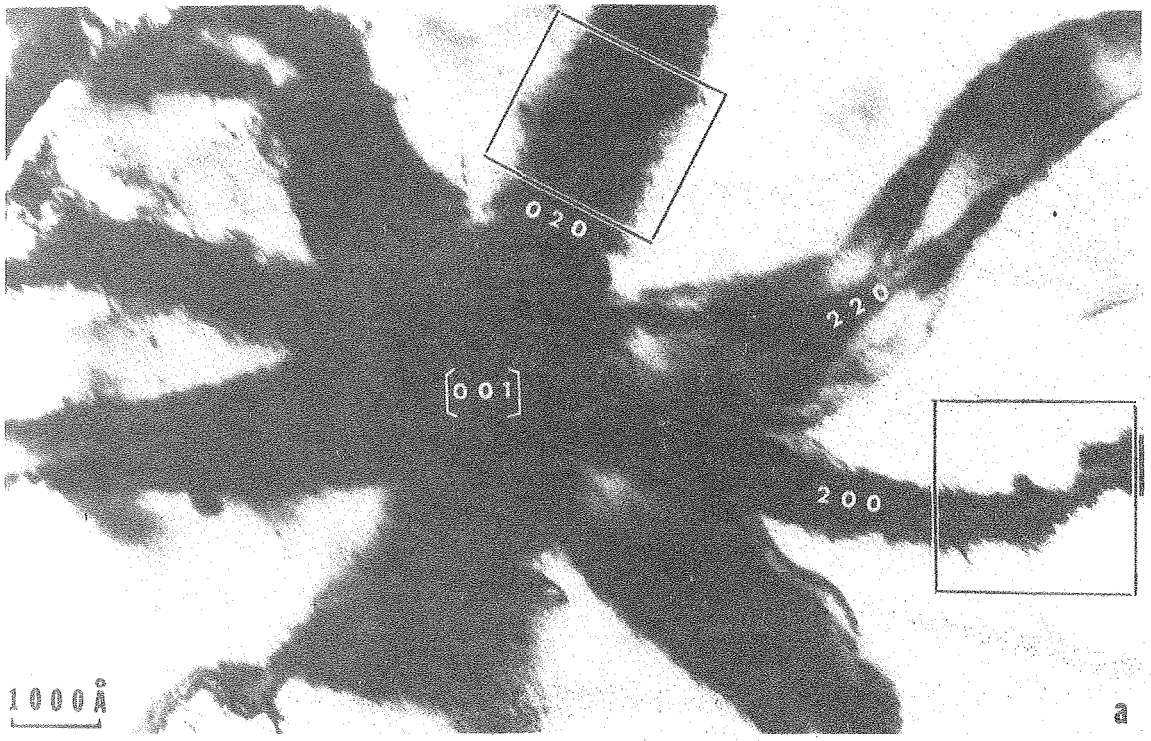

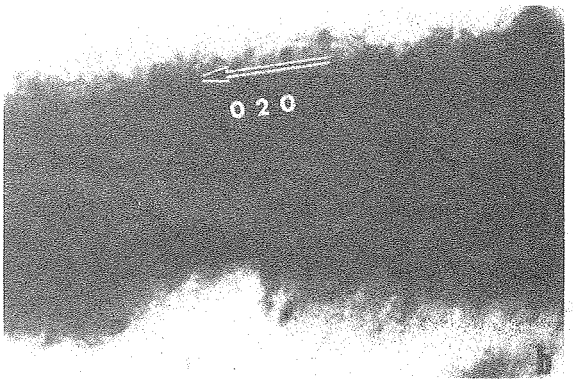

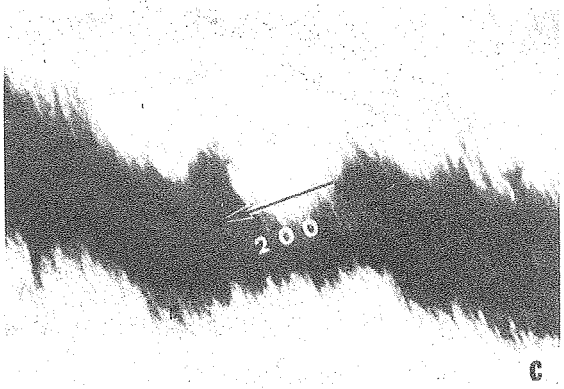

XBB 780-12888

Fig. 16

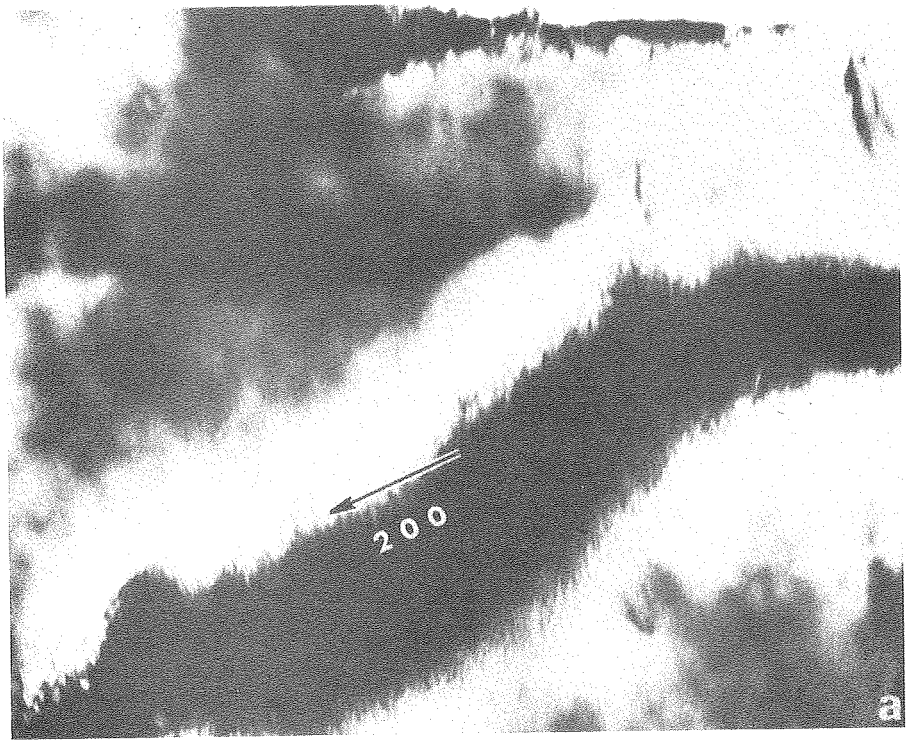

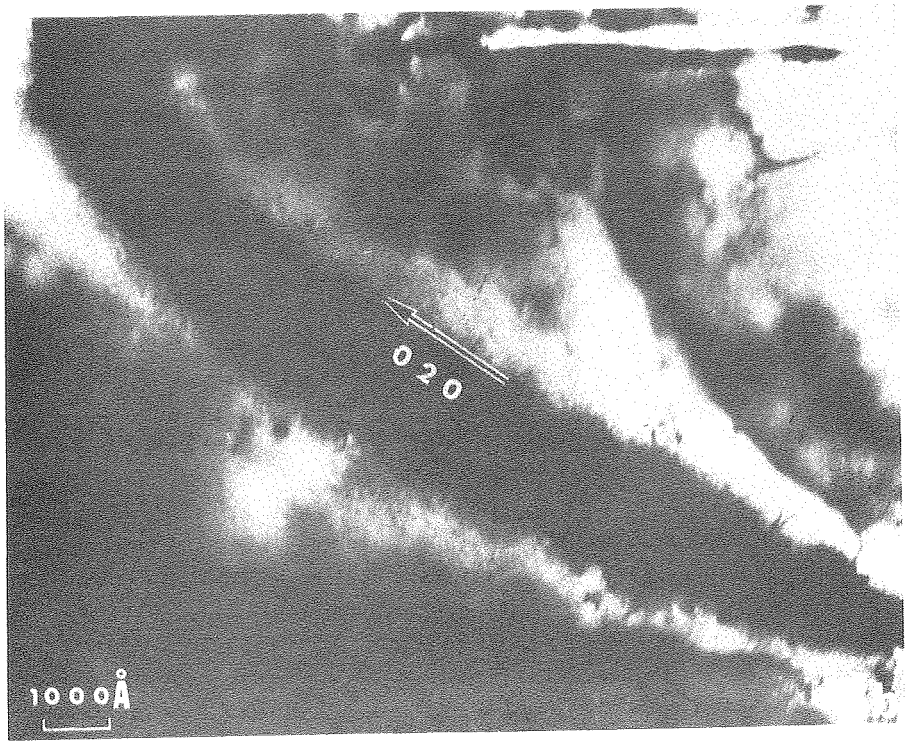

XBB 780-12874

Fig. 17

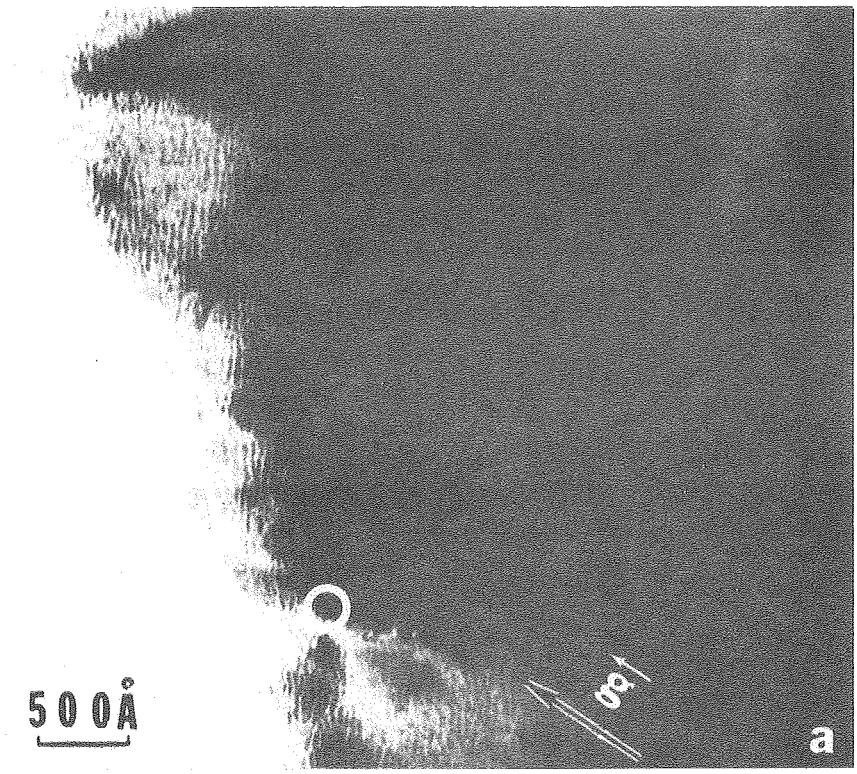

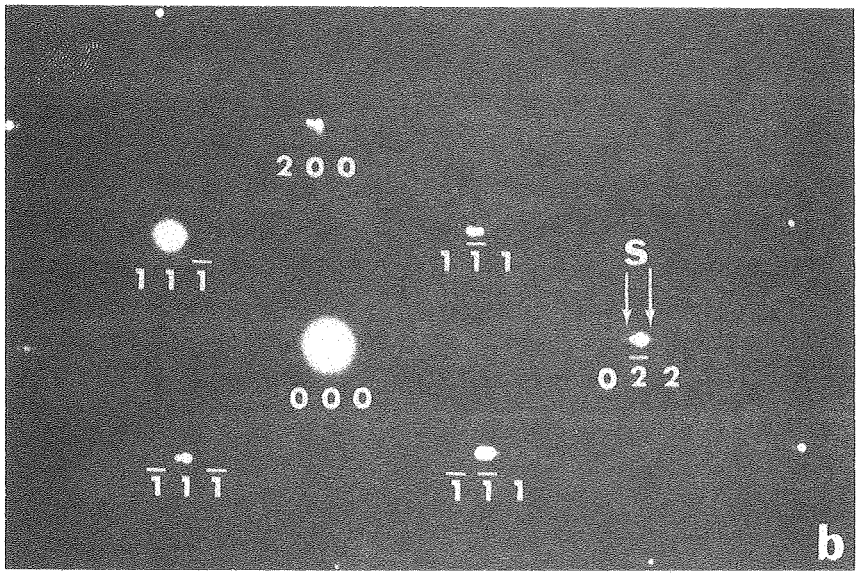

XBB 780-12883

Fig. 18

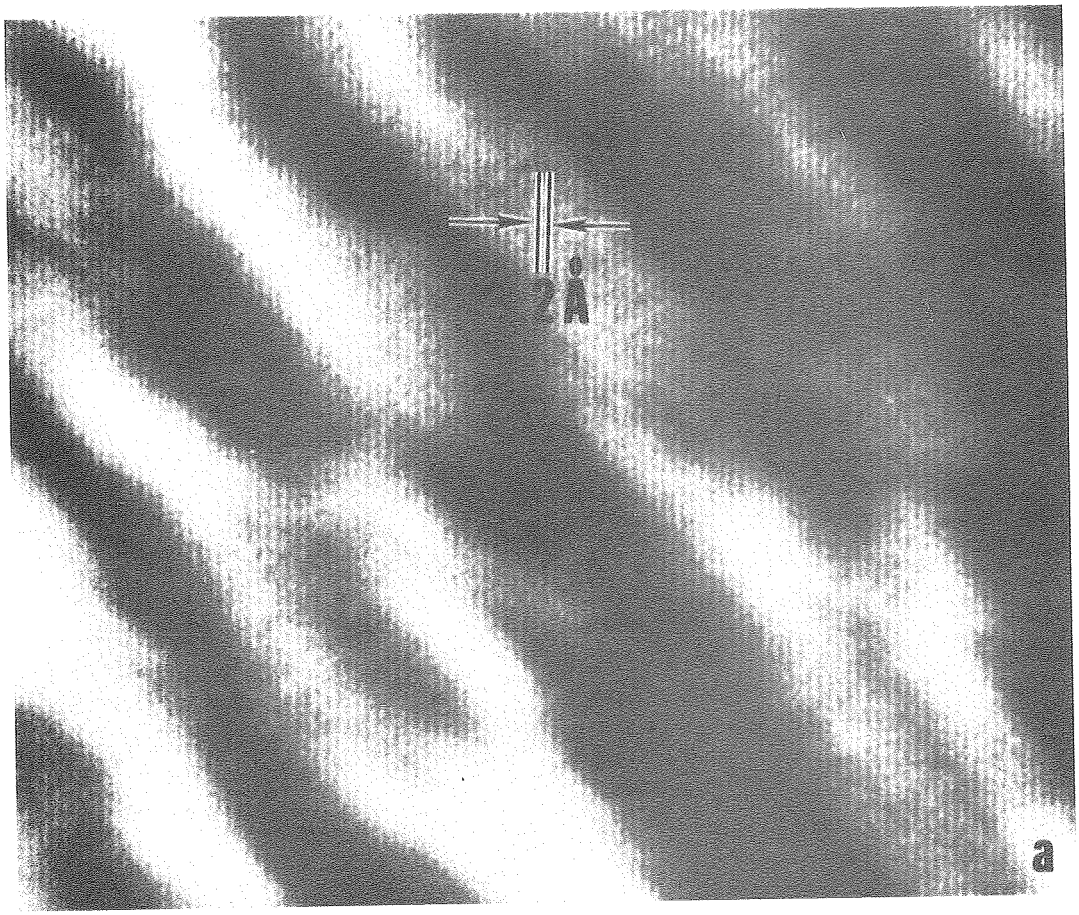

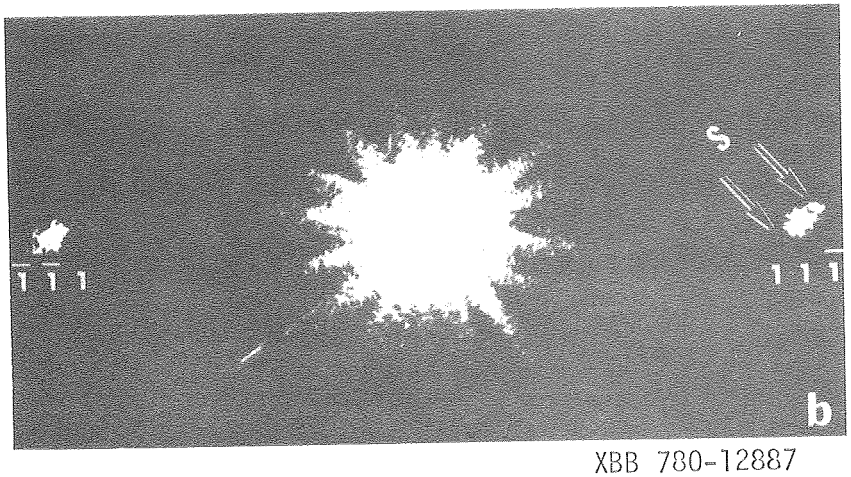

XBB 780-12887

Fig. 19

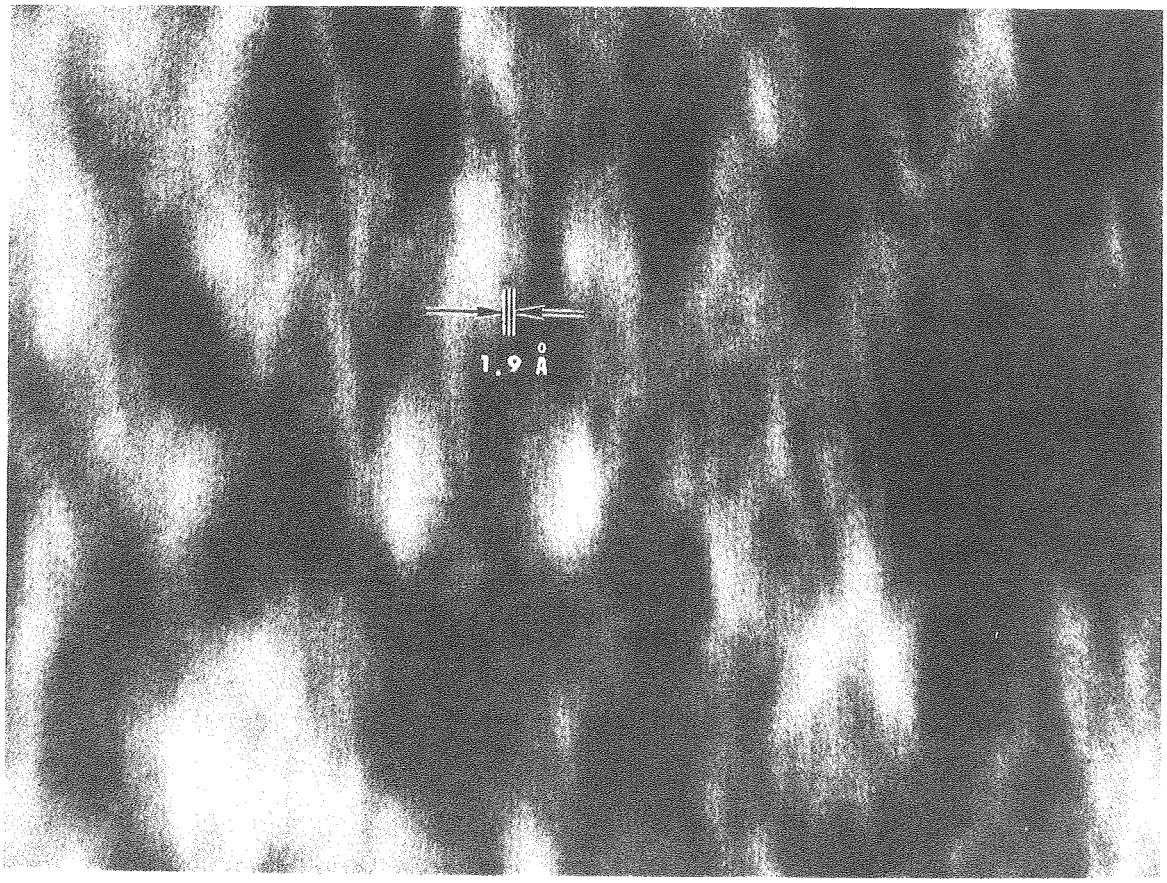

XBB 780-12884

Fig. 20

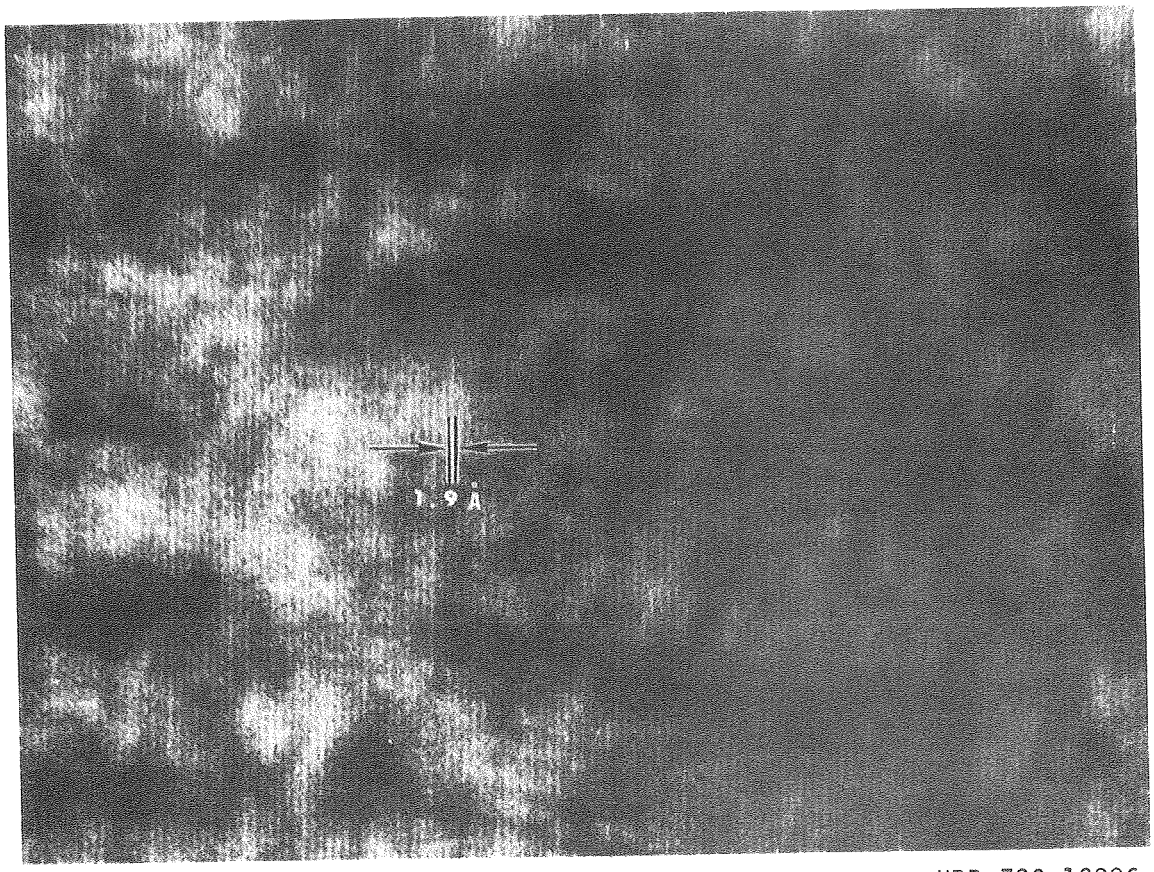

XBB 780-12886

Fig. 21

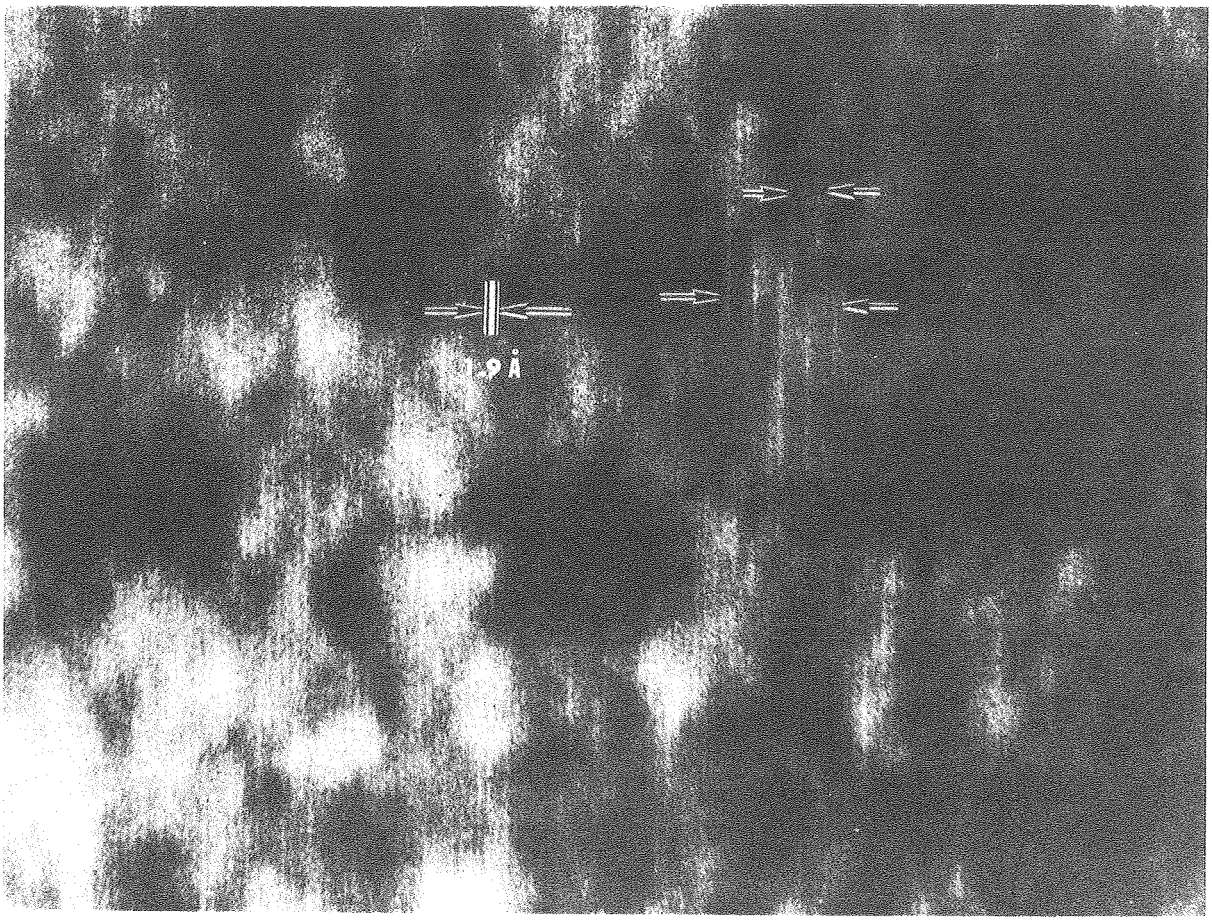

XBB 780-12873

Fig. 22

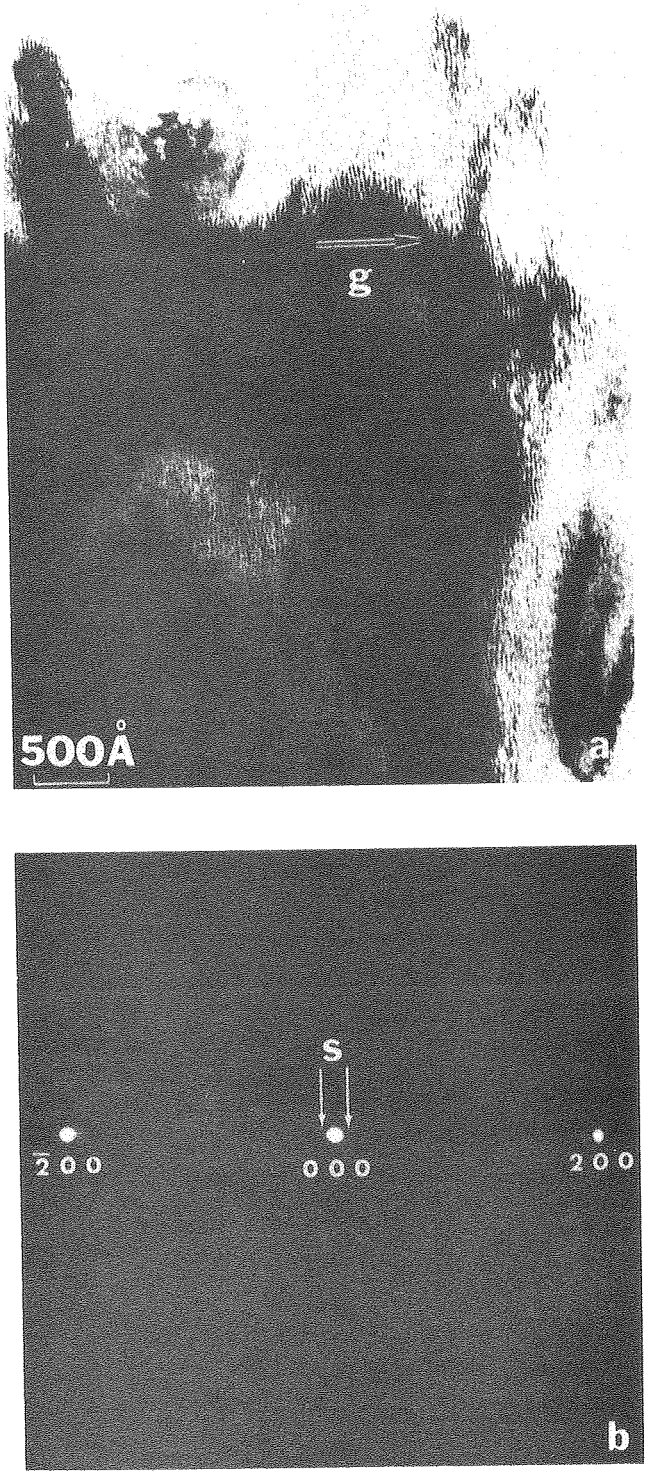

XBB 780-12875

Fig. 23

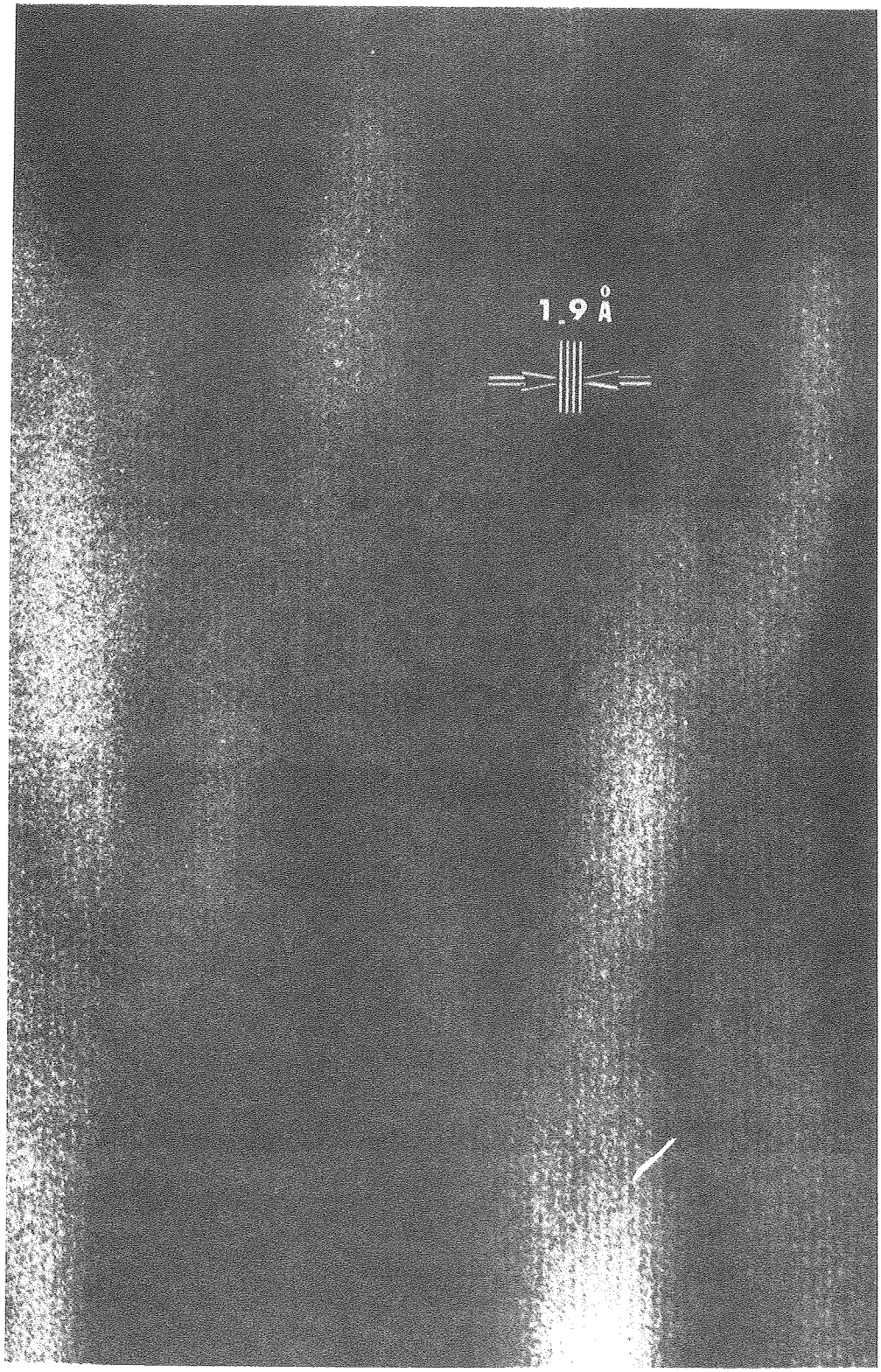

XBB 780-12891

Fig. 24

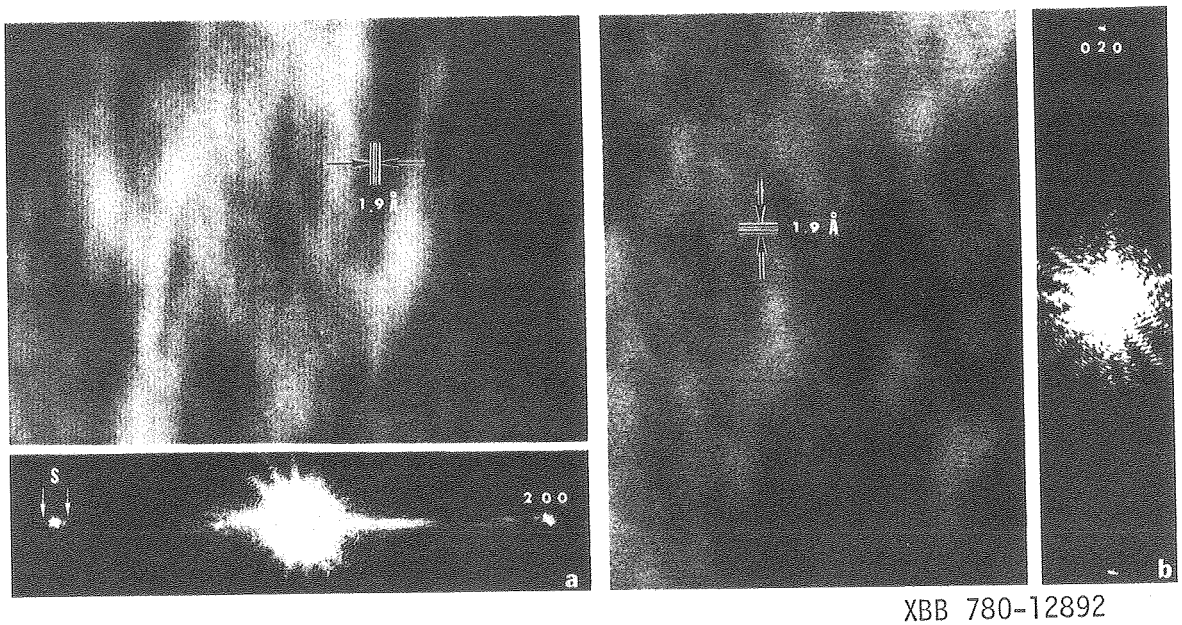

XBB 780-12892

Fig. 25

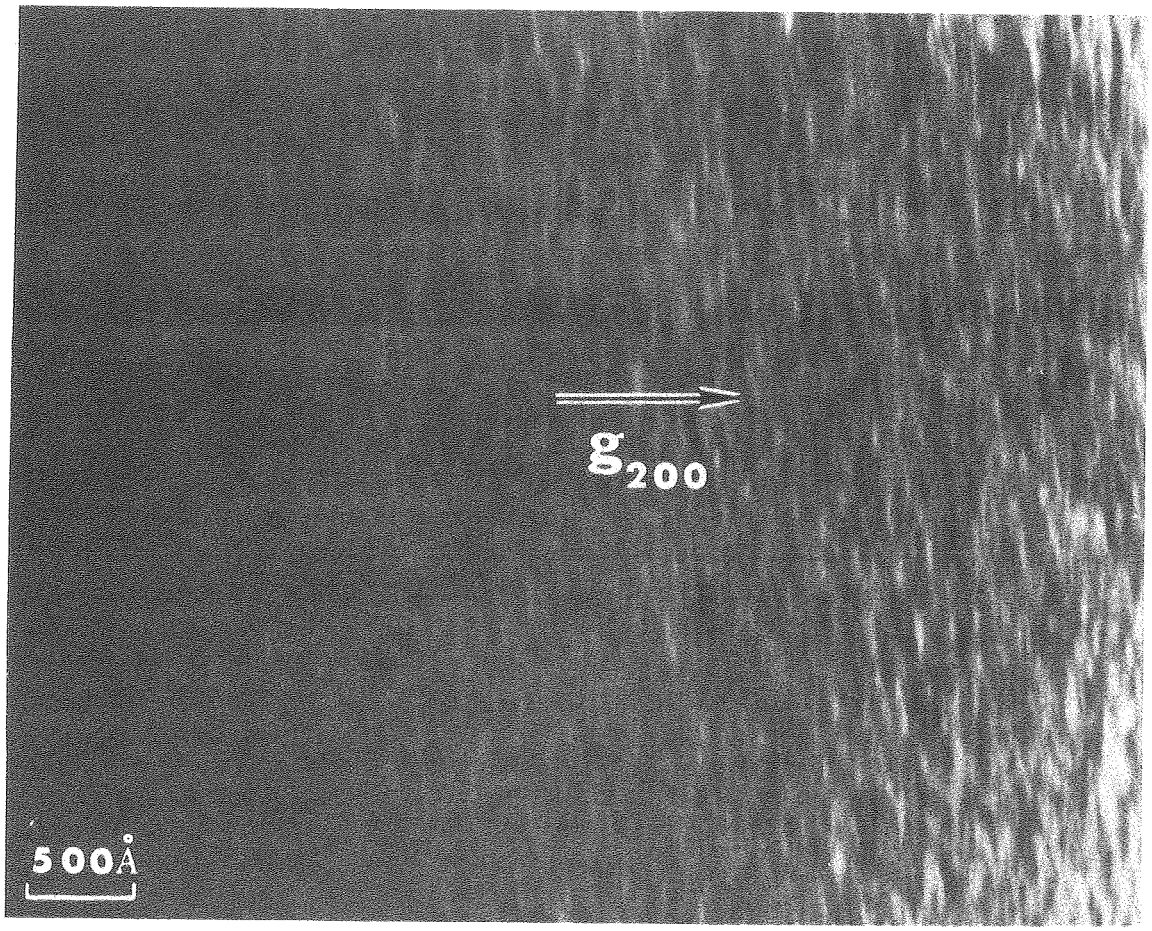

XBB 780-12889

Fig. 26

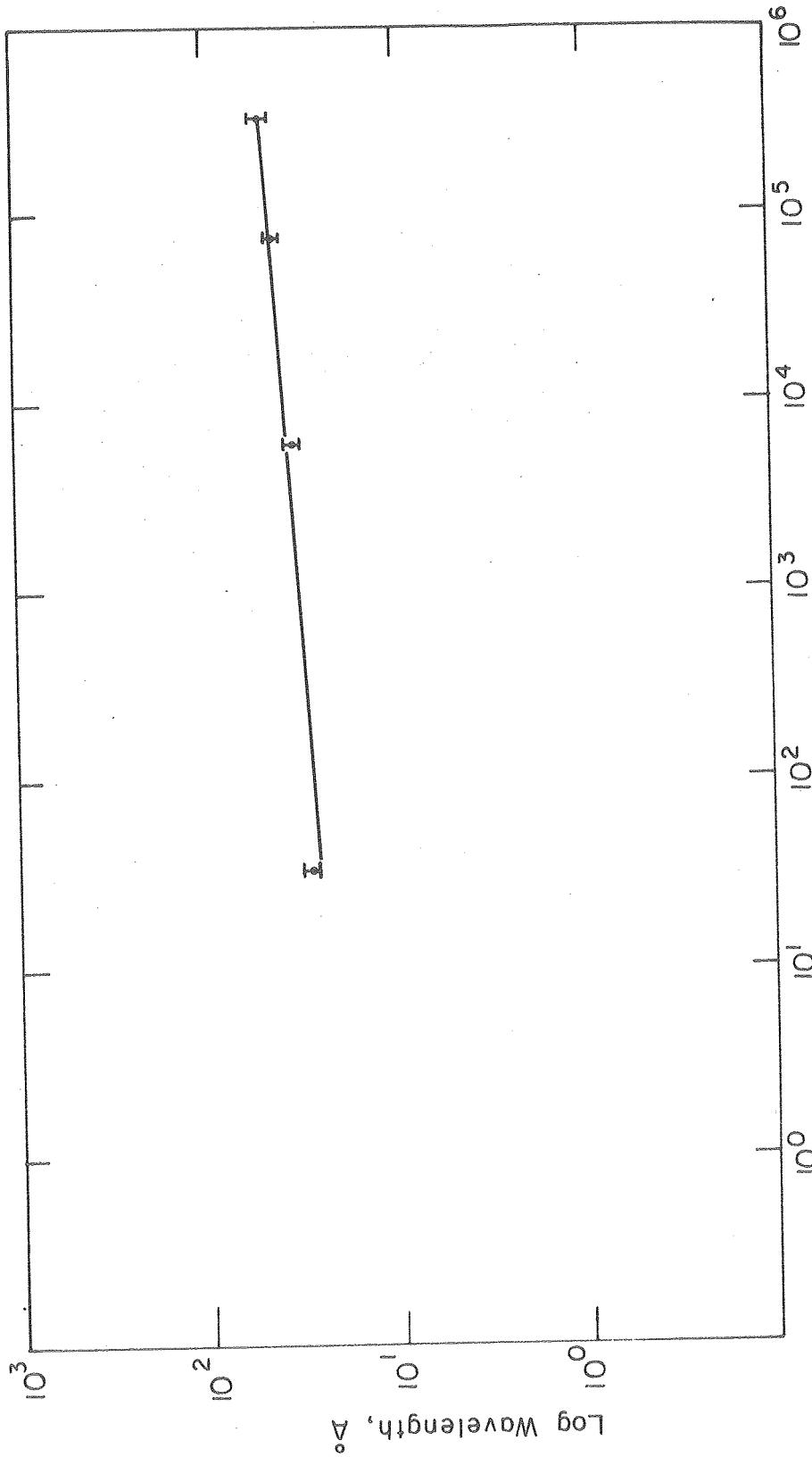

XBL782-4661

Fig. 27

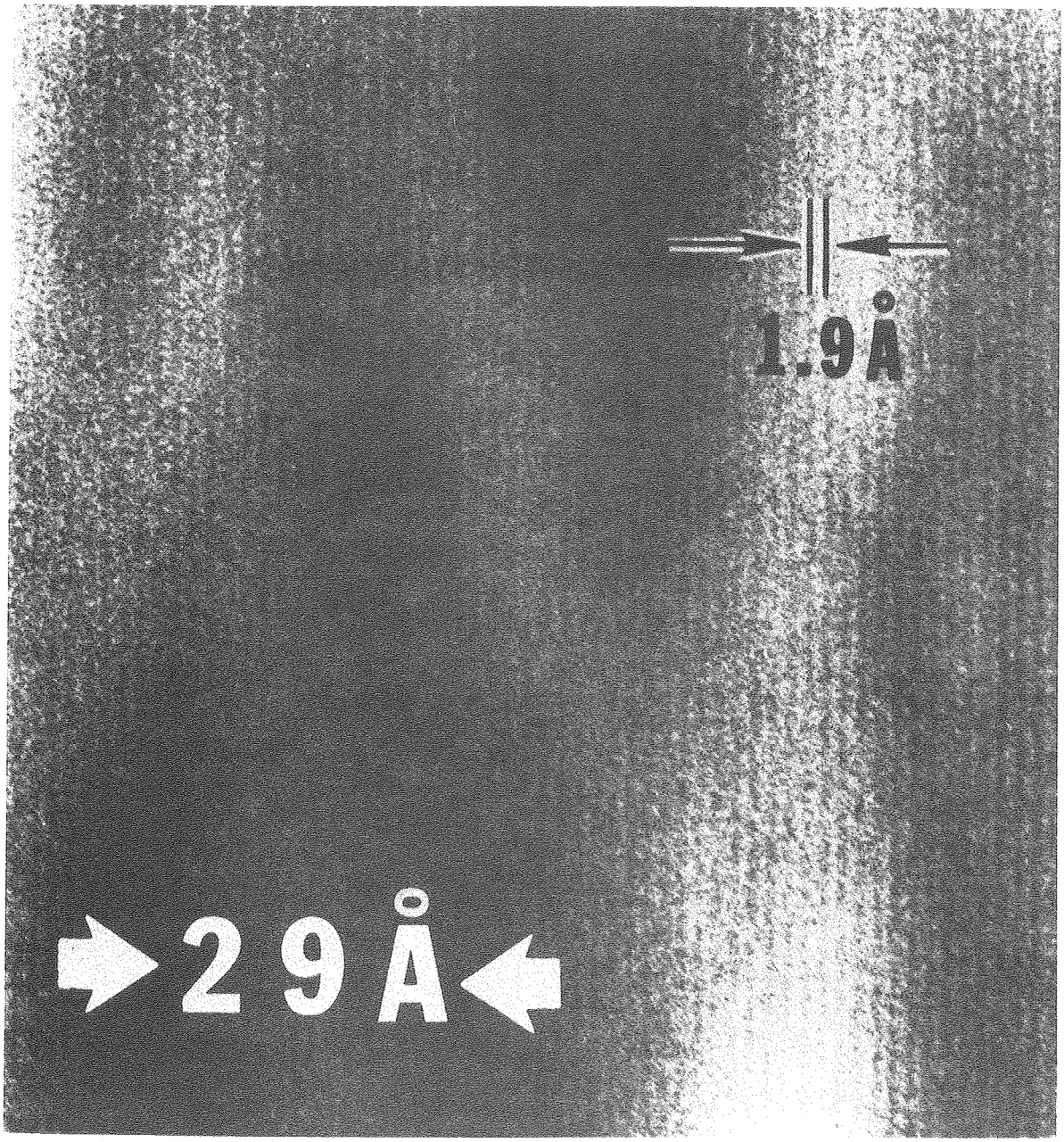

XBB 780-12871

Fig. 28

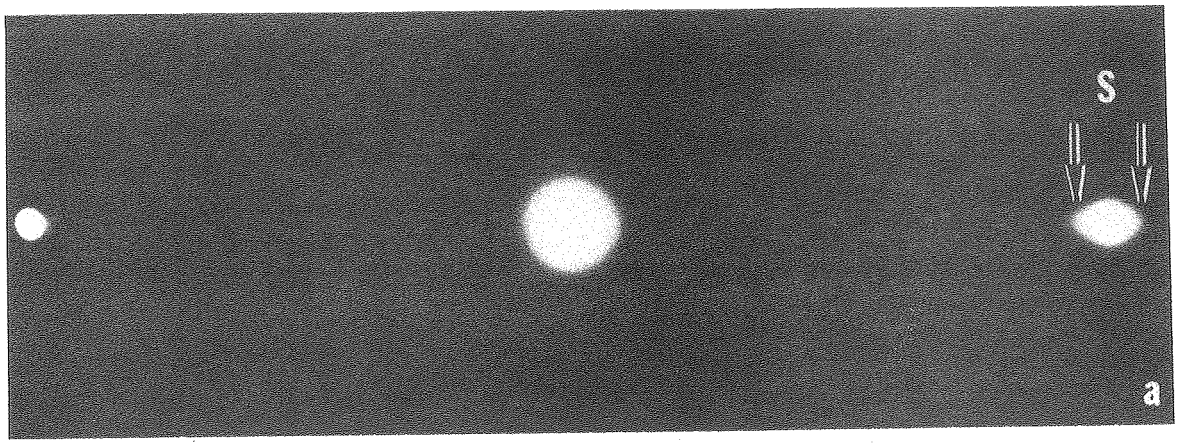

$\bar{2}00$ 000 200

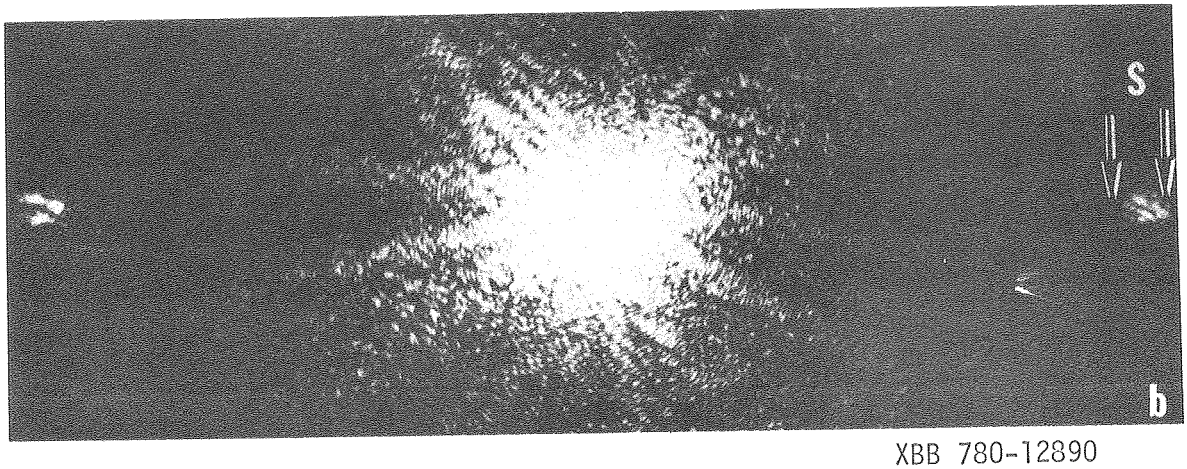

XBB 780-12890

Fig. 29

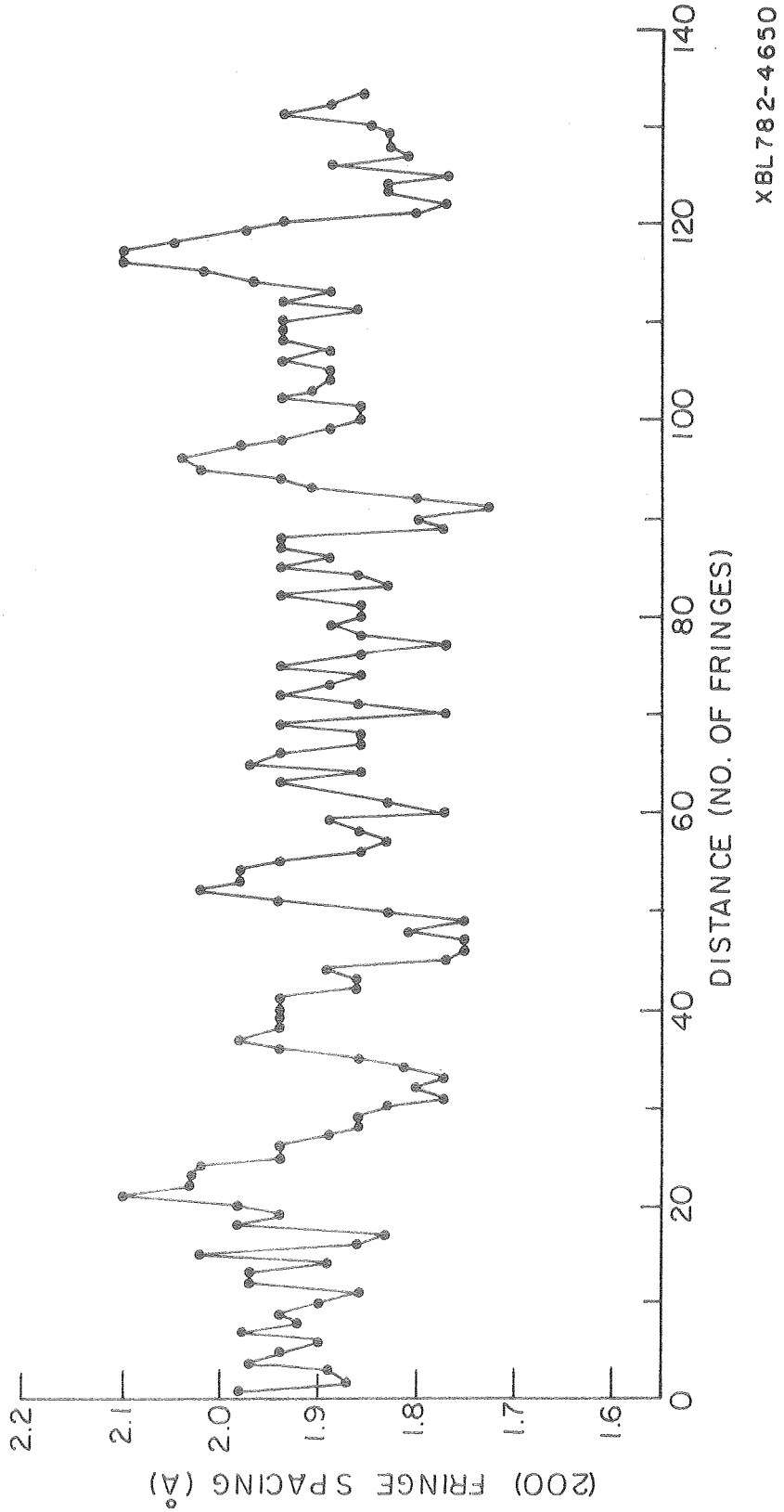
(200) FRINGE SPACING (Å)
2.2
2.1
2.0
1.9
1.8
1.7
1.6
0
20
40
60
80
100
120
140
DISTANCE (NO. OF FRINGES)
XBL782-4650

Fig. 30

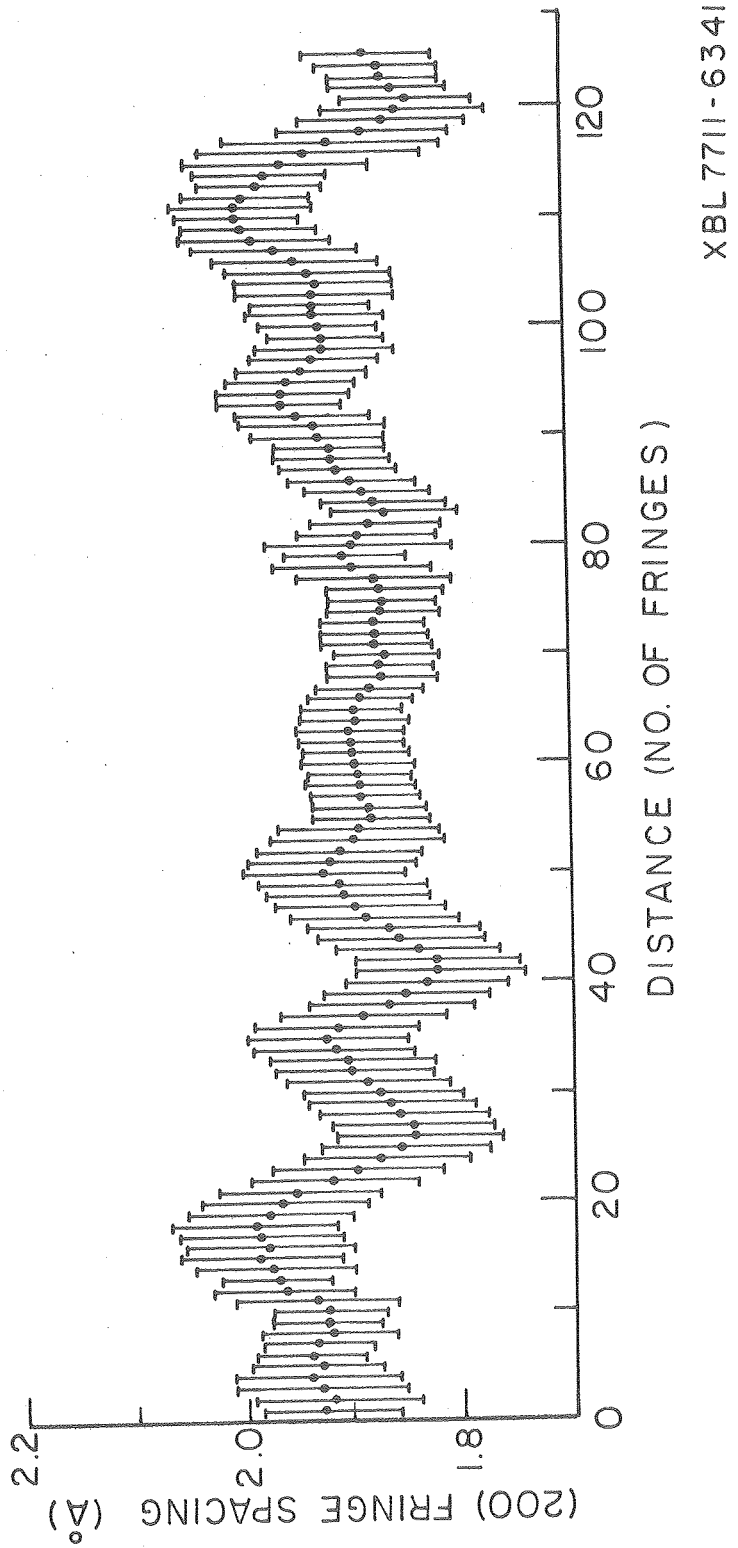
(200) FRINGE SPACING (Å)
2.2
2.0
1.8
0
20
40
60
80
100
120
DISTANCE (NO. OF FRINGES)
XBL 7711-6341

Fig. 31

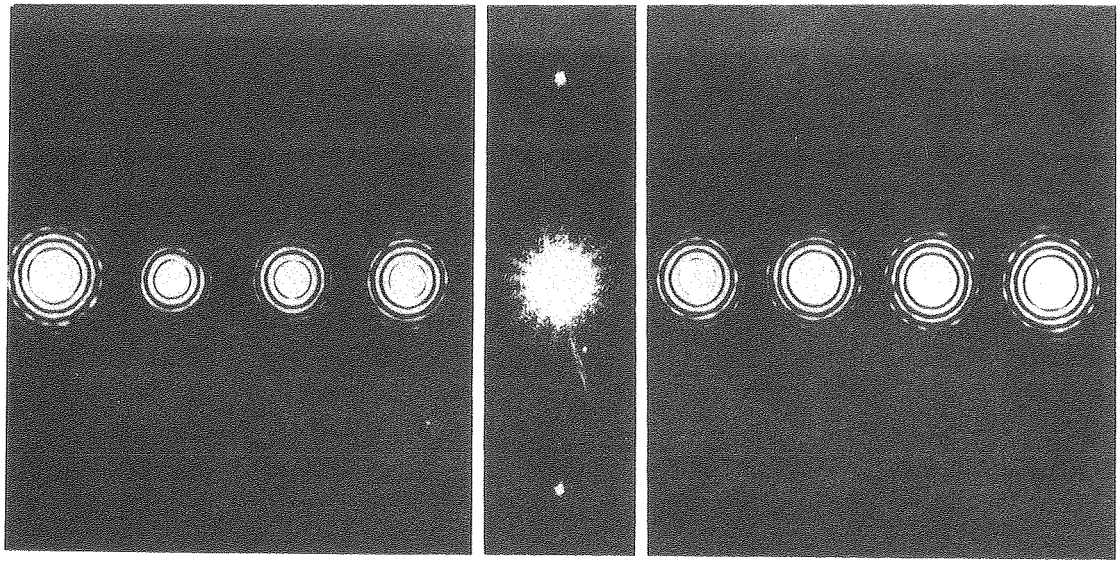

XBB 780-12893

Fig. 32

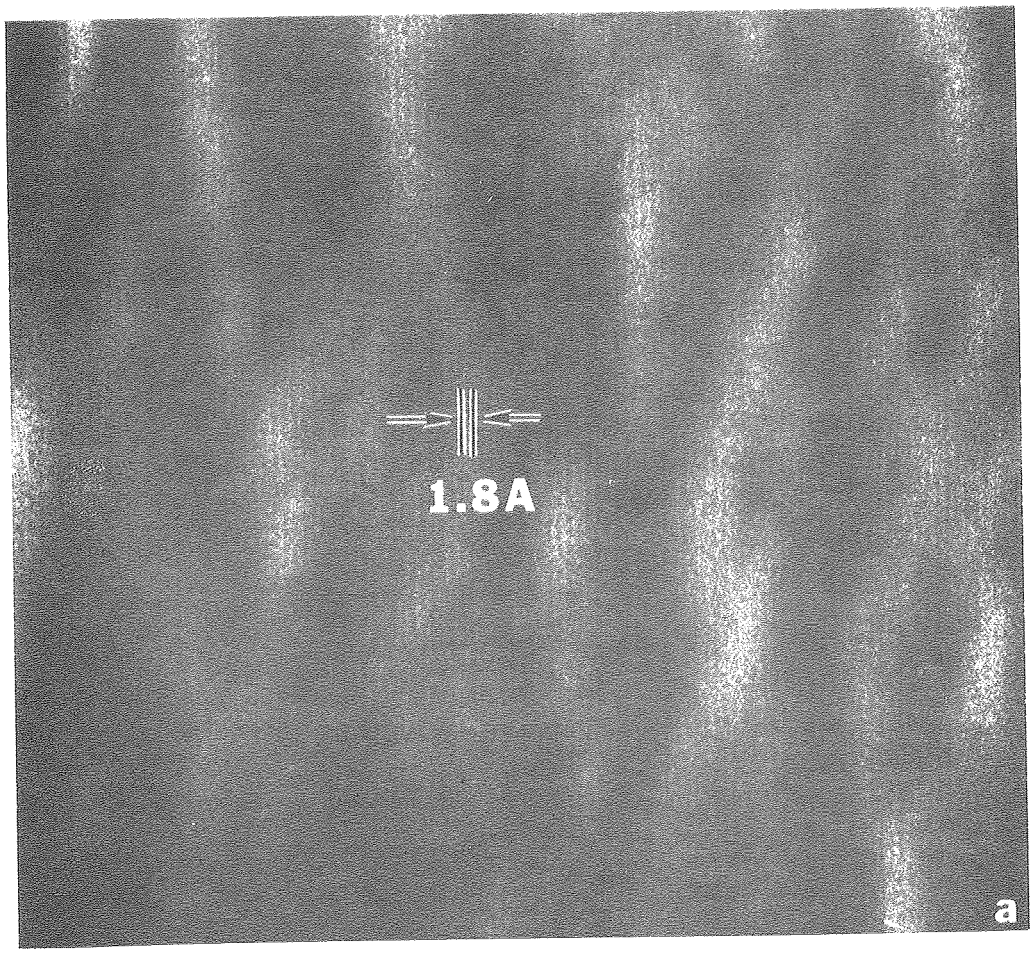

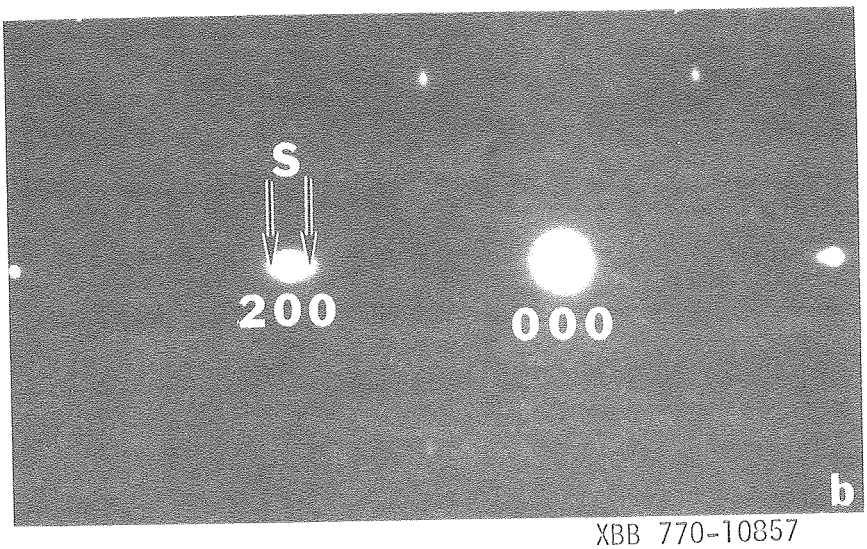

XBB 770-10857

Fig. 33

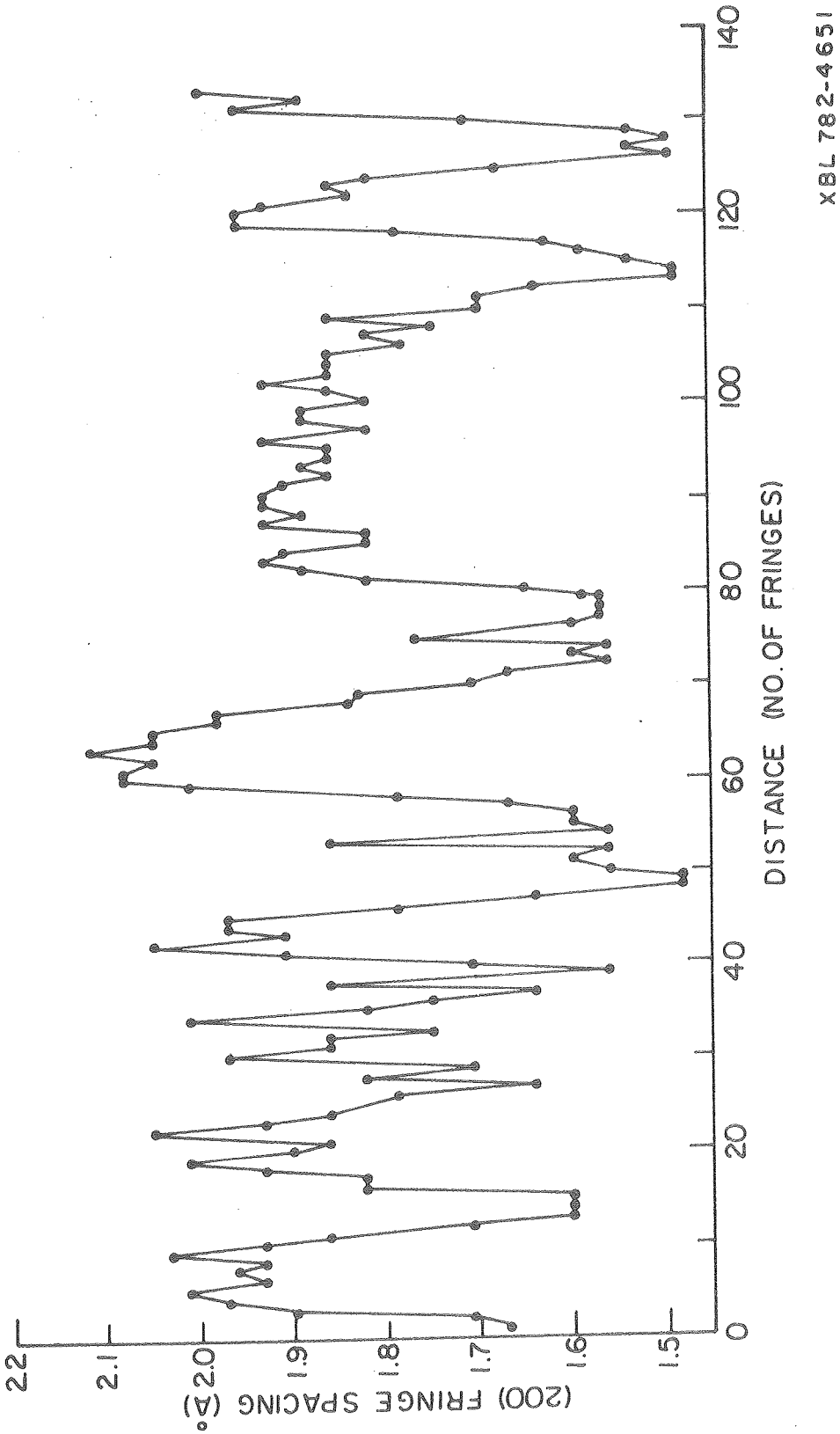
(200) FRINGE SPACING (Å)
2.2
2.1
2.0
1.9
1.8
1.7
1.6
1.5
0
20
40
60
80
100
120
140
DISTANCE (NO. OF FRINGES)
XBL 782-4651

Fig. 34

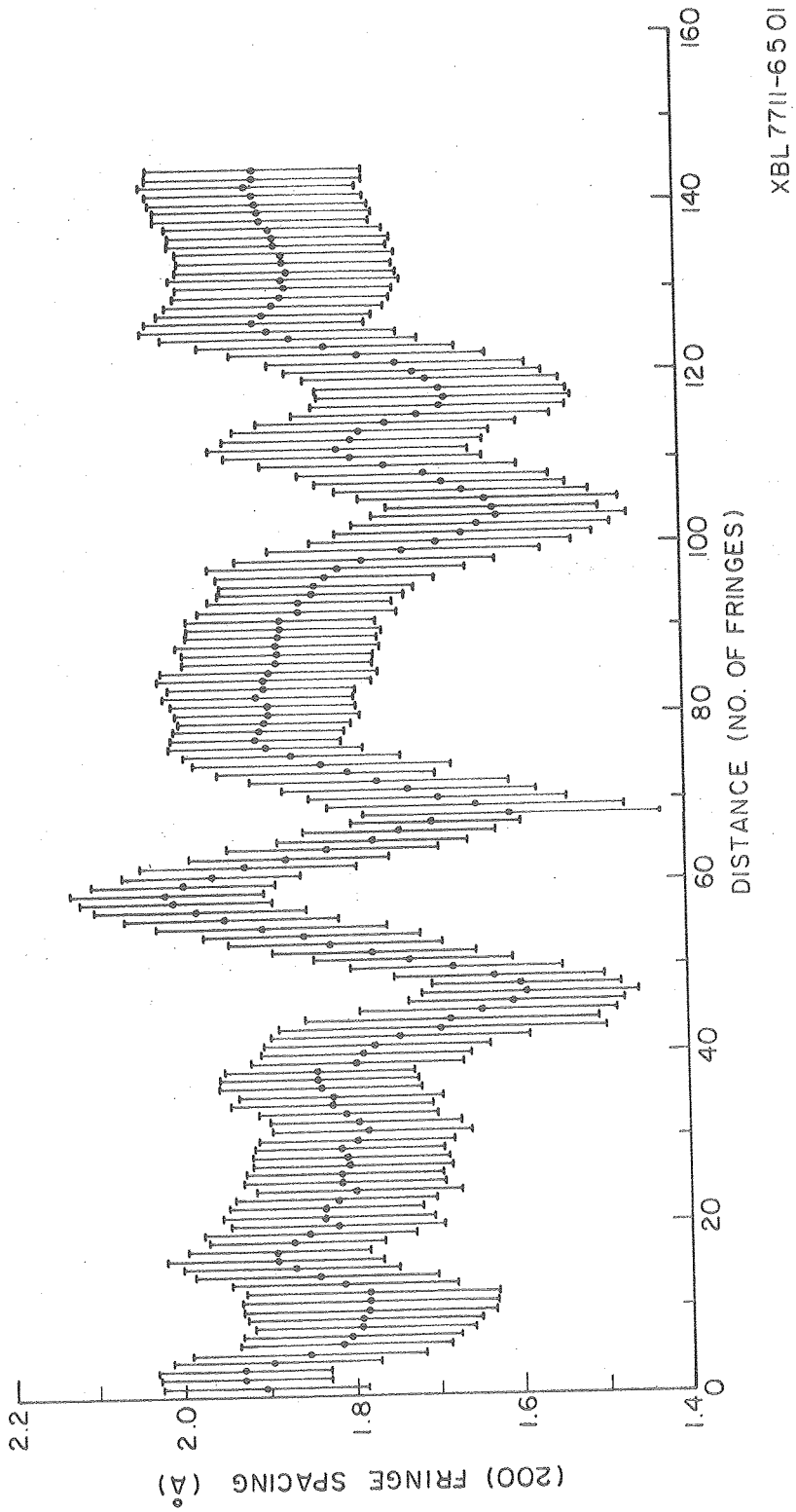
(200) FRINGE SPACING (Å)
2.2
2.0
1.8
1.6
1.4
0
20
40
60
80
100
120
140
160
DISTANCE (NO. OF FRINGES)
XBL 7711-6501

Fig. 35

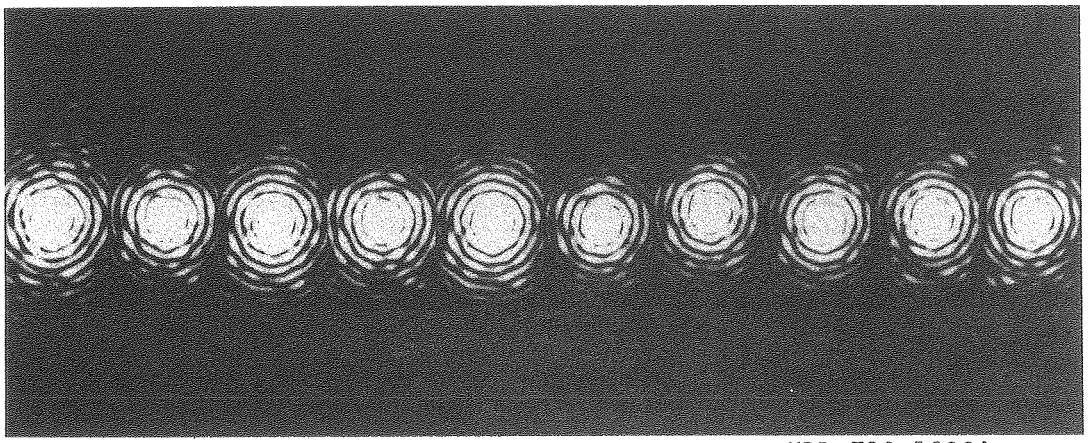

XBB 780-12894

Fig. 36

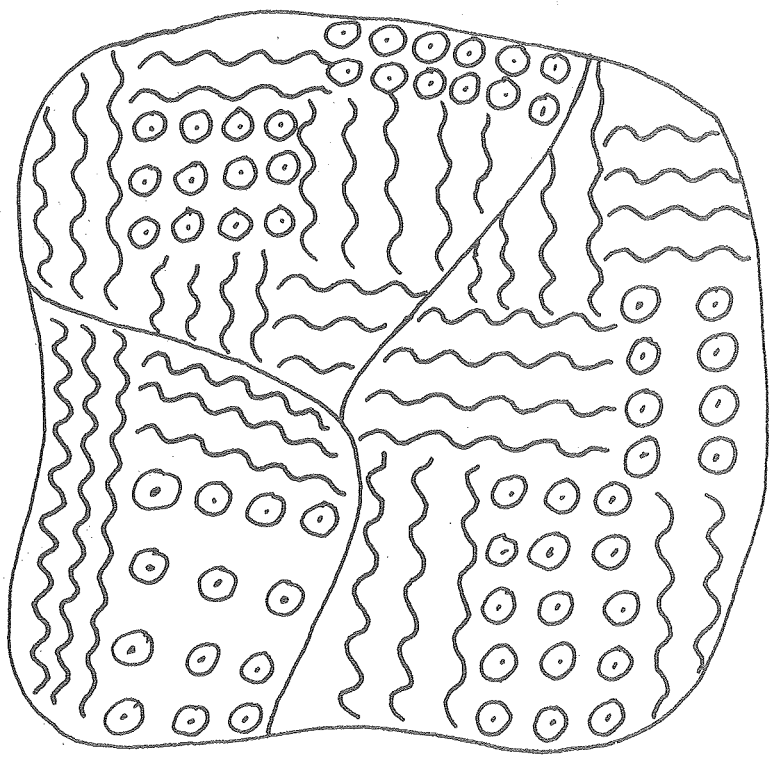

XBL 782-4662

Fig. 37

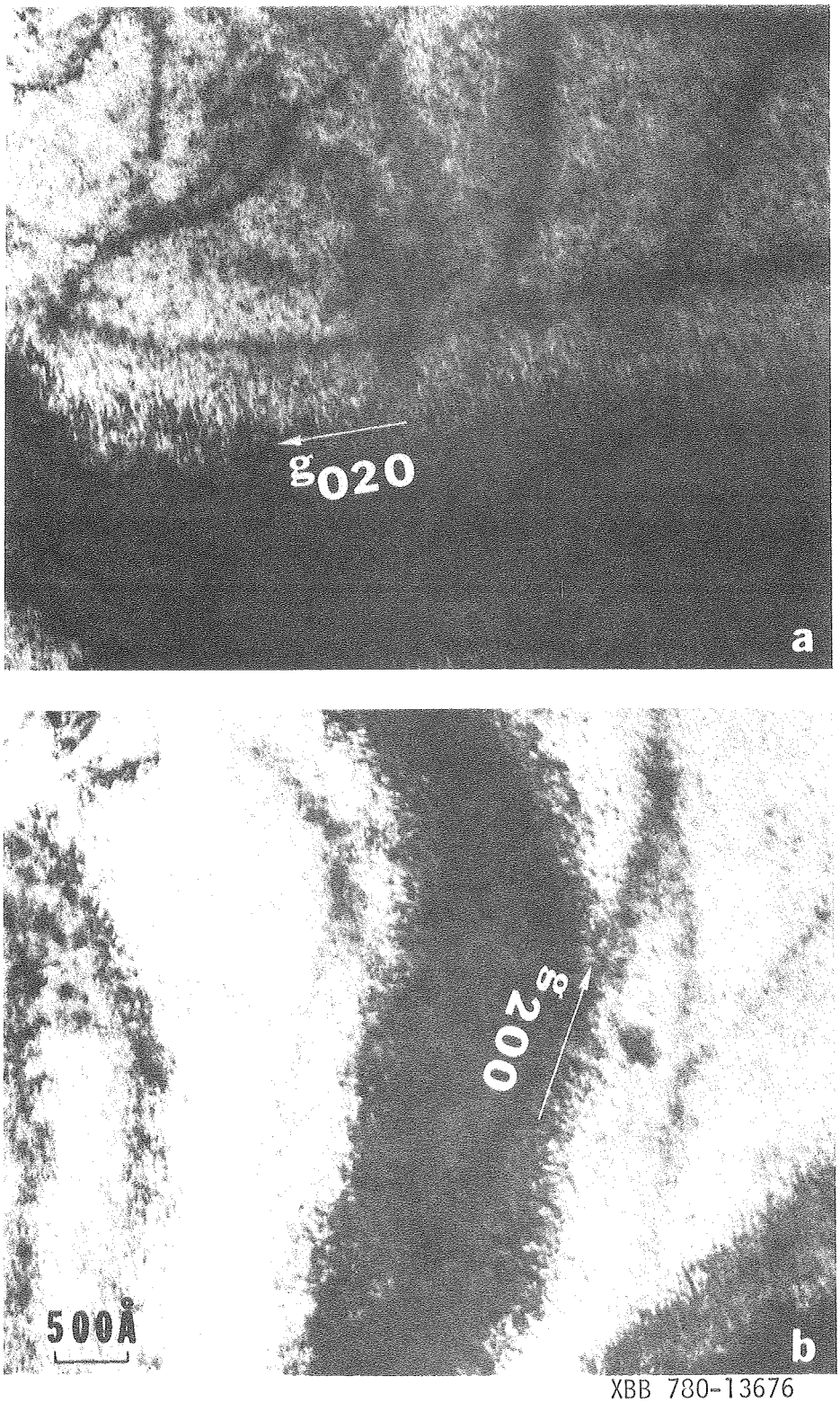

XBB 780-13676

Fig. 38

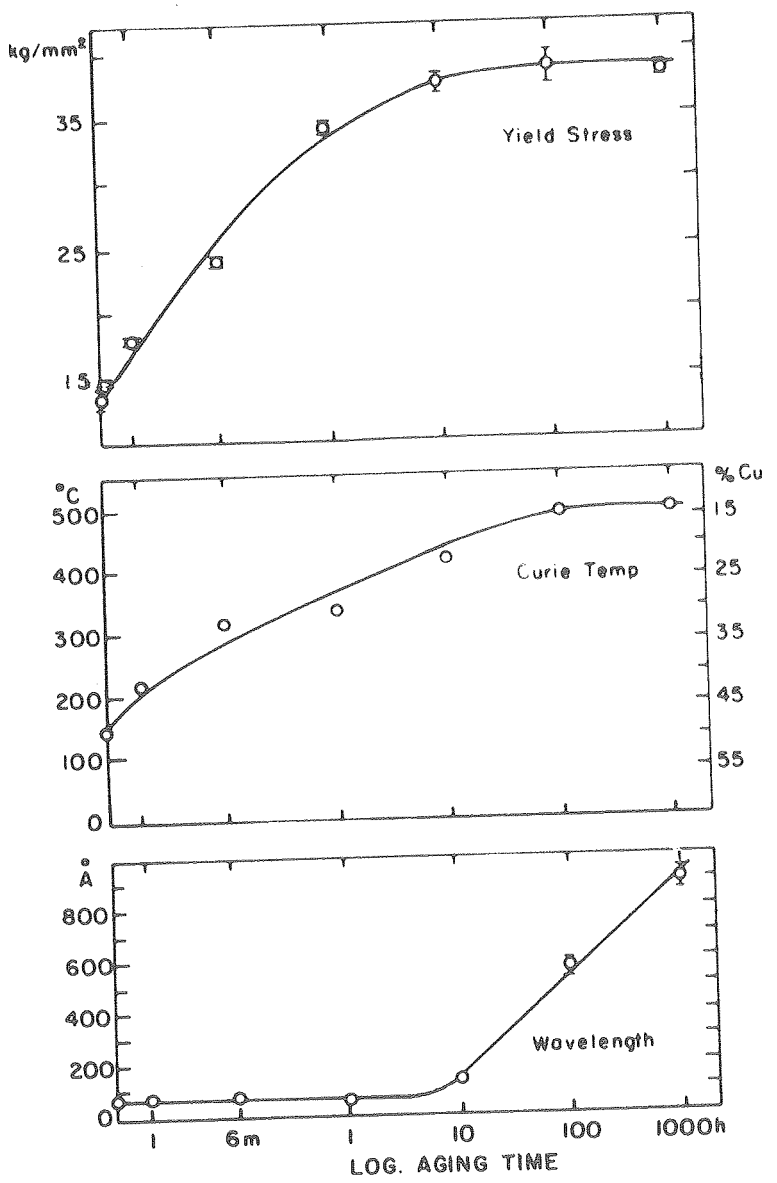
kg/mm²
35
25
15
Yield Stress
°C
500
400
300
200
100
0
Curie Temp
%Cu
15
25
35
45
55
Å
800
600
400
200
0
Wavelength
1
6m
1
10
100
1000h
LOG. AGING TIME
XBL 702-448

Fig. 39

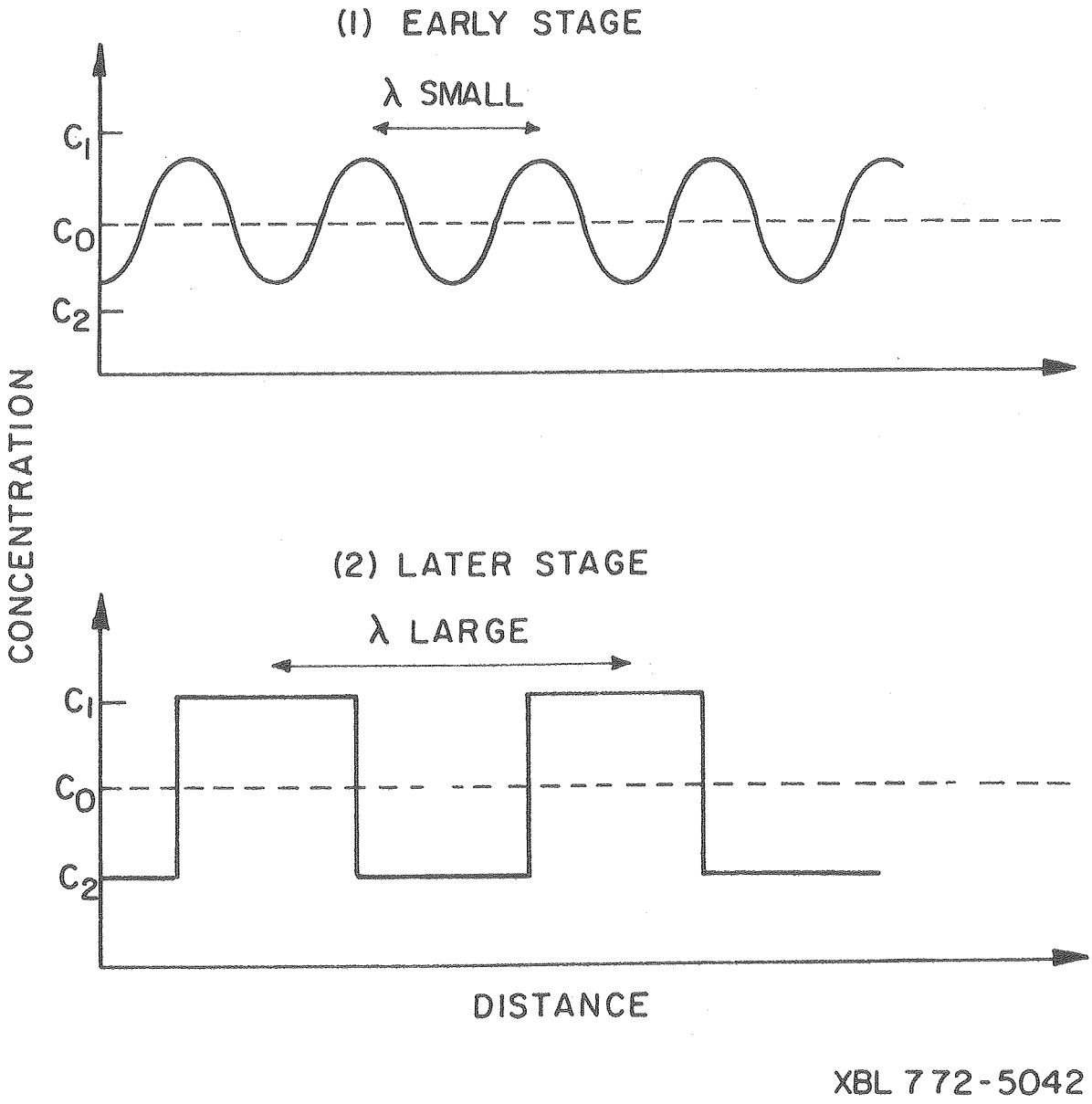
(1) EARLY STAGE
λ SMALL
C1
C0
C2
CONCENTRATION
(2) LATER STAGE
λ LARGE
C1
C0
C2
DISTANCE
XBL 772-5042

Fig. 40

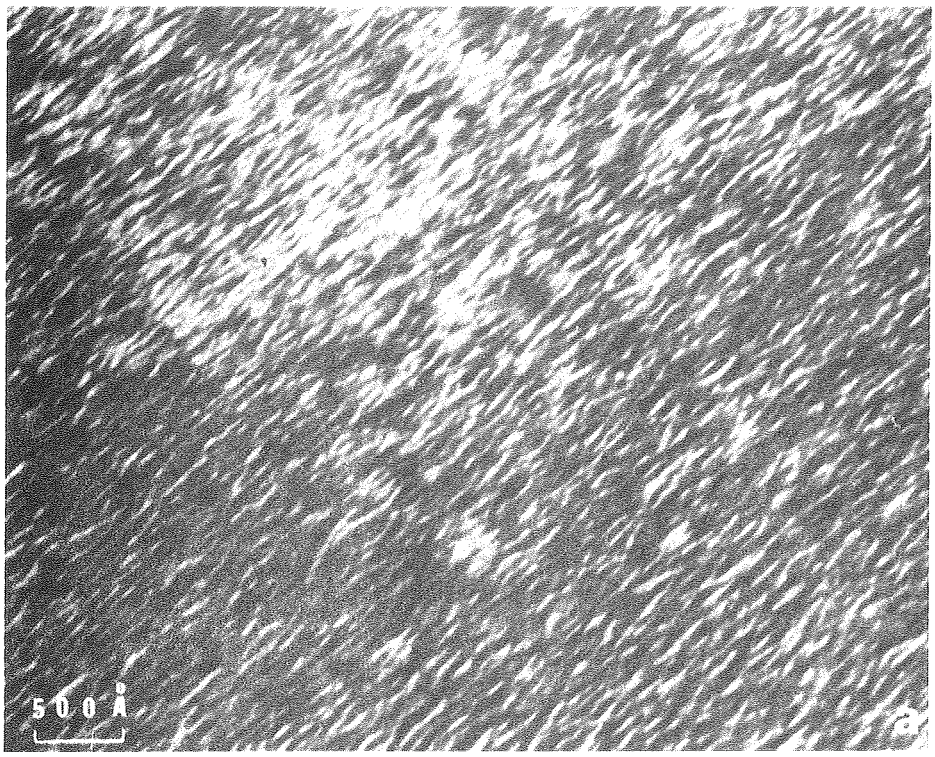

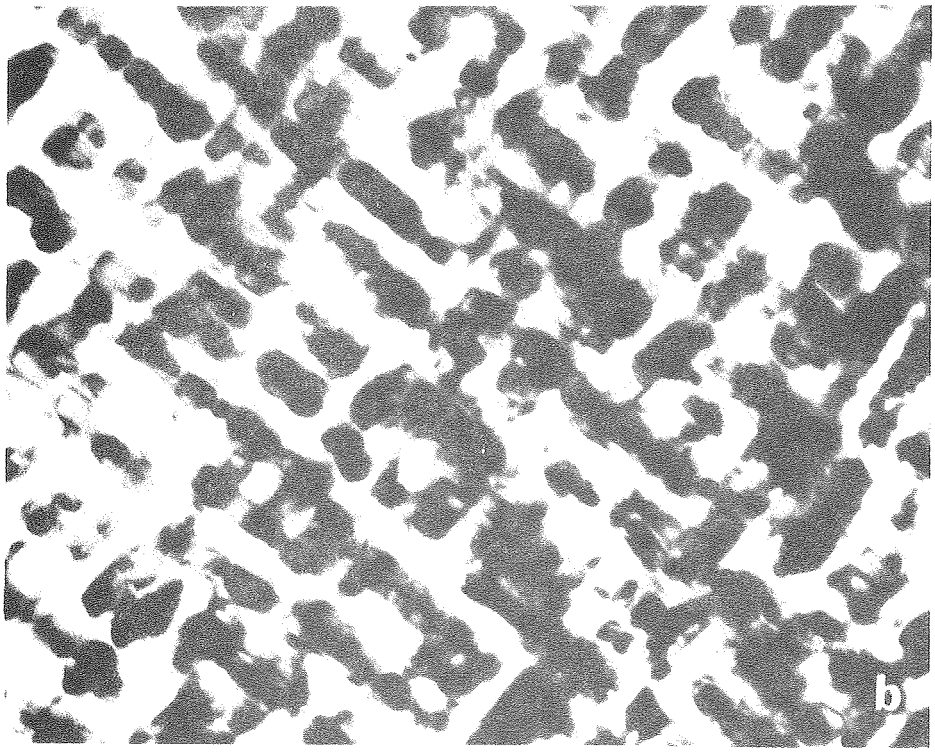

XBB 780-13675

Fig. 41

This report was done with support from the Department of Energy. Any conclusions or opinions expressed in this report represent solely those of the author(s) and not necessarily those of The Regents of the University of California, the Lawrence Berkeley Laboratory or the Department of Energy.